TUDelft

Delft University of Technology

Tracking organoid cell fate dynamics in space and time

Zheng, X.Z.

DOI
10.4233/uuid:8fa320aa-a1b8-4ca2-9e9d-4428911aa02d
Publication date
2023
Document Version
Final published version
Citation (APA)
Zheng, X. Z. (2023). *Tracking organoid cell fate dynamics in space and time*. [Dissertation (TU Delft), Delft University of Technology]. https://doi.org/10.4233/uuid:8fa320aa-a1b8-4ca2-9e9d-4428911aa02d

Important note
To cite this publication, please use the final published version (if applicable).
Please check the document version above.

Tracking organoid cell fate dynamics in space and time

Xuan ZHENG

TRACKING ORGANOID CELL FATE DYNAMICS IN SPACE AND TIME

Dissertation

for the purpose of obtaining the degree of doctor
at Delft University of Technology
by the authority of the Rector Magnificus prof. dr. ir. T.H.J.J. van der Hagen
chair of the Board for Doctorates
to be defended publicly on
Tuesday 6 June 2023 at 15:00 o'clock

by

Xuan ZHENG

Master of Science in Applied Physics
Delft University of Technology, The Netherlands
born in Shanxi, China

This dissertation has been approved by the promotors.

Composition of the doctoral committee:
Rector Magnificus   Chairperson
Prof. dr. ir. S.J. Tans,   Delft University of Technology / AMOLF, promotor
Dr. J.S. van Zon,   AMOLF, copromotor

Independent members:
Prof. dr. M. Tanenbaum,   Delft University of Technology / Hubrecht Institute
Prof. dr. M.M. Maurice,   UMC Utrecht
Prof. dr. A. Grapin-Botton,   Max Planck Institute, Germany
Prof. dr. S. Rulands,   Ludwig Maximilian University of Munich, Germany
Dr. R. van Amerongen,   University of Amsterdam
Prof. dr. N.H. Dekker,   Delft University of Technology, reserve member

After endless mountains and rivers that leave doubt whether there is a path out, suddenly one encounters the shade of a willow, bright flowers and a lovely village.

by Lu You

Contents

SUMMARY

Throughout the lifetime of living systems, tissue homeostasis and renewal constantly take place to confront challenging conditions, both internally, such as cell aging, and externally, such as infections, so that health can be maintained. Such processes require a tight balance between cell proliferation and differentiation. When homeostasis is disturbed, diseases like cancer can develop. Therefore, understanding the regulation of tissue homeostasis is a key question in biology. However, directly monitoring the dynamics of proliferation and differentiation in live animals remains extremely challenging. Common methods, such as immunostaining and single-cell RNA sequencing, require killing the animal and fixing the cells. Therefore, they can merely provide information in a single time frame. As a result, lineage tracing techniques are introduced, where cells are labeled with a heritable marker that can be detected in progeny after a certain period by fluorescence microscopy or sequencing. Nevertheless, they only produce lineage dynamics indirectly.

Organoids recapitulating the original organ are three-dimensional multicellular *in vitro* structures grown from stem cells. They have significantly expanded the toolbox of developmental biologists over the past decade. Organoids can be used to model biological processes during tissue maintenance and disease development, and hold great potential for drug screening and personalized medicine. They can be grown from pluripotent or adult stem cells. Scientists have successfully generated organoids that mimic the gut, stomach, brain, kidney, lung, and liver. Many other types of organoids are currently being generated and optimized. One of the most notable features of organoids as a research tool is their synergy with imaging techniques that enable following spatiotemporal dynamics. Recently developed microscopy techniques that track individual cells through space and time have been applied extensively to embryos and 2D cell cultures to elucidate the cellular processes. **Chapter 1** reviews the technical advances in cell tracking, including the improvement of automatic trackers and the combination of tracking with fluorescent reporters or endpoint measurement. The application of these methods to organoids holds great promise in discovering organizational principles within organs and organoids. In this thesis, we bridge the gap between organoids and cell tracking to investigate proliferation, differentiation, and the Wnt signaling pathway in intestinal organoids.

We used the mouse small intestinal organoids as a model system. They recapitulate the crypt-villus structures and contain the major cell types of the intestinal epithelium. During intestinal homeostasis, proliferation and differentiation must be strictly balanced, as any bias to proliferation can lead to uncontrolled exponential growth. However, how proliferation is controlled to cope with fluctuations and achieve homeostasis remains unknown. **Chapter 2** investigates this question by combining microscopy experiments both *in vitro* and *in vivo* with computational modeling. We used time-lapse imaging and live-cell tracking to track cells in growing intestinal organoid crypts and reconstruct the underlying lineage dynamics. We discovered that sister cells have a high symmetry in

proliferative behavior: either they cease divisions together or they continue to proliferate. Such symmetry was further confirmed by clone size distributions obtained from *in vivo* lineage tracing experiments. To explain the observed stability in the number of proliferating cells during crypt growth, we conducted computational simulations. Our simulations suggest that symmetric proliferative behaviors between sisters can minimize cell number fluctuations. Hence, this study points to a concrete mechanism, proliferative symmetry, for balancing proliferation and differentiation with minimal fluctuations. This mechanism is found in the intestinal epithelium and may be of broad relevance to other tissues.

The intestinal epithelium, consisting of more than six different cell types, is a multitasking tissue that has functions including absorbing nutrients, producing mucus, and secreting hormones. The generation of different cell types and the regulation of the abundance of each type are essential elements for maintaining tissue homeostasis. Intestinal organoids, containing all the cell types in the epithelium, have emerged as an important model to study multi-lineage differentiation. However, as methods for visualizing underlying cell differentiation dynamics are lacking, the main organizational principles of cell-type specifications are still unresolved. In **Chapter 3**, we combined AI-enabled cell tracking with multiplexed endpoint antibody staining to show when and where cells differentiate. After mapping the lineage trees to endpoint cell identities, we implemented a backpropagation method to infer the cell types present during imaging and the type transitions made along the lineage trees. Surprisingly, we discovered that cells which ultimately differentiate and migrate to the villus are committed to their new type already deep inside the crypt – when still surrounded by their relatives that remain stem cells at the crypt bottom. Such early fate commitment can lead to several unexpected consequences. First, secretory cells commit even before terminal division, causing secretory fates to emerge symmetrically in sister cells. Second, the relative abundances of secretory and absorptive cells are controlled mainly by the proliferation after commitment. Furthermore, the spatial patterning of different cell types is achieved by type-dependent cell movement and rearrangements after commitment. This 'commit-then-sort' model contrasts with the idea that cells only commit after moving away from the crypt and into the transit-amplifying region, and raises new questions about underlying commitment and sorting mechanisms in the intestinal epithelium. These findings may also be generally relevant, as the tissue architecture and molecular pathways are conserved in diverse stem cell systems.

Cell signaling plays a crucial role in regulating the capacity of each cell to receive information from the environment, communicate with other cells, and execute biological processes. Multiple signaling pathways, such as Wnt and Notch signaling pathways, have been demonstrated to be actively involved in the maintenance of intestinal homeostasis. Understanding the mechanisms of how these pathways regulate cell type transitions and cell proliferation remains an important question in the field. In **Chapter 4**, we focus on the regulation of Wnt signaling and how it affects cell differentiation. In mouse small intestinal organoids, Wnt is secreted by Paneth cells at the crypt bottom and is important for stem cell maintenance. Direct contact with Paneth cells is crucial for stem cells to maintain stemness. There are two competing hypotheses for Wnt signaling regulation after stem cells lose contact with a Paneth cell. 1) Cells experience a decreasing Wnt gradient as their distances to Paneth cells increase, and 2) Wnt signaling levels are only altered with each cell division by dilution of the amount of Wnt bound per cell. In this chapter, we imaged

and tracked cells in intestinal organoids carrying an Axin2 reporter, which is a Wnt target gene, to follow the spatio-temporal dynamics of Wnt signaling. We used laser ablation to remove single Paneth cells. Subsequently, endpoint antibody staining was performed to identify cell types. We showed quantitatively that cells rapidly reduce their Wnt signaling levels once their contact with Paneth cells is lost. This reduction was observed both in cells moving away from the Paneth cells and in cells whose neighbor Paneth cells are ablated. Such reduction is not due to dilution caused by cell growth or division, as we also observed the rapidly reducing Wnt signaling in conditions where growth and proliferation are inhibited. If Paneth cell contact is not regained in time, cells differentiate even if they remain close to Paneth cells. As a result, our study suggests a new Wnt signaling dynamics model, a timer model. In this model, the loss of contact with a Paneth cell triggers the timer for stem cell differentiation. Such a timer starts much earlier than the occurrence of cell divisions or cell migration further away from the crypt bottom.

Finally, in **Chapter 5**, we briefly summarize the major discoveries made in this thesis. In addition, we propose promising future paths to illustrate the application of living cell tracking methods in organoids and to obtain more insights into organ development and disease mechanisms. This includes tracking in platforms such as healthy human intestinal organoids, organoids recapitulating Inflammatory Bowel Disease, cancer organoids, and organoids co-cultured with bacteria and immune cells. These applications will advance our knowledge of the differentiation trajectories in the human intestine, the influence of signaling pathways on the differentiation dynamics, Inflammatory Bowel Disease development, and cancer development and treatment.

Samenvatting

Levende systemen worden continu geconfronteerd met interne en externe uitdagingen, zoals slijtage van cellen en infecties. Om gezond en in homeostase te blijven moeten deze systemen zich dus constant vernieuwen. Daarin moet een strak evenwicht gevonden worden tussen celgroei en differentiatie. Zodra homeostase verstoord raakt kunnen ziektes als kanker zich ontwikkelen. Daarom is het essentieel om te begrijpen hoe de homeostase van biologische weefsels gereguleerd wordt.

Tegelijkertijd is het zeer ingewikkeld om de dynamica van celgroei en differentiatie te bestuderen in proefdieren. Bij geijkte methodes, zoals immunhistochemie en enkel-cels *RNA-sequencing*, is het nodig om de dieren te doden en weefsels te fixeren. Daarom kunnen dit soort experimenten enkel informatie over één enkel tijdspunt opleveren. Om dit probleem te ondervangen zijn zogeheten lineage tracing experimenten ontwikkeld, hierbij worden cellen gelabeld met een unieke erfelijke marker. Die marker wordt doorgegeven aan alle nakomelingen van betreffende cellen en kan op het einde van het experiment gedetecteerd worden met fluorescentiemicroscopie of *sequencing*. Maar ook hier geldt dat de dynamica van het systeem niet direct geobserveerd kan worden.

Organoïden zijn drie dimensionale multicellulaire structuren die *in vitro* kunnen groeien vanuit stamcellen. Deze structuren recapituleren veel eigenschappen van het orgaan waaruit de stamcellen oorspronkelijk vandaan komen. Hierdoor kunnen organoïden gebruikt worden om weefselhomeostase maar ook bepaalde ziektebeelden te modelleren. Dit biedt weer grote mogelijkheden voor het screenen van mogelijke medicijnen en het stellen van gepersonaliseerde diagnoses.

Organoïden kunnen gegroeid worden uit pluripotente stamcellen of uit volwassen stamcellen en wetenschappers hebben organoïde-modellen weten te genereren voor de darmen, maag, longen, brein, nieren en lever. Ook voor andere organen worden nu organoïden ontwikkeld en geoptimaliseerd.

Een belangrijk aspect van organoïden is dat ze uitstekend te combineren zijn met microscopische technieken die het mogelijk maken om weefsels te volgen in de ruimte en in de tijd. Dit soort microscopie wordt al veel toegepast binnen de embryologie en op 2D celculturen. **Hoofdstuk 1** reflecteert op de recente ontwikkelingen in het volgen van levende cellen, waaronder verbeteringen in algoritmes die dit volgen automatiseren, combinaties met fluorescente reporter eiwitten en extra metingen na afloop van het experiment. De toepassing van die ontwikkelingen op organoïden biedt kansen om de fundamentele principes achter de regulatie van groei van organoïden - en daarmee de homeostase van organen - te ontdekken. In deze thesis overbruggen we het gat tussen de techniek van microscopisch cellen volgen en die van organoïden om proliferatie, differentiatie en Wnt signaaltransductie te onderzoeken in organoïden van de dunne darm.

Als modelsysteem gebruiken we organoïden van de dunne darm van de muis. Deze organoïden recapituleren de crypt-villus structuur en bevatten de celtypes die kenmerkend

zijn voor het epitheel van de dunne darm. Homeostase vereist dat proliferatie en differentiatie van cellen perfect gebalanceerd is, teveel proliferatie leidt tot ongecontroleerde exponentiele groei van het aantal cellen. Het is echter nog niet duidelijk hoe proliferatie gecontroleerd wordt en omgaat met fluctuaties in het aantal cellen. In **Hoofdstuk 2** wordt deze vraag onderzocht doormiddel van *in vivo* en in vitro microscopie experimenten in combinatie met computermodellen. Time-lapse microscopie werd gebruikt om live cellen en hun delingen te volgen in organoïden en de dynamica van proliferatie te reconstrueren. We beschrijven dat zustercellen zeer symmetrisch zijn in hun proliferatieve gedrag. Ze stoppen ofwel allebei met delen of blijven beide groeien. Eenzelfde soort symmetrie konden we observeren door te kijken naar de grootte van klonen in lineage tracing experimenten *in vivo*. Om te verklaren waarom het aantal delende cellen gelijk blijft tijdens de groei van een organoïde hebben we computer simulaties gebruikt. Deze simulaties laten zien dat symmetrische proliferatie fluctuaties in het aantal cellen kan minimaliseren. Daarmee suggereert dit onderzoek een concreet mechanisme, symmetrische proliferatie, om proliferatie met differentiatie te balanceren met minimale fluctuaties. Hoewel we dit mechanisme beschrijven voor het dunne darm epitheel zou eenzelfde soort mechanisme ook in andere weefsels kunnen bestaan.

Het dunne darm epitheel bestaat uit meer dan zes verschillende celtypen en heeft verschillende taken, waaronder het absorberen van voedingstoffen, het produceren van mucus en het uitscheiden van hormonen. Het genereren van deze verschillende celtypes in de juiste hoeveelheden is een essentieel onderdeel van de homeostase. Dunne darm organoïden zijn een belangrijk model om deze complexe differentiatie van stamcellen in meerdere celtypen te onderzoeken. Methodes om de dynamica van deze differentiatie te visualiseren ontbreken echter nog en daarmee zijn ook de basisprincipes waarmee een cel zijn type wordt gecontroleerd nog onduidelijk. In **hoofdstuk 3** combineren we time-lapse microscopie, het volgen van cellen met behulp van kunstmatige intelligentie en immuunhistochemie om erachter te komen wanneer en waar cellen differentiëren in verschillende celtypen. Nadat we na afloop van een experiment het celtype van elke cel hadden geïdentificeerd met immuunhistochemie, gebruikten we een *backpropagation* strategie om het celtype te bepalen voor cellen uit voorgaande generaties en te identificeren waar in de gereconstrueerde stambomen transities in celtype plaats vonden. Verassend genoeg zagen we dat cellen die uiteindelijk differentiëren en vanuit de crypt in villus terechtkomen zich al committeren aan hun uiteindelijke celtype diep in de crypt – op dat moment zijn ze nog omgeven door stamcellen die niet zullen differentiëren en in de crypt zullen blijven. Deze vroege beslissing heeft verschillende verassende consequenties. Ten eerste committeren secretiecellen zich nog voor hun laatste celdeling wat ertoe leidt dat ze ontstaan in zusterparen. Ten tweede, worden de relatieve fracties van secreterende en absorberende cellen vooral gecontroleerd door het aantal celdelingen na de celtype beslissing. Een cel bereikt zijn uiteindelijk locatie ook pas na deze beslissing door migratie en herordening die specifiek voor het celtype is. Dit 'beslis-dan-sorteer' model contrasteert met het idee dat cellen pas een keuze voor een celtype maken nadat ze uit de crypt en in de transitionele zone zijn gemigreerd. Dit onderzoek biedt een basis om de onderliggende mechanismen van zowel de celtype beslissing als de daaropvolgende ordening verder te onderzoeken. Ook kunnen de conclusies voor andere weefseltypen relevant zijn, zowel de ruimtelijke architectuur als de moleculaire signalen zijn vaak overeenkomstig in verschillende epitheliale weefsels.

Signaaleiwitten zijn cruciaal voor cellen om informatie te ontvangen over hun omgeving en te communiceren met andere cellen. Signaaltransductieketens, zoals die van de eiwitten Wnt en Notch, zijn ook betrokken bij de homeostase van het darmepitheel. Maar hoe deze signaalroutes precies proliferatie en differentiatie controleren is nog een belangrijke open vraag. In **hoofdstuk 4** focussen we op communicatie via Wnt en wat voor effecten dit heeft op differentiatiebeslissingen. In organoïden is Wnt afkomstig van Paneth cellen onderaan de crypt en zorgt het dat stamcellen daar hun identiteit behouden. Er zijn twee hypotheses over hoe Wnt-communicatie zich gedraagt nadat een stamcel contact verliest met een Paneth cel. 1) Cellen ondergaan een graduele daling in Wnt naarmate ze zich verder bewegen van de Paneth cel en 2) Wnt-niveaus veranderen enkel tijdens cel divisies die leiden tot verdunning van de hoeveelheid Wnt per cel.

In ons onderzoek volgden we organoïden met een Axin2 reporter onder de microscoop. Axin2 is een target van Wnt en de reporter laat ons dus dynamica van Wnt-communicatie in de ruimte en de tijd volgen. We gebruiken laserablatie om Paneth cellen (één per keer) uit organoïden te verwijderen. Vervolgens gebruikten we immuunhistochemie om celtypes te achterhalen. Hiermee konden we kwantificeren dat cellen snel Wnt verliezen zodra het contact met een Paneth cell is verbroken. Deze reductie is niet te wijten aan celgroei of deling, we zien namelijk eenzelfde reductie wanneer proliferatie geblokkeerd is. Wanneer stamcellen niet op tijd weer in contact komen met een Paneth cel differentiëren ze, ook als ze in de buurt van een Paneth cel blijven. Dit alles suggereert een nieuw model voor Wnt-communicatie, een 'timer-model'. In dit model start verbreking van het Paneth cell contact een timer voor een stamcel die uiteindelijk differentiatie triggert. Die timer start al in de crypt en veel vroeger dan de celdelingen en celmigratie die op differentiatie volgen.

Afsluitend, in **hoofdstuk 5**, bespreken we kort de belangrijkste conclusies van deze thesis. Ook suggereren we mogelijkheden om de technieken die we gebruiken in deze thesis toe te passen om nog meer inzicht te krijgen in de homeostase van organen en bijbehorende ziektebeelden. We stellen onder andere voor om cellen te volgen in humane darmorganoïden, organoïden die een model zijn voor het prikkelbare darm syndroom, organoïden van kankerweefsel en organoïden in cocultuur met bacteriën en imuuncellen. Deze toepassingen zullen bijdragen aan ons begrip over de dynamica van differentiatie, hoe verschillende signaaltransductieketens daarop ingrijpen, het prikkelbare darm syndroom en hoe kanker zich ontwikkelt.

1

Cell Tracking For Organoids

M.A. Betjes, **X. Zheng***, R.N.U. Kok*, J.S. van Zon# and S.J. Tans#*

Organoids have emerged as powerful model systems to study organ development and regeneration at the cellular level. Recently developed microscopy techniques that track individual cells through space and time hold great promise to elucidate the organizational principles of organs and organoids. Applied extensively in the past decade to embryo development and 2D cell cultures, cell tracking can reveal the cellular lineage trees, proliferation rates, and their spatial distributions, while fluorescent markers indicate differentiation events and other cellular processes. Here, we review a number of recent studies that exemplify the power of this approach, and illustrate its potential to organoid research. We will discuss promising future routes, and the key technical challenges that need to be overcome to apply cell tracking techniques to organoid biology.

* denotes co-first authors, # denotes co-corresponding authors.

1

1.1 Introduction

While the development and maintenance of organs is one of the most fundamental problems in biology, our understanding of it is far from complete. A hallmark of this process is the differentiation of cells in time, in terms of proliferative potential and cell type, with individual cells giving rise to complex lineages that organize in space to shape tissues and organs. Thus far, these differentiation dynamics have often been studied using the lineage tracing method [8, 97, 171]. Here, cells are labeled with a heritable marker such as fluorescent genes or a genetic barcode, for instance using Cre-Lox recombination [110, 145] or lentiviral transduction [103, 174, 175]. This label can be detected in progeny after a certain period by fluorescence microscopy or single-cell sequencing, and hence, allows inference of genealogical relations between cells.

However, lineage tracing does not yield complete lineage trees nor provide information on the temporal dynamics of cells, such as their movements, growth rates, transient signaling, and timing of differentiation events (Fig. 1.1), which limits progress on many important questions. For instance, it remains largely unclear when and where cell fates are actually set, whether differentiation is either a consequence or a cause of spatial organization, how size and shape homeostasis is achieved, or how lineage dynamics are remodeled upon injury or disease. We also know little about the possible interplay with cellular metabolism, and the plethora of molecular signals from adjacent cells, for instance from the immune system. Elucidating the spatiotemporal dynamics is central to resolve these crucial issues and to elucidate the organizational principles of organ development [95].

A different technique, here referred to as cell tracking has the potential to reveal these developmental dynamics. As opposed to lineage tracing based on static snapshots, cells are here followed in real time over multiple generations, which can thus provide temporal dynamics, complete lineage trees, as well as spatial organization and cellular movements. Furthermore, cell tracking can readily be combined with the large spectrum of microscopy techniques that have been developed to study cell biology. For instance, the expression of fluorescent proteins directly identify differentiation events, cell-cycle progression, cytoskeletal structures, the dynamics of key molecular signals like Wnt or Notch, while FRET sensors may detect more rapidly changing signals such as calcium and metabolites [4, 89, 164].

Cell tracking has been applied extensively to study the early development of embryos, at increasing levels of sophistication [111, 156, 163], but poses challenges to the study of organs, given the challenges of time-lapse microscopy deep within tissues at later stages of development, even as intra-vital imaging is possible at lower resolution and throughput [120]. Yet, in recent years organoids have emerged as a model system for studying development and disease at the cellular level, including patient derived systems, which are ideally suited for this approach. Organoids are self-organizing cellular assemblies, which are grown in vitro and recapitulate organ structure and functionality to a striking degree [31, 142]. Due to their in vitro nature, the growth and maintenance of organoid tissue can be observed directly by timelapse microscopy [119]. Yet, cell tracking approaches have only scarcely been applied to organoids thus far.
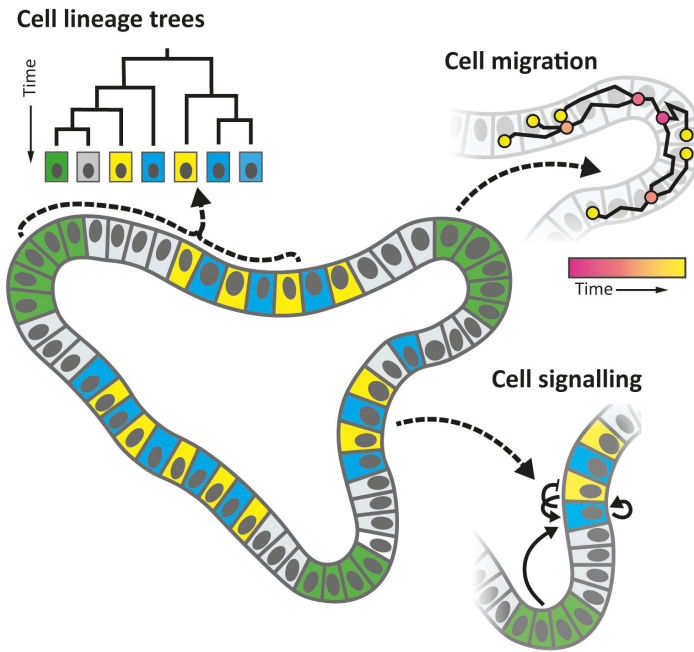
Fig 1.1: Organoid properties that can be studied by "cell tracking," a technique in which (nearly) all cells are followed in time over multiple generations, using 3D time-lapse microscopy and automated image analysis, along with a host of fluorescence detection methods. Tracked cell positions allow one to reconstruct lineage trees, follow migration, growth, and division dynamics, while fluorescence reporters may be used to study differentiation events, signaling pathways, and metabolic states, which are key to understand cellular decision-making during development.

The aim of this review is to discuss the potential of cell tracking approaches for organoid science, as well as its technical challenges. We will do so by focusing on developmental systems ranging from 2D cell cultures to developing embryos, which have been studied extensively by cell tracking methods, and illustrate the scientific questions that it can uniquely address.

1.2 Automatic cell tracking

Automated tracking of individual cells in time has become a powerful approach to study cellular dynamics in cell lines and embryos [158]. Pioneering examples include tracking of embryos of Caenorhabditis elegans, fruit flies, zebrafish, and mice [2, 6, 132]. In a recent paper, 104 cells were tracked in growing mouse embryos over 48 h, during gastrulation and early organogenesis [96]. The authors imaged cell nuclei using adaptive multi-view light sheet imaging. Cells were tracked using a Gaussian mixture model, with the center of each nucleus determined by fitting their fluorescent signal to a 3D Gaussian function. By assigning cells present at the end of the experiment to different tissues, e.g., the heart field

or the neural tube, based on anatomical features, and by following the tracks of these cells backward in time, it was possible to reconstruct how these cells flowed out of the primitive streak and assembled into tissues. This revealed that both the timing and position of cells as they left the primitive streak was key to determining their cell fate. Moreover, by tracking cell divisions in time, the authors showed that the orientation of cell divisions changes several times during neural tube closure, with important impact on tissue morphology.

Despite the advance in analyzing mouse embryogenesis, the McDole study also underscores the formidable technical challenges that remain when studying development, including in organoids. While the tracking error rate was low enough to reconstruct the general flow of cells, it was too high to automatically reconstruct lineages in most parts of the embryo. This is because a single erroneous switch in cell identity can corrupt large parts of the lineage tree. Instead, the authors used a mosaic Cre/loxP reporter to sparsely label small subsets of cells. This strongly reduced cell identity mistakes, by increasing the spacing between tracked cells, but severely reduced the lineage information that was captured. While such analysis of cell flow coupled to fate is useful for many applications, acquiring more exhaustive lineage information is of particular importance for organoids, for instance to identify the rare differentiation events and correlations between them, or to reveal spatial interactions on short length scales, including those between neighboring cells that originate from cell–cell signaling.

Following each cell without error requires both fine-tuned image analysis algorithms to accurately identify all nuclei and their positions, as well as a careful balance between limiting phototoxicity and increasing temporal and spatial imaging resolution. Similar to the embryo systems discussed above, organoids have extended 3D structures that lead to out-of-focus light and scattering, resulting in decreased resolution. In addition, cell nuclei tend to be more closely packed compared to early embryos and, particularly in epithelia, nuclei move rapidly along the apicobasal axis during division [98]. These properties require comparatively fast imaging (one 3D image every 5–15 min) at high spatial resolution (better than 1 mm/pixel), and generally complicates identification of all nuclei in each frame, for instance using gaussian fitting, and linking them through time without error. Light-sheet imaging may be used [119, 139], which can limit resulting phototoxicity. This technique has also been used to study the flow of embryonic renal cells in kidney organoids during kidney rudiment re-aggregation [64]. However, more broadly available confocal imaging is often sufficient for organoid time-lapse imaging studies.

Apart from imaging, the dense 3D tissues found in organoids also pose challenges for nuclei identification using established image analysis approaches, such as Gaussian mixture models. An important recent advance in this regard is the use of neural networks and machine learning. This approach, which is based on a training procedure that uses manually analyzed datasets to learn to identify nuclei, was shown to improve performance in nonorganoid systems with closely packed cells [163, 179]. Another issue is that cell tracking software can be difficult to use for non-experts [99]. Cell trackers often need to be reprogrammed, reconfigured, or retrained in the case of a neural network approach, upon changes in the system studied, imaging parameters, or fluorescent reporters, although algorithms that work for a wider range of microscopy images are developed [154]. Finally, an important practical problem is that software packages are not always well suited to correct for the tracking errors they invariably generate. This feature is less important when

studying properties such as cell flow, but is important for lineage analysis in organoids, where differentiation events may be strongly influenced by stochasticity or neighbor interactions.

As a consequence, manual cell tracking approaches are still used, even for systems with hundreds of cells [178]. A promising new direction for organoid systems is to combine automated tracking based on neural networks with manual error correction steps. Such an approach was used to reconstruct cell lineages by tracking 50 cells during embryonic brain regionalization in brain organoids [54]. Key to scaling up such a hybrid approach from a limited number of lineages to entire organoids is to incorporate algorithms that automatically identify possible errors and allow for efficient manual correction of these errors. Recently, we developed such a hybrid approach to perform lineage tracking for whole intestinal organoids [79].

In the future, we expect that automatic cell tracking approaches will continue to improve, driven in part by advances in machine learning methods [158]. Currently cell tracking studies focus primarily on cellular movement and divisions. With automatic cell tracking becoming more accessible, a range of new applications will open up in organoid research, including the study of cellular differentiation, tissue renewal, shape and symmetry changes, and may involve simultaneous measurements of key regulatory and metabolic signals [75, 121].

1.3 Tracking combined with fluorescent markers

The tracking of cells and their corresponding lineage trees by itself is often not enough to understand how developmental decisions are made. The results of these decisions, the cell fates, are invisible in most situations – with the exception of well characterized systems where the cell type can be deduced from its spatiotemporal position and anatomical features, like the mouse embryo discussed in the previous section. By combining fluorescent markers that report on cell type with image-based cell tracking, it is possible to monitor a cell's identity, position and lineage dynamics concurrently, and hence, study where and when cell fate decisions are made.

A recent study [169] showcases the power of this combination. This work focused on tissue regeneration upon damage of the neuromast, a small sensory organ, in zebrafish. An elegant combination of cytosolic and nuclear markers allowed imaging and identification of all three major cell types in the neuromast using only two colors. These fluorescence markers made it possible to selectively photo-ablate different parts of the organ, and to subsequently study the regenerative potential of the different cell types. By manually tracking lineages it was found that multiple cell types have regenerative potential, but only one type has the potential to regenerate all three major cell types in the neuromast.

The authors then aimed to understand how these cell fate decisions are regulated to faithfully regenerate the organ from a single cell type. To analyze the large amounts of data generated during live imaging, feature lists were compiled for every tracked cell, including both intrinsic (e.g., the time since birth) and extrinsic information (absolute position, relative position to other cell types, and polar orientation). Using a machine learning technique called "random forest" to predict cell fate decisions, spatial features, like the position of

1

cells relative to the organ center during division, were shown to be highly predictive of the cell fates that their progeny will take on. Intrinsic features were uninformative, suggesting that in this system, cell fates are not determined by (prior) cellular heterogeneity but by the cells plastically responding to their environment. This influence of position on cell fate would have been difficult to determine without the combination of live fluorescence markers and image based lineage tracking.

For organoids, this approach is increasingly feasible, especially given recent progress in CRISPR based techniques that allow fluorescent reporters to be directly incorporated in organoid lines [4]. An organoid model for breast cancer has been used to study why some cells carrying an oncogenic mutation become highly proliferative while others do not [1]. Tracked lineages and a fluorescent reporter for the mutation indicated that the local density of mutated cells was the most predictive feature. Being within a cluster of other mutated cells yielded increased progeny. Again, the combination of spatial and lineage information (in this case the amount of progeny) provided by cell tracking were central to the conclusions.

We note that the breast organoids from [1] and the neuromasts studied by [169] are comparatively small systems and contained few cell types. Tracking will be more challenging in larger systems of several hundreds of cells, while spectral overlap limits the number of fluorescent labels, and hence, the ability to distinguish all cell types of interest. Besides reporting for cell type, fluorescent proteins can also quantify cellular processes in organoids, such as chromosome and tubulin dynamics during cell division [4, 16, 98]. Even metabolic processes like oxygenation can be followed using fluorescence sensors [108]. Also promising are fluorescence reporters for the signaling pathways that regulate developmental decisions. Often, these reporters can be fused either directly to a downstream target of the pathway or placed under control of a target gene promotor. Short-lived fluorescent proteins might be required to detect rapid pathway activity dynamics [38]. Indeed, newly developed Wnt and Notch reporters have shown notable dynamics, which in turn impact differentiation [36, 94, 123, 148]. These functional read-outs can be readily combined with lineage tracking to quantitatively study correlations with cellular organization and differentiation.

1.4 Tracking combined with endpoint measurements

As discussed in the previous section, signaling dynamics and changes in cell state during development can in principle be monitored directly using fluorescent markers. However, the spectral overlap of fluorescent proteins and the time investments associated with the required genetic engineering limits the number of colors that can be imaged simultaneously to at most 2–3. This severely limits the number of cell types or genes that can be tracked in one experiment.

An approach that may help to circumvent this limitation was used to study 2D cultures of mouse embryonic stem cells [67]. After tracking the cells over time, these same cells were subsequently studied using three-color single molecule RNA-fluorescence in situ hybridization (RNAFISH). These data quantified the expression of three genes that mark various differentiation stages. Each cell was classified as high or low for each gene, resulting in eight possible cell states. These states were correlated with the lineage

history of each cell using an analytical approach called Kin Correlation Analysis (KCA). This method infers the cell-state transition rates during time-lapse imaging by analyzing state-correlations between relative cells, such as sisters and cousins. Reversible transitions occurred only between adjacent cell states, in a linear chain of cell states from pluripotent to more differentiated. Overall, these experiments show how developmental dynamics can be inferred by combining dynamic cell tracking with static endpoint measurements.

One advantage of such endpoint measurements is their scalability. In order to find genes important to Escherichia coli cell cycle control, cells from a library of 235 CRISPR interference (CRISPRi) perturbations were tracked for days jointly in a single experiment, while characterizing phenotypes such as chromosome replication forks, cell size, and growth rates. Afterward, 10 sequential rounds of FISH labeling were performed to identify the underlying CRISPR perturbation in each tracked lineage. Key replication initiation regulators could hence be identified, and yielded new replication initiation control models [24]. Measurements of gene expression in single fibroblast cells and in brain tissue have been performed using a sequential staining method termed multiplexed error-robust FISH (MERFISH) [27, 102]. Applying smFISH to organoids is challenging, due to limited penetration of probes and high background fluorescence, and often requires cryosectioning, which is non-trivial to implement [57]. However, a protocol for 3D smFISH in whole-mount colon organoids, that relied on reducing the background fluorescence of Matrigel, was described recently and may be applicable to other organoid systems [109].

This approach may be extended to other endpoint analysis techniques such as immunostaining. Immunostaining has been often used to study cell type and differential expression statically, without a combination with cell tracking, for instance recently in neural tube development [44]. Multiplexed immunofluorescence imaging techniques allows for more than ten sequential rounds of antibody staining in a tissue [88]. Multiple rounds of immunostaining has been used in intestinal organoids [139], though not in combination with cell tracking. An exciting idea is performing single-cell RNA-sequencing (scRNA-seq) as end-point analysis after cell tracking, as it would allow one to correlate the lineage tree to genome-wide changes in gene expression. However, as cells may then have to be removed from their tracked location to perform sequencing, which may be partially achieved by sorting fluorescently labeled cells or microaspiration, challenges remain in linking these different data sets. Alternatively, cell tracking could be followed by the recently developed spatial transcriptomics technique, which allows for RNA-sequencing while keeping the information of relative cell positions, though current techniques use sectioning and do not provide 3D information [85, 122, 152]. Overall, combining lineage tracking with static endpoint measurements in organoids provides a promising approach to study spatio-temporal organization in developing organoids.

1.5 Discussion

In this review we have highlighted a number of recent studies that show the power of cell tracking approaches and how they can be applied to organoid model systems. They first of all underscore a general reality: the more we follow biological processes in time, the more crucial dynamics we uncover. This is perhaps particularly true for developmental processes, where organization in time is the core of the problem. They also illustrate how

1

key technologies are now converging. On the one hand, advances in 3D microscopy and image analysis algorithms provide increasingly detailed views of cellular dynamics. On the other hand, rapid progress in genetic engineering and single cell sequencing yield more information on key regulators and markers of cell identity. With adjustments, these techniques are highly suited for application to the biology and biophysics of organoids, where study of temporal dynamics is still in its infancy. Together, these developments now provide an exciting opportunity to understand the underlying principles by which organs and organoids are organized in space and time.

While the studies reviewed here show that the main technologies are available, numerous improvements and extensions can be envisioned. At a practical level, more reliable automated tracking of cell movement and division would greatly expand the general use and throughput of cell tracking approaches. The development of new fluorescent reporters and sensors promises far more detailed observations of regulatory and metabolic pathways than is possible currently. Approaches that can link cell tracking to more expansive cell expression measurements, including multiplexed immunostaining, smFISH, and single-cell sequencing, have the potential to unlock a next level of understanding down to the molecular scale.

A general challenge will be to analyze the resulting lineage tracking data sets, given their complex, multi-faceted nature that combines space, time, lineage, and internal states. How can insight into simple organizing principles be inferred from such data sets? One approach could be to use machine learning techniques to identify the most relevant features informing cell fate decisions [1, 152, 169]. In addition, one may exploit dimensionality reduction techniques similar to ones used in the single cell sequencing and flow cytometry fields, which deal with similar highly dimensional single-cell resolved data, as they could identify hidden structures in the data. For instance, currently expressed cellular fate could be determined by past cell–cell contacts, cellular location, orientation, and molecular signals, while conversely, cellular migration speeds and spatial patterns may depend on cell type, age, and genealogical relations. Reduction techniques are already being used to analyze high throughput microscopy [22, 34] and recently have been used in the analysis of timeresolved imaging of whole organoids [139] and single cells in 2D culture [117]. Beyond the single cell level, recently developed methods allow statistical analysis of lineage trees shapes [151, 181] and simultaneously measured phenotypic signals [47, 66, 75, 144, 151]. In this way key differences between lineages may be identified and correlated with developmental decisions. However, it is likely that new analysis methods and the introduction of bottom-up mechanistic models are needed to make full use of the incredible richness of information that these new technologies can provide, and allow one to move from a descriptive to a predictive understanding of organ biology.

2

MOTHER CELLS CONTROL DAUGHTER CELL PROLIFERATION IN INTESTINAL ORGANOIDS

*G. Huelsz-Prince, R.N.U. Kok, Y.J. Goos, L. Bruens, **X. Zheng**, S.I. Ellenbroek, J. van Rheenen, S.J. Tans and J.S. van Zon*

During renewal of the intestine, cells are continuously generated by proliferation. Proliferation and differentiation must be tightly balanced, as any bias towards proliferation results in uncontrolled exponential growth. Yet, the inherently stochastic nature of cells raises the question how such fluctuations are limited. We used time-lapse microscopy to track all cells in crypts of growing intestinal organoids for multiple generations, allowing full reconstruction of the underlying lineage dynamics in space and time. Proliferative behavior was highly symmetric between sister cells, with both sisters either jointly ceasing or continuing proliferation. Simulations revealed that such symmetric proliferative behavior minimizes cell number fluctuations, explaining our observation that proliferating cell number remained constant even as crypts increased in size considerably. Proliferative symmetry did not reflect positional symmetry, but rather lineage control through the mother cell. Our results indicate a concrete mechanism to balance proliferation and differentiation with minimal fluctuations, that may be broadly relevant for other tissues.

2.1 Introduction

Most adult organs and tissues constantly renew themselves by replacing old and damaged cells, while retaining their structure [143]. Theory indicates that this homeostasis requires a precise balance between proliferating and non-proliferating cells, as even a slight systematic bias towards producing proliferating cells yields uncontrolled exponential cell growth [29, 76, 78, 83, 90, 125]. Moreover, the exponential nature of proliferation also readily amplifies fluctuations in the numbers of proliferating cells, which can lead to stochastic cell overgrowth or depletion in absence of additional control mechanisms [48, 157]. How cell proliferation is balanced despite fluctuations has remained challenging to test in direct experiments, given the difficulties of following this process in time.

The mammalian intestine has become an important model system to study the mechanisms of tissue renewal and homeostasis [52, 143]. The proliferating stem cells that sit at the base of intestinal crypts generate rapidly dividing transit-amplifying (TA) cells that in turn replenish the absorptive and secretory cells populating the lining of intestinal villi. Paneth cells positioned at the crypt bottom provide short-range signals that affect the proliferative and undifferentiated state of intestinal stem cells [45, 129, 140]. Originally, it was proposed that one or a few stem cells generated all differentiated cells by strictly asymmetric cell divisions [137, 177], thus directly ensuring a constant stem cell pool. Subsequent studies rather suggested that individual cells stochastically and independently cease to divide or not [90, 120, 145]. In this 'population asymmetry' model, in principle one stem cell daughter could remain proliferative by staying adjacent to a Paneth cell, while the other daughter exits the stem cell niche, differentiates, and stops proliferating. However, such asymmetric outcome is no longer guaranteed. Instead, proliferation and differentiation are balanced more indirectly, by averaging these stochastic events across the total stem cell population.

Observations of neutral drift, in which the offspring of a single cell randomly take over the stem cell population of intestinal crypts [90, 120, 145] established the stochastic nature of stem cell proliferation that distinguishes the population asymmetry model from the earlier division asymmetry model. However, approaches used thus far do not follow the underlying cell divisions and lineages in time. Proliferation symmetry between sister cells and its role in homeostasis of the intestinal epithelium have so far only been inferred indirectly, typically by quantifying the clone size distributions at a certain time point. Hence, we also lack insight into the fluctuations of the number of proliferating cells and the mechanisms that control them.

Here, we developed an alternative approach: we employed time-lapse microscopy and single-cell tracking of all cells in crypts of mouse intestinal organoids [130], thus providing complete lineage trees, division dynamics, and cell movement, and combine it with mathematical modelling and intravital imaging of the mouse intestine. Surprisingly, we found that most cell divisions (>90%) were symmetric in proliferative outcome, producing daughter cells that either both continued to proliferate or both ceased proliferating. Proliferation was symmetric even when one daughter neighbored a Paneth cell, the source of proliferative signals in the crypt, while the other did not. Hence, proliferation was not independent between sisters, but rather controlled through the lineage by the mother. Our data and simulations explained not only how this behavior achieves homeostasis, but more-

over, that it constitutes a near-optimal strategy to minimize fluctuations in the number of proliferating cells. Consistently, despite their large size increases over multiple generations in crypts of various size, the number of proliferating cells was notably constant in time and exhibited sub-Poissonian fluctuations, indicating a precise balance between proliferative and non-proliferative sister pairs. Finally, by measuring clone size distributions in mice, we showed that stem cell divisions *in vivo* reproduced the strong symmetry in proliferative behavior between sister cells seen in organoids. As cell proliferation in many tissues follows inherently stochastic 'population asymmetry' mechanisms [29, 37, 77, 145, 161], we conjecture that high symmetry in proliferative behavior, controlled through the lineage, may be a more general mechanism to limit proliferation fluctuations.

2.2 Results

2.2.1 Single-cell tracking of complete crypts in growing intestinal organoids

To examine the dynamics of individual cells within crypts during growth, we used organoids with a H2B-mCherry nuclear reporter (Fig. 2.1A) and performed confocal 3D time-lapse microscopy for up to 65 hours at a time resolution of 12 minutes. Cell division events were distinguished by the apical displacement of the mother cell nucleus, followed by chromosome condensation and separation, and finally, basal migration of the daughter cell nuclei (Fig. 2.1B), consistent with epithelial divisions [115]. Custom-written software was used to track every cell within organoid crypts by recording their nuclei positions in 3D space and time (Fig. 2.1C) and reconstruct lineage trees containing up to six generations (Fig. 2.1F, Fig. S2.1).

To study the cell lineages along the crypt surface, we 'unwrapped' the crypts: First, we annotated the crypt axes at every time point, then projected every cell position onto the surface of a corresponding cylinder, which we then unfolded (Fig. 2.1D,E). This allowed us to visualize the cellular dynamics in a two-dimensional plane defined by two coordinates: the position along the axis and the angle around the axis. We found that lineages starting close to the crypt bottom typically continued to proliferate and expand in cell number, while those further up in the crypt contained cells that no longer divided during the experiment, consistent with stem cells being located at the crypt bottom and terminal differentiation occurring higher up along the crypt axis (Fig. 2.1F). Lineages were also terminated by the death of cells, as observed by their extrusion into the lumen. This fate occurred more often in some lineages compared to others, and the frequency did not depend strongly on position along the crypt-villus axis. At the crypt bottom we also observed a small number of non-dividing cells, suggestive of terminally differentiated Paneth cells. Indeed, these cells typically exhibited the larger cell size and granules typical of Paneth cells.

2.2.2 Control of cell proliferation in organoid crypts

To systematically study proliferation control, we classified cells as proliferating when they divided during the experiment. Cells were classified as non-proliferating when they did not divide for longer than 30 hours or were born more than 60 μm away from the crypt bottom, as such cells rarely divided in our experiments (See Materials and Methods
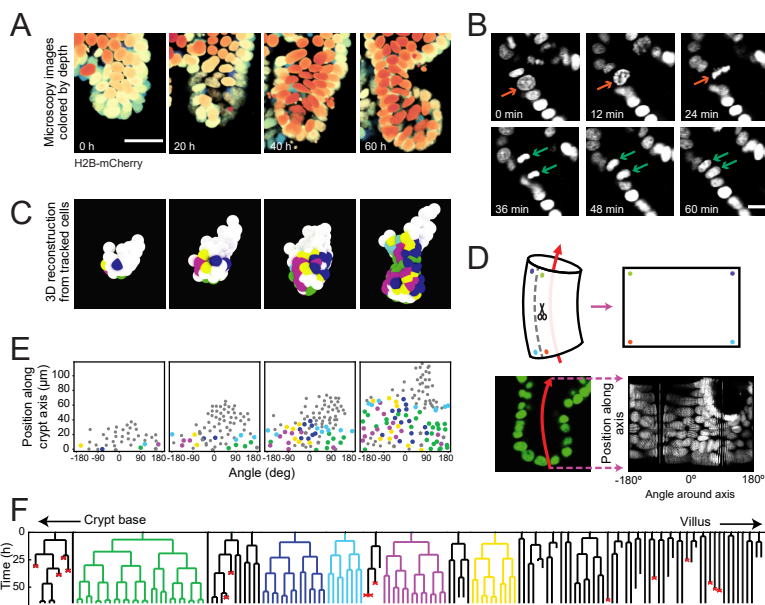
Fig 2.1: Time-lapse imaging and single-cell tracking of intestinal organoid crypts. (A) 3D reconstruction of an organoid expressing an H2B-mCherry reporter to visualize individual nuclei. Shown here is the crypt region, with nuclei colored by their depth along the optical axis. Scale bar is 25 μm. (B) Snapshots of a cell division event in a crypt. Cell divisions are distinguished by the apical migration of the nucleus followed by chromosome condensation (red arrows). After mitosis, the nuclei of the two newly born cells are displaced basally (green arrows). Scale bar is 10 μm. (C) 3D reconstruction of a crypt growing in time using the positions of tracked nuclei. Colors represent cells that belong to the same lineage. (D) Illustration of crypt unwrapping. After the crypt-villus axis is annotated (red arrow), tracked cell positions are projected onto the surface of a bent cylinder. The cylinder is then unfolded and its surface is mapped onto a two-dimensional plane defined by the distance along the axis and the angle around the axis. (E) Unwrapped representation of the crypt in (C), where colors represent the same lineages. (F) Lineage trees of cells within the crypt in (C) and colored accordingly. Cells in the initial time point are ordered according to their distance to the crypt base. Red crosses indicate cell deaths and incomplete lines indicate cells that could not be accurately traced further due to insufficient fluorescence intensity or movement outside of the field of view.

for details). A smaller fraction of cells could not be classified. Some cells were lost from tracking (7%, N=2880 cells). These cells were typically located in the villus region (Fig. 2.1F) and therefore likely non-proliferating. For other cells, the experiment ended before a division could be observed or excluded based on the criteria above (27%). Such cases were particularly prominent in the last 15 hours of each time-lapse data set (22%). To analyze proliferation control, we therefore excluded all cells born less than 15 hours before the end of each experiment, thereby reducing the fraction of unclassified cells to 10%.

Using this classification procedure, we then quantified the total number of cells born in the tracked cell lineages for nine crypts and found a strong (∽ 4-fold) increase in time (Fig. 2.2A). In contrast, the number of proliferating cells remained approximately constant in time for most crypts (Fig. 2.2B). Two crypts (crypt 3 and 4 in Fig. 2.2) formed an exception with ∽ 2-fold increase in the number of proliferating cells, an observation that we discuss

further below. We then estimated the exponential growth rate α for each crypt, by fitting the dynamics of total number of cells born and proliferating cell number to a simple model of cell proliferation (discussed further below as the Uniform model), where proliferating cells divide randomly into proliferating and non-proliferating cells. In this model, the number of proliferating and non-proliferating cells increase on average by α and $1-\alpha$ per cell division, respectively (Materials and Methods). Apart from Crypts 3 and 4, that displayed growth ($\alpha \approx 0.3$), the remaining crypts showed a low growth rate, $\alpha = 0.05 \pm 0.07$ (Fig. S2.2A-C), indicating that birth of proliferating and non-proliferating cells was balanced on average. We then quantified the magnitude of fluctuations in the number of proliferating cells, N. Calculations of birth-death models of cell proliferation show that, without any control, the standard deviation of the proliferating cell number grows in time without bounds as $\sigma_D \backsim \sqrt{Nt}$ [48]. In models without exponential growth, with proliferating cells born at constant rate, fluctuations are reduced: they are constant in time and Poissonian, $\sigma_D \backsim \sqrt{N}$ [159]. In models where exponential growth was controlled by homeostatic feedback loops, fluctuations were further reduced to sub-Poissonian: $\sigma_D < \sqrt{N}$ [157]. Using the same measures, we found here that most crypts exhibited sub-Poissonian fluctuations (Fig. S2.2D), implying the presence of a mechanism to limit fluctuations in proliferating cell number. Finally, we quantified the frequency of cell divisions along the crypt axis. Notably, divisions occurred in a region below 60 μm from the crypt base throughout the experiment, even as the crypts grew significantly (Fig. 2.2C), indicating that the size of the proliferative region was constant in time. Moreover, the proliferative region was found to have a similar size in all analyzed crypts (Fig. 2.2D), even though crypts varied both in size, as measured by diameter (30-50 μm, Fig. S2.2E), and number of proliferating cells (Fig. 2.2B). Overall, these results show that crypts by themselves are already capable of a specific form of homeostasis, namely maintaining a stationary number of proliferating cells that occupy a region of the crypt of constant size.

2.2.3 SYMMETRY OF PROLIFERATIVE BEHAVIOR BETWEEN SISTER CELLS

To examine the origin of the observed balance between the birth of proliferating and non-proliferating cells, we first examined whether cell proliferation or cell death were correlated between sisters, for all observed sister pairs S_1 and S_2 (Fig. 2.3A). Strikingly, we found that the decision to divide or not was highly symmetrical between sisters. In particular, occurrences where one sister divided but the other not were rare (2%) compared to cases where both divided or stopped dividing (74%). This correlation was also apparent by visual inspection of individual lineages, as sisters showed the same division behavior (Fig. 2.3B, top). Indeed, if we ignore cell death, the fraction of pairs with symmetric proliferative outcome was high (97%) and could not be explained by sister cells making the decision to proliferate or not independently ($P < 10^{-5}$, bootstrap simulation, Materials and Methods). We also compared lineage dynamics between all cousin pairs C_1 and C_2 (Fig. 2.3A). While we indeed found a significantly increased fraction (9%) of cousin pairs with asymmetrical division outcome, i.e. C_2 dividing and C_1 not, compared to sister pairs (2%), this fraction was still low, indicating that symmetric outcomes also dominated for cousins.

We found that symmetry between sisters did not only impact proliferation arrest, but also cell cycle duration: when a cell exhibited a longer-than-average cell cycle, this was typically mirrored by a similar lengthening of the cell cycle of its sister (Fig. 2.3B,

2
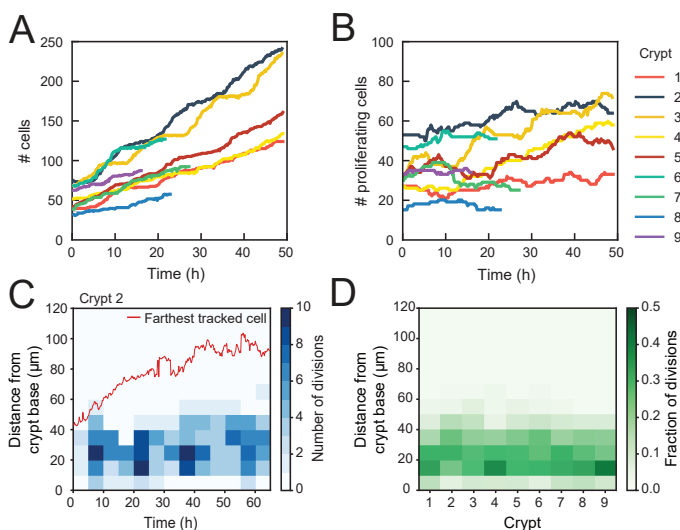
Fig 2.2: Control of cell divisions in intestinal organoids. (A) Total number of cells born and (B) number of proliferating cells as a function of time for all cell lineages followed in nine tracked crypts. Note the different scale along the y-axis. Cells that died were classified as non-proliferating. Whereas total cell number increases, the number of proliferating cells remains approximately constant. The strongest increase in number of proliferating cells (~2-fold) was seen in Crypts 3 and 4. (C) Number of divisions that occurred at different positions along the crypt axis as a function of time in a single tracked crypt. Red line corresponds to the position of the farthest tracked cell from the crypt base at every time point. Divisions occur in a compartment close to the crypt base, whose size remain constant over time. Apical displacement of the nuclei during mitosis results in few divisions occurring at less than 10 μm from the crypt base. (D) Fraction of divisions that occurred at different positions along the crypt axis for all tracked crypts, averaged over the full time course. The size of the proliferative region is similar between crypts, despite differences in the total number of divisions.

bottom). Indeed, cell cycle duration was strongly correlated between sisters (R=0.8, Fig. 2.3C), even as cell cycle duration showed a broad distribution among tracked cells (Fig. S2.3). In contrast, cell death was not symmetric between sisters, as the fraction of pairs where both cells died (0.09) was smaller than the fraction of pairs where only a single sister died (0.14, Fig. 2.3A).

When examining all sister pairs in our data set, pairs of dividing sisters (59%) outnumber pairs of non-dividing sisters (15%), which appeared at odds with the observation that in most crypts the number of proliferating cells remain approximately constant (Fig. 2.2B). This apparent mismatch was due to the exclusion of sister pairs where the proliferative state could not be classified in one sister or both (Fig. S2.4), as the majority of these unclassified cells were likely non-proliferating. Indeed, when we restricted our sister pair analysis to the cells of crypts with $\alpha \approx 0$ in Fig. 2.2A,B (Crypts 1,2,5,7-9) and furthermore assumed that all unclassified cells were non-proliferating, we found that now proliferating sister pairs (43%) are approximately balanced by non-proliferating sisters (40%, Fig. S2.4).
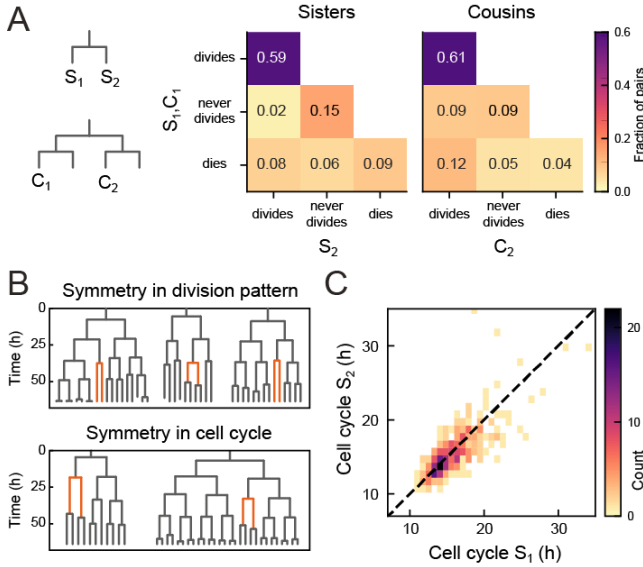
Fig 2.3: Symmetry of lineage dynamics between sister cells. (A) Correlations in division patterns between sister (S_1,S_2) and cousin cells (C_1,C_2) (n=1004 and 1304 sister and cousin cell pairs). Most sister pairs show symmetrical outcomes, with most pairs consisting of sisters that either both divide or both cease dividing. Cell death occurs at low frequency and impacts sister cells asymmetrically. Symmetrical outcomes are still dominant for cousins, but the fraction of pairs that exhibited asymmetric proliferative outcomes (C_1 never divides, C_2 divides) was significantly increased in cousins compared to sisters ($P = 2.4 * 10^{-7}$, Pearson's Chi Square Test). (B) Representative examples of measured lineages highlighting pairs of sister cells (orange) that differ in lineage dynamics from their more distant relatives (black), either in terms of proliferative behavior (top) or cell cycle duration (bottom). (C) Duration of sister cell cycles plotted against each other for pairs in which both sisters divided. Cell cycle duration is strongly correlated between sisters (R=0.80).

2.2.4 Symmetry between sisters minimizes fluctuations in a cell proliferation model

In principle, any combination of (a)symmetric divisions would yield a constant number of proliferating cells on average, as long as the birth of proliferating and non-proliferating cells is balanced. We therefore hypothesized that the observed dominance of symmetric divisions might have a function specifically in controlling fluctuations in the number of proliferating cells. To test this hypothesis, we used mathematical modelling. Mathematical models of intestinal cell proliferation have been used to explain observed clone size statistics of stem cells [33, 90, 120, 145], but so far not to examine the impact of division (a)symmetry on cell number fluctuations. We therefore examined simple stem cell models in which the degree of symmetry of sister cell proliferation could be tuned as an external parameter.

We first examined this in context of the canonical stochastic stem cell model [29], that we here refer to as the Uniform model. This model only considers cells as 'proliferating' or 'non-proliferating' (approximating stem and differentiated cells) and tissues that are

unbounded in size, while ignoring spatial cell distributions. The parameter ϕ describes the division symmetry, with $\phi = 1$ corresponding to purely symmetric divisions and $\phi = 0$ to purely asymmetric divisions. The growth rate α describes the proliferation bias, with $\alpha > 0$ indicating more proliferating daughters, and $\alpha < 0$ more non-proliferating daughters on average. In our simulations, cells either divide symmetrically to produce two proliferating cells with probability $\frac{1}{2}(\phi + \alpha)$ or two non-proliferating cells with probability $\frac{1}{2}(\phi - \alpha)$, while the probability to divide asymmetrically is $1 - \phi$ (Fig. 2.4A). The number of proliferating cells increases exponentially for $\alpha > 0$ or decreases exponentially for $\alpha < 0$ while homeostasis requires $\alpha = 0$ [29, 83] (Fig. 2.4B).

When varying the division symmetry ϕ while maintaining $\alpha = 0$, we found that fluctuations in the number of proliferating cells N were minimized for $\phi = 0$ (Fig. 2.4B, C), i.e. every division was asymmetric. In this scenario, the number of proliferating cells remains constant throughout each individual division by definition. Adding only a small fraction of symmetric divisions strongly increased the fluctuations in N. These fluctuations increased the risk of stochastic depletion, where all proliferating cells are lost, or uncontrolled exponential increase in cell number, as previously observed in simulations [157], with the probability of such events occurring increasing with ϕ (Fig. 2.4B,C). These trends are inconsistent with the symmetry between sisters we observed experimentally.

Hence, we extended the model by explicitly incorporating the observed subdivision of the crypt in a stem cell niche region, corresponding roughly to the stem cell niche, and a differentiation region, corresponding to the villus domain (Fig. 2.4D). In the niche compartment, which has fixed size S, most divisions generate two proliferating daughter cells ($\alpha_n > 0$), while in the differentiation compartment, which has no size constraints, most divisions yield two non-proliferative daughters ($\alpha_d < 0$). Cell divisions in the niche compartment results in expulsion of the distalmost cell into the differentiation compartment, while neighboring cells swap positions in the proliferative compartment with rate r to include cell rearrangements. In contrast to the uniform model, where homeostasis only occurred for $\alpha = 0$, the compartment model shows homeostasis with $\alpha_{n,d} \neq 0$ in either compartment. Specifically, we found that the average number of proliferating cells in the two compartments, N_n and N_d, is given by $N_n = \alpha_n S$ and $N_d = Sln(1 + \alpha_n)\frac{\alpha_d - \alpha_n}{\alpha_d} - \alpha_n S$, independent of the division symmetry ϕ [80]. We simulated the proliferation dynamics for different values of α_n, α_d and ϕ (Fig. 2.4E,F), where for simplicity we assumed the same ϕ in both compartments. For each combination of parameters, we varied the compartment size S so that $<N> = N_n + N_d = 30$, comparable to the number of proliferating cells per crypt in our experiments (Materials and Methods, Fig. S2.5A). For cell rearrangements, we used $r \cdot T = 1$, where T is the average cell cycle time, meaning that cells rearrange approximately once per cell cycle. For this r, our simulations reproduced the correlations in division outcome that we observed experimentally for cousins (Fig. S2.6A-C), although we found that the dependence of the dynamics of N on the parameters ϕ, α_n and α_d did not depend strongly on r (Fig. S2.6D).

By fixing $<N>$, all simulations maintained the same number of proliferating cells on average, but potentially differed in the magnitude of fluctuations. Indeed, we found parameter combinations that generated strong fluctuations (Fig. 2.4E,F, scenario 1) and stochastic depletion of all proliferating cells (scenario 2). Stochastic depletion occurred at significant rate (>1 event per 1000 hours) when $\alpha_n \lesssim 0.5$ (Fig. S2.5B) and implies that

the existence of a stem cell niche, defined as a compartment with $\alpha > 0$, by itself does not guarantee homeostasis, unless its bias towards proliferation is high, $\alpha \approx 1$. For fixed α_n and α_d, we observed that fluctuations in N always decreased with more asymmetric divisions $\phi \to 0$ (Fig. 2.4E,F, scenarios 2,3), similar to the uniform model. However, the global fluctuation minimum was strikingly different (Fig. 2.4E,F, scenario 4). Here, symmetric divisions dominated ($\phi = 1$), with all divisions generating two proliferative daughters in the niche compartment ($\alpha_n = 1$) and two non-proliferating daughters in the differentiation compartment ($\alpha_d = -1$). Similar low fluctuations were found for a broader range of α_d, provided that $\alpha_n \approx 1$. When we quantified the magnitude of fluctuations versus the average number of proliferating cells, we found that fluctuations for the suboptimal scenarios 1-3 were larger than those expected for a Poisson birth-death process (Fig. S2.2D). In contrast, fluctuations in the optimal scenario 4 were similar to the low fluctuations we observed experimentally.

Our simulations also provided an intuitive explanation for this global minimum. A bias $\alpha_n = 1$ is only reached when the birth of non-proliferating cells in the niche compartment, by symmetric or asymmetric divisions, is fully avoided. In this limit, all cells in this compartment are proliferating, meaning that fluctuations in the niche compartment are entirely absent, with the only remaining fluctuations due to cells ejected from the niche compartment that subsequently divide in the differentiation compartment. Consistent with this explanation, we found that fluctuations in N increased when more symmetric divisions in the niche compartment generated non-proliferating daughters (scenarios 1 and 2). Finally, we note that the well-established neutral drift model of symmetrically dividing stem cells in a niche of fixed size [90, 145] fails to reproduce the high symmetry in proliferation we experimentally observe between sister cells (Fig. S2.6E), indicating that the size constraint of a niche is by itself not sufficient to generate this symmetry. In conclusion, our simulations show that the dominance of symmetric divisions we observed experimentally might function to minimize fluctuations in cell proliferation.

2.2.5 Symmetry of proliferation is independent of Paneth cell distance

Our results raised the question how the strong symmetry in proliferative behavior between sister cells is generated. Stem cell maintenance and cell proliferation is control by signals such as Wnt and EGF, that in organoids are locally produced by Paneth cells [45, 129]. The symmetry between sister cells could therefore be explained by these sisters having a similar position relative to Paneth cells, leading them to experience a near identical environment in terms of proliferative signals. Alternatively, the proliferative behavior of sister cells could be controlled through the lineage, by their mother. In this case, symmetric proliferative behavior would even be seen in sisters that differ in position relative to Paneth cells. To differentiate between these two scenarios, we performed lysozyme staining after time-lapse imaging to retrospectively identify Paneth cells in our tracking data. Using crypt 'unwrapping' (Fig. 2.1D,E), we calculated for each cell and each time point the link distance δ to the closest Paneth cell (Materials and Methods, Fig. S2.7A,B), i.e. the number of cells between the cell of interest and its closest Paneth cell, allowing us to examine proliferative behavior as function of distance to Paneth cells.

Paneth cell-derived Wnt ligands form gradients that only penetrate 1-2 cells into the surrounding tissue [45], suggesting that the steepest gradient in proliferative signals is found in close proximity to the Paneth cell. We therefore selected all dividing mother cells directly adjacent to a Paneth cell ($\delta_M = 0$) and examined their daughters. These sister pairs varied in Paneth cell distance ($\delta_{1,2} \approx 0 - 2$, Fig. 2.5A, Fig. S2.7C), with differences between sisters ($\delta_1 \neq \delta_2$) seen in 42% of pairs. We classified each sister pair as asymmetric in outcome, when only one sister continued proliferating, or symmetric (Fig. 2.5B). In the latter case, we distinguished between symmetric pairs where both sisters divided and those were both stopped proliferating. We found that most daughters cells divided again, even though a small fraction ceased division even in close proximity to Paneth cells (Fig. 2.5B, Fig. S2.7D). However, whether cells divided or not was fully symmetric between sister pairs, even when one cell remained adjacent to a Paneth cell ($\delta_1 = 0$) while the other lost contact ($\delta_2 > 0$). This also held for the few pairs where Paneth cell distance differed most between sisters ($\delta_1 = 0$, $\delta_2 = 2$).

When we instead examined mother cells that just lost contact with a Paneth cell ($\delta_M = 1$), we found that their offspring stopped proliferating more frequently (Fig. 2.5C). While here we did find a substantial fraction of sister pairs with asymmetric outcome, for most pairs the outcome was still symmetric (92% of pairs), even for pairs that differed considerably in relative distance to the Paneth cell. Sister pairs with asymmetric outcome occurred more frequently for pairs with different Paneth cell distance ($\delta_1 \neq \delta_2$). For these pairs, however, the non-proliferating cell was the sister closest to the Paneth cell about as often as it was the more distant (5 and 3 pairs, respectively), indicating that position relative to the Paneth cell had little impact on each sister's proliferative behavior. Overall, these results show that the symmetry of proliferative behavior between sisters did not reflect an underlying symmetry in distance to Paneth cells, thus favoring a model where this symmetry is controlled by the mother cell.

2.2.6 Paneth cells control proliferative bias

Even though the proliferative behavior of sisters was not explained by their relative Paneth cell distance, we found that the bias towards proliferating daughters was clearly reduced when the Paneth cell distance of the mother increased (Fig. 2.5B,C). Our simulations showed that both division symmetry and proliferative bias are important parameters in controlling fluctuations in the number of proliferating cells, with fluctuations minimized when most divisions are symmetric ($\phi \approx 1$), biased strongly towards producing two proliferating daughters in one compartment ($\alpha \approx 1$) and two non-proliferating daughters in the other ($\alpha \approx -1$). To compare our experiments against the model, we therefore measured the frequency of each division class as function of the mother's Paneth cell distance, averaging over all positions of the daughter cells (Fig. 2.5D). Overall, cells had a broad range of Paneth cell distances (δ=0-10). Close to Paneth cells ($\delta \leq 1$), most divisions generated two proliferating daughters, while further away ($\delta > 1$), the majority yielded two non-proliferating cells. Asymmetry was rare and only occurred for δ=1-2. No divisions were seen for $\delta > 5$. When we used these measured frequencies to calculate α and ϕ as a function of Paneth cell distance (Fig. 2.5E), we found good agreement with the parameter values that minimized fluctuations in the model, with a niche compartment of strong proliferation close

to Paneth cells ($\alpha = 0.67, \delta \leq 1$) and a non-proliferative compartment beyond ($\alpha = -0.67$), while almost all divisions were symmetric ($\phi = 0.98$).

The compartment model also predicted that the number of proliferating cells increases linearly with size S of the niche compartment. Above, we observed that the number of proliferating cells differed between crypts (Fig. 2.2B). We therefore examined whether variation in number of proliferating cells between crypts could be explained by differences in Paneth cell number, in those crypts where we identified Paneth cells by lysozyme staining (Crypts 1-4). For the crypts that maintained a constant number of proliferating cells in time (Crypts 1-2), we found that differences in number of proliferating cells were well explained by differences in Paneth cell number. Moreover, in crypts with increasing number of proliferating cells (Crypts 3-4), we found that for Crypt 3 this change could be explained by an increase of Paneth cell number, due to cell divisions that generated Paneth cell sisters. In Crypt 4, however, proliferating cells increased in number without apparent Paneth cell proliferation. This crypt appeared to undergo crypt fission [84] at the end of the experiment, suggesting that during fission cell proliferation is altered without concomitant changes in Paneth cell number. For Crypts 1-3, the relationship between number of proliferating and Paneth cells was well-fitted by a linear function (Fig. 2.5F), consistent with the compartment model. The fitted slope of this line indicates that one Paneth cell maintains ~8 proliferating cells. This agrees with the observation in Fig. 2.5D that divisions are strongly biased towards proliferation only for cells within the first and second ring of cells around each Paneth cell. Taken together, these results show that Paneth cells control proliferation by tuning the proliferative bias of divisions that are otherwise symmetric in proliferative outcome.

2.2.7 In vivo LINEAGE TRACING CONFIRMS SYMMETRIC PROLIFERATIVE BEHAVIOR OF SISTER CELLS

Finally, we asked whether the symmetry of proliferative behavior between sister cells was also observed in intestinal (stem) cells *in vivo*. Studying lineage dynamics with the high spatial and temporal resolution we employed here is currently impossible *in vivo*. However, we found that clone size distributions, which can be measured *in vivo*, exhibited a clear signature consistent with symmetric divisions. Specifically, clone size distributions of lineages generated by the compartment model showed that enrichment of even-sized clones depended strongly on a high frequency of symmetric divisions (Fig. 2.6A). When we quantified clone size distributions for our organoid lineage data, by counting the number of progeny of each cell at the end of a 40 h time window, while sliding that window through our ~60 h data set, we indeed found that even clone sizes were strongly enriched compared to odd clone sizes (Fig. 2.6B). Both for organoid and model data, we still observed odd clone sizes even when virtually all divisions were symmetric in proliferative behavior. This reflected variability in the cell cycle duration, with odd clone sizes typically resulting from symmetric divisions where one daughter had divided, but the other not yet.

To measure clone size distributions in the small intestine *in vivo*, we stochastically induced heritable tdTomato expression in Lgr5+ stem cells using $Lgr5^{EGFP-ires-CreERT2}$; $R26_{LSL-tdTomato}$ mice. We activated Cre-mediated recombination by tamoxifen and examined tdTomato expression after 60 hours, similar to the timescale of our organoid

experiments, and imaged crypts with 3D confocal microscopy. Cre-activation occurred in one cell per ~10 crypts, indicating that all labeled cells within a crypt comprised a single clone. Indeed, we typically found a small number of tdTomato+ cells per crypt, of which most also expressed Lgr5-GFP (Fig. 2.6C). We then counted the number of tdTomato+ cells per crypt to determine the clone size distribution and found a clear enrichment of even clone sizes (Fig. 2.6D), with the overall shape of the distribution similar to that measured in organoids. Overall, these results indicated a dominant contribution of divisions with symmetric proliferative outcome also in the lineage dynamics of Lgr5+ stem cells *in vivo*.
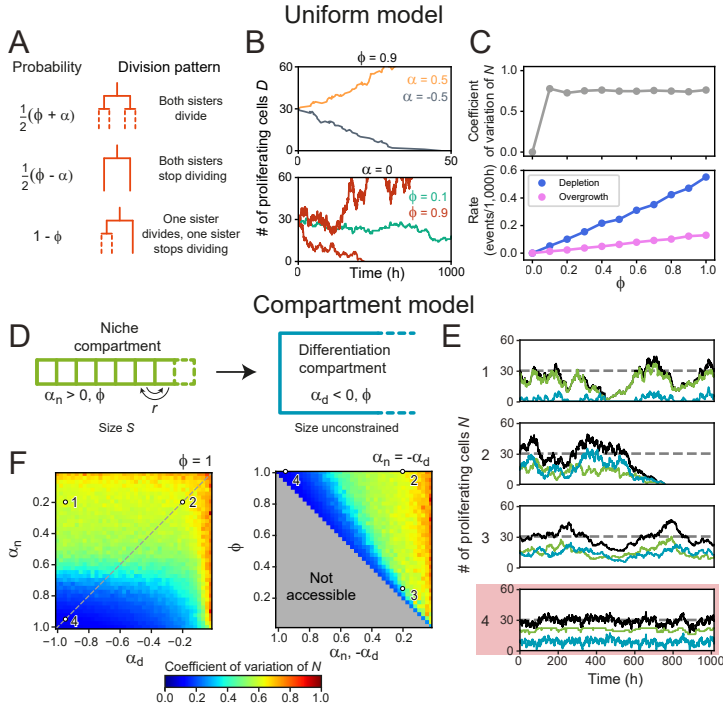
Fig 2.4: Cell number fluctuations in stem cell models. (A) 'Uniform' stem cell model. The probability of each division pattern depends on α, the average increase in the number of proliferating cells per division, and ϕ, the fraction of divisions with symmetric outcome, while the total cell number is unconstrained. (B) Number of proliferating cells, N, as function of time for different values of α (top) and ϕ (bottom). For $\alpha = 0$, N remains constant on average, yet in this case fluctuations can cause stochastic depletion or overgrowth of proliferating cells, as shown for $\phi = 0.9$ (bottom). (C) Coefficient of variation (standard deviation divided by mean) of N as a function of ϕ (top panel) and the probability of depletion ($N = 0$, blue) or overgrowth ($N \geq 150$, pink) events (bottom panel), for the 'Uniform' model with $\alpha = 0$. Frequency of overgrowth depends strongly on the threshold value used. Fluctuations are minimal for $\phi = 0$, i.e. only asymmetric divisions. (D) 'Compartment' model. Cells divide according to (A), but now the tissue is divided in a niche compartment n with $\alpha_n > 0$, and a differentiation compartment d, where $\alpha_d < 0$. Both compartments have the same ϕ. In the niche compartment, the total number of cells cannot exceed S, so that upon cell division the distalmost cell (dashed square) moves into the differentiation compartment. Cells in the niche compartment switch positions at rate r. (E) Number of proliferating cells as a function of time in the niche (green) and differentiation compartment (blue). The total number of proliferating cells (black) fluctuates around the dashed line corresponding to $< N >$. Each panel's number refers to the parameter sets shown in (F). The parameter set with lowest fluctuations is outlined in red. (F) Coefficient of variation of N. Left panel shows the effects of varying the growth rates of both compartments when all divisions are symmetric ($\phi = 1$), and right panel of varying the degree of symmetry when both compartments have opposite growth rates ($\alpha_n = -\alpha_d$, dashed line in top panel). The grey region in bottom panel is inaccessible parameter space. Simulations ran with $< N >= 30$, corresponding to our experimental observations, and rearrangements occurring approximately once per cell cycle. Fluctuations are minimized for $\alpha_n, -\alpha_d = 1$ and $\phi = 1$, i.e. only symmetric divisions.
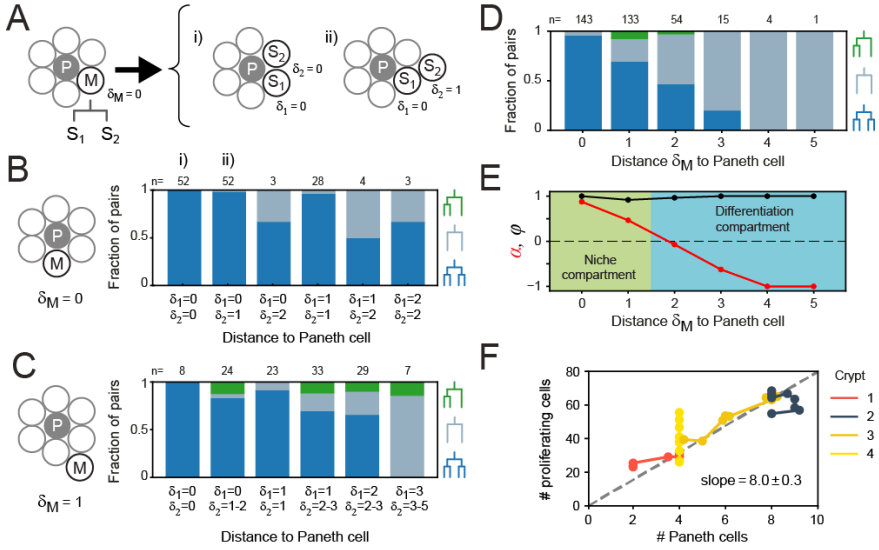
Fig 2.5: Impact of Paneth cell distance on proliferation. (A) Dependence of proliferation on contact with Paneth cells. We examined cases where a mother cell (M) that touched a Paneth cell (P) divided into sister cells, S_1 and S_2, that either retained or lost Paneth cell contact. Here, the link distances δ_1 and δ_2 represents the number of cells between each sister and its closest Paneth cell. (B) Probability that both cells divide (blue), neither cell divides (orange) or only a single cell divides (green) for all sister pairs S_1 and S_2 of which the mother touched a Paneth cell ($\delta_M = 0$). Sister pairs exhibited full symmetry in proliferative behavior, even when distance to the Paneth cell differed between sisters ($\delta_1 \neq \delta_2$). (C) Same as (B) but for a mother cell positioned one cell away from the Paneth cell ($\delta_M = 1$). More daughter cells cease proliferation. While the fraction of pairs where only one sister divides increases, most sisters exhibit symmetric behavior. (D) Probability of each division pattern as function of Paneth cell distance of the mother cell. (E) Proliferative bias α and degree of symmetry ϕ as a function of Paneth cell distance. The observed values of α define a proliferative (green, $\alpha \approx 1$) and non-proliferative (blue, $\alpha < 0$) compartment, with the former corresponding approximately to the first two 'rings' of cells surrounding the Paneth cell. (F) Number of proliferating cells as function of Paneth cell number. Time-courses for individual crypts were divided into 5 hour intervals (markers), for which average cell numbers were calculated. Apart from Crypt 4, Paneth cell number correlated well with number of proliferating cells, even when Paneth cell number increased in time due to divisions. Dashed line is a linear fit to the data.

2
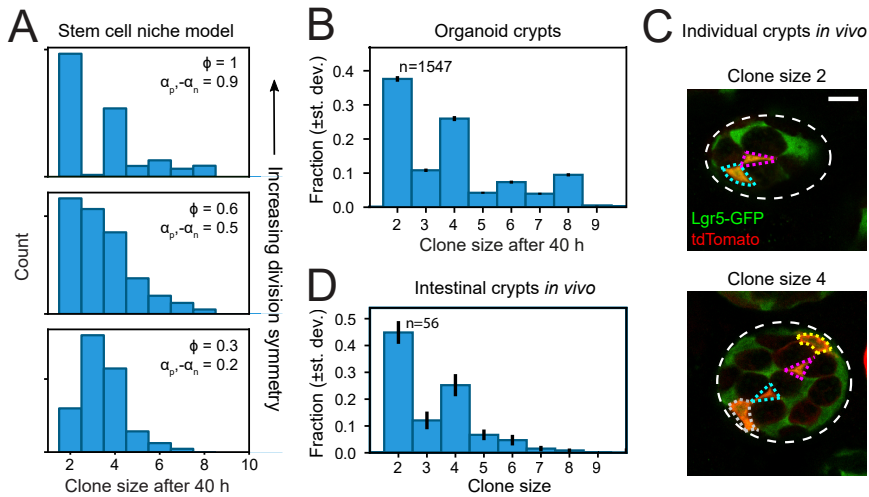
Fig 2.6: Clone size distributions reveal symmetry of proliferative behavior. (A) Clone size distributions calculated for the Compartment model, for different degrees of division symmetry ϕ. Top panel corresponds to parameters that minimize fluctuations in number of proliferating cells. For high division symmetry, $\phi \approx 1$, even clone sizes are enriched compared to odd clone sizes. (B) Clone size distributions calculated for the lineage data obtained in organoids, for a sliding window of 40 h. Even clone sizes are enriched, consistent with the observed dominance of divisions with symmetric proliferative outcome. Error bars indicate standard deviation calculated using a bootstrapping approach (Materials and Method). (C) Examples of individual crypts found *in vivo*, displaying clone size 2 (top) and 4 (bottom). Crypts are viewed from the bottom, with individual cells belonging to a tdTomato+ clone (red) outlined. Scale bar is 10 μm. (D) Clone size distributions measured *in vivo* 60 h after induction of Cre-mediated recombination in small intestinal crypts of $Lgr5^{EGFP-ires-CreERT2}$; $R26_{LSL-tdTomato}$ mice (n=160 crypts). Even clone sizes 2 and 4 are enriched compared to odd clone sizes 3 and 5.

2.3 Discussion

Self-renewing tissues exhibit homeostasis at multiple levels, such as overall tissue morphology, total cell number and the relative frequency of different cell types. To prevent exponential growth or tissue atrophy, the birth of each proliferating cell must be balanced by the loss of another through terminal differentiation. Experiments in a range of systems indicate that this is achieved through 'population asymmetry', with each cell making the decision to proliferate or not in a stochastic manner and this balance only achieved averaged over the entire population [29, 77, 143, 145]. However, our simulations showed that even though 'population asymmetry' ensures a constant pool of proliferating cells on average, its inherently stochastic nature can cause strong fluctuations in proliferating cell number, even resulting in their full depletion (Fig. 2.4). This raises the question how these fluctuations are controlled.

We addressed this by a combined experimental and theoretical approach. We tracked all cell movements and divisions in the crypts of growing intestinal organoids, to reconstruct the full lineage of these crypts up to six generations (Fig. 2.1). These data showed that the number of proliferating cells in most organoid crypts was approximately stationary, with small, i.e. sub-Poissonian fluctuations in their number, while non-proliferating cells were born at a constant rate (Fig. 2.2, Fig. S2.2), an indication of homeostatic control of cell proliferation that also limits fluctuations. That intestinal organoids exhibited homeostasis is notable, as organoid culture completely lacks surrounding tissue, such as the mesenchyme, that provides key signals regulating stem cell fate and proliferation [46, 140], and shows that this form of homeostasis is inherent to the epithelium itself.

Our simulations showed that the fluctuations in proliferating cell number depended strongly on the relative proportion of divisions with symmetric proliferative outcome (either two proliferating or two non-proliferating daughters) and asymmetric outcome (one proliferating and one non-proliferating daughter), with small, sub-Poissonian cell number fluctuations only seen when most divisions had symmetric outcome (Fig. 2.4, Fig. S2.2). So far, the relative contribution of these three divisions patterns in the intestine could only be inferred indirectly from static measurements, leading to conflicting results [70, 90, 138, 145]. Here, we used direct measurements of cell dynamics in time to unambiguously identify the proliferative state of successive generations of cells. These measurements show that virtually all cell divisions (>90%) showed symmetric proliferative behavior, generating either two proliferating or two non-proliferating sisters (Fig. 2.3). Clone size distributions calculated based on our measured lineage data in organoids showed that this symmetry in proliferative behavior between sister cell gave rise to an enrichment of even clone sizes (Fig. 2.6). Using short-term lineage tracing experiments in the mouse small intestine, we found that single Lgr5+ stem cells also gave rise to more even-sized than odd-sized clones, indicating that divisions that are symmetric in proliferative behavior indeed also dominate stem cell proliferation *in vivo*.

The symmetry in proliferative behavior we observe between sister cells could arise because both cells experience a highly similar environment, in terms of proliferative signals, or rather indicate control of cell proliferation through the lineage, by the mother cell. The current models of stem cell dynamics in the intestinal crypt favor a strong role for position relative to the stem cell niche, formed in organoids by Paneth cells, and a minor

role, if any, for control of cell proliferation through the lineage [90, 120, 145]. We found that sister cells exhibited symmetric proliferative behavior, even when sisters differed in distance to Paneth cells (Fig. 2.5), the sole source of proliferative Wnt signals in intestinal organoids [129]. This result implies control of proliferation by the mother cell rather than by each daughter's position in the stem cell niche. Our simulations provided a potential function for the predominance of divisions with symmetric proliferative outcome. When the tissue was subdivided into compartments of low and high cell proliferation, with the latter resembling the stem cell niche, we found that fluctuations in the number of proliferating cells were virtually eliminated, provided that cell divisions were symmetric, with all divisions generating two proliferating daughters in the niche compartment and two non-proliferating daughters outside (Fig. 2.4). Consistently, in our experiment we found that frequency of mother cells generating two proliferating rather than two non-proliferating daughters decreased with the mother's distance to the closest Paneth cell (Fig. 2.5). Taken together, our results suggest a model where differences in proliferative behavior emerges in the cell lineage over at least two generations: while a mother cell division generates two daughters with the same proliferative behavior, these daughters might subsequently generate granddaughters that differ in proliferative behavior, depending on each daughter's position relative to the Paneth cells. This is consistent with our observation that the symmetry of proliferative behavior between cousins is reduced significantly compared to sisters (Fig. 2.3).

We used mathematical modelling to explore the dependence of fluctuations in cell proliferation on the degree of symmetry in cell division outcome, arriving at a two-compartment model that matched key features of our experiments (Fig. 2.4D-F). It reproduced the observed low, sub-Poissonian fluctuations in number of proliferating cells (Fig. S2.2D), but only when division symmetry was high, as we also observed experimentally. In contrast, high symmetry increased fluctuations in a spatially uniform stem cell model (Fig. 2.4B,C), while a standard neutral drift model of a stem cell niche [90, 145] failed to reproduce the observed symmetry in outcome (Fig. S2.6). Our model also reproduced the observed correlation in proliferative state between cousin cells (Fig. S2.6), explaining it as arising from closely-related cells having similar location in the tissue and therefore similar probability of leaving the stem cell niche. Finally, it predicted the observed division of the tissue in a compartment where most divisions generated proliferating cells (close to Paneth cells) and one where divisions mostly generated non-proliferating daughters (away from Paneth cells) (Fig. 2.5). However, the simplified nature of our model also poses limits. First, the observed transition from proliferating to non-proliferating daughter cells was more gradual than predicted by the model, indicating that each divisions proliferative outcome depended on space in a more complex manner than captured by the model. Second, the existence of compartments and the degree of symmetry in division outcome is imposed externally by the model rules. It will be interesting to examine whether simple mathematical models can explain how these properties emerge from the internal cellular states, long-range signaling pathways and local cell-cell interactions involved in intestinal homeostasis [52, 143].

Precise control of cell proliferation is key to homeostasis. It has been proposed that cells may sense cell density, either by chemical signals or mechanical cues, and decrease cell proliferation (known as contact inhibition) if the cell number is too high [42, 83, 157],

thereby ensuring homeostasis of and minimize fluctuations in the number of proliferating cells. Here, we provide a mechanism that achieves this without explicit sensing of cell density. Instead, it relies on the dominance of divisions symmetric in proliferative behavior of the daughter cells, coupled with the organization of a tissue in a proliferative niche (stem and transit amplifying cell) compartment, and a non-proliferative differentiation compartment. Such an organization is found widely, e.g. in the skin, hair follicles, testis among others [87]. In all these tissues, homeostasis of and minimizing fluctuations in the number of proliferating and differentiated cells must be essential. Hence, we speculate that the model we propose here, which exploits proliferative symmetry between sister cells to minimize fluctuations, is conserved more broadly and relevant to diverse tissue systems.

2.4 Materials and methods

2.4.1 Organoid culture

H2B-mCherry murine intestinal organoids were a gift from Norman Sachs and Joep Beumer (Hubrecht Institute, The Netherlands). Organoids were cultured in basement membrane extract (BME, Trevingen) and overlaid with growth medium consisting of murine recombinant epidermal growth factor (EGF 50 ng/ml, Life Technologies), murine recombinant Noggin (100 ng/ml, Peprotech), human recombinant R-spondin 1 (500 ng/ml, Peprotech), n-Acetylcysteine (1 mM, Sigma-Aldrich), N2 supplement (1x, Life Technologies) and B27 supplement (1x, Life Technologies), Glutamax (2 mM, Life Technologies), HEPES (10 mM, Life Technologies), Penicilin/Streptomycin (100 U/ml 100 $\mu g/ml$, Life Technologies) in Advanced DMEM/F-12 (Life Technologies). Organoid passaging was performed by mechanically dissociating crypts using a narrowed glass pipette.

2.4.2 Time-lapse imaging

Mechanically dissociated organoids were seeded in imaging chambers one day before the start of the time-lapse experiments. Imaging was performed using a scanning confocal microscope (Nikon A1R MP) with a 40x oil immersion objective ($NA = 1.30$). 30 z-slices with 2 μm step size were taken per organoid every 12 minutes. Experiments were performed at 37°C and 5% CO_2. Small but already formed crypts that were budding perpendicularly to the objective were selected for imaging. Imaging data was collected for 3 independent experiments.

2.4.3 Fluorescent staining

After time-lapse imaging, organoids were fixed with 4% formaldehyde (Sigma) at room temperature for 30 minutes. Next, they were permeabilized with 0.2% Triton-X-100 (Sigma) for one hour at 4°C and blocked with 5% skim milk in TBS at room temperature for one hour. Subsequently, organoids were incubated in blocking buffer containing primary antibody (rabbit anti-lysozyme 1:800, Dako #A0099) overnight at 4°C, and then incubated with secondary antibody (anti-rabbit conjugated to Alexa Fluor ©405 1:1,000, Abcam #ab175649) at room temperature for one hour. Afterwards, they were incubated with wheat germ agglutinin (WGA) conjugated to CF ©488A (5 $\mu g/ml$ Biotium) at room temperature for two hours, followed by incubation with $RedDot^{TM}1$ Far-Red Nuclear Stain (1:200, Biotium) at room temperature for 20 minutes. Finally, organoids were overlaid with mounting medium (Electron Microscopy Sciences). The procedure was performed in the same imaging chambers used for time-lapse imaging in order to maintain organoids in the same position. Imaging was performed with the same microscope as previously described. Note that WGA stains both Paneth and Goblet cells, but the lysozyme staining allowed the unequivocal distinction between them.

2.4.4 Single-cell tracking

Cells were manually tracked by following the center of mass of their nuclei in 3D space and time using custom-written image analysis software. Each cell was assigned a unique label at

the start of the track. For every cell division, we noted the cell labels of the mother and two daughter cells, allowing us to reconstruct lineage trees. We started by tracking cells that were at the crypt bottom in the initial time point and progressively tracked cells positioned towards the villus region until we had covered all cells within the crypt that divided during the time-lapse recording. We then tracked at least one additional row of non-dividing cells positioned towards the villus region. Cell deaths were identified either by the extrusion of whole nuclei into the organoid lumen or by the disintegration of nuclei within the epithelial sheet. Only crypts that grew approximately perpendicularly to the imaging objective and that did not undergo crypt fission were tracked. During imaging, a fraction of cells could not be followed as they moved out of the microscope's field of view or moved so deep into the tissue that their fluorescence signal was no longer trackable. Because these cells were predominantly located in the villus region, where cells cease division, this likely resulted in underestimation of non-proliferating cells. Data was discarded when a large fraction (> 25%) of the cells in the crypt move out of the imaged volume.

2.4.5 Classifying cell state

To classify cells as either proliferating or non-proliferating, we followed the following procedure. Defining proliferating cells was straightforward, as their division could be directly observed. As for non- proliferating cells, we applied two criteria. First, cells were assigned as non-proliferating when they were tracked for at least 30 hours without dividing. This was based on our observation that cells cycle times longer than 30 hours were highly unlikely (P=$7.1 * 10^{-7}$, from fit of skew normal distribution, Fig. S2.3). However, we were not able to track all cells for at least 30 hours, as cells moved out of the field of view during the experiment or, more frequently, because they were born less than 30 hours before the end of the experiment. In this case, we defined a cell as non-proliferating if its last recorded position along the crypt axis was higher than 60 μm, as almost no divisions were observed beyond this distance (Fig. 2.2). Finally, cells were assigned as dying based on their ejection from the epithelium, while the remaining unassigned cells were classified as undetermined and not included in the analysis.

We tested the accuracy of this approach as follows. In data sets of >60 hours in length, we selected the subset of all cells for which we could with certainty determine proliferative state, either because they divided or because they did not divide for at least 40 hours. We then truncated these data sets to the first 40 hours, which reduced the number of cells whose proliferative state we could identify with certainty, and instead determined each cells proliferative state based on the above two criteria. When we compared this result with the ground truth obtained from the >60 hour data sets, we found that out of 619 cells, we correctly assigned 141 cells as non-proliferative and 474 as proliferative. Only 4 cells were incorrectly assigned as non-dividing, whereas they were seen to divide in the >60 hour data sets.

2.4.6 Estimation of significance of symmetric divisions

To estimate whether the experimentally observed fraction of sisters with symmetric division outcome could be explained by sister deciding independently to proliferate further or not, we used a bootstrapping approach. In our experimental data, we identified n=499 sister

pairs, where the proliferative state of each cell was known and excluding pairs where one or both sisters died. In this subset of sisters the probability of a cell dividing was found to be $p = 0.79$. For N=105 iterations, we randomly drew n sister pairs, which each cell having probability p to be proliferative and $1 - p$ to cease proliferation. For each iteration, we then calculated the resulting symmetry fraction ϕ. This resulted in a narrow distribution of ϕ with average ±st.dev. of 0.67±0.02, well-separated from the experimentally observed value of ϕ=0.97. In particular, none of 105 iterations resulted in a value $\phi \geq 0.97$, leading to our estimated P-value of P<10^{-5}. Overall, this means that the high fraction of sisters with symmetric division outcome reflects correlations in sister cell fate.

2.4.7 Estimation of crypt growth rate

To estimate an effective growth rate from the time dynamics of the total cell number and number of proliferating cells for each individual crypt, we used the 'Uniform' model as defined in the main text. Here, each generation the number of proliferating cells increases by αN, and the number of non-proliferating cells, M, changes by $(1 - \alpha)N$, where α is the growth rate with $-1 \leq \alpha \leq 1$. For α sufficiently close to zero, the resulting dynamics of the number of proliferating and non-proliferating cells, N and M, is given by $\frac{dN}{dt} = \frac{\alpha}{T}N$ and $\frac{dM}{dt} = \frac{1-\alpha}{T}N$, where T is the average cell cycle duration. Solving these differential equations yields $N(t) = N(0)e^{\frac{\alpha t}{T}}$ and $U(t) = M(0) - \frac{1-\alpha}{\alpha}N(0) + \frac{N(0)}{\alpha}e^{\frac{\alpha t}{T}}$ for the total number of cells, where $U = N + M$. We then fitted $N(t)$ and $U(t)$ to the experimental data in Fig. 2.2A,B, using a single value of the fitting parameter α for each crypt and the experimentally determined value of $T = 16.2h$.

2.4.8 Crypt unwrapping

At every time point the crypt axis was manually annotated in the xy plane at the z position corresponding to the center of the crypt, since tracked crypts grew perpendicularly to the objective. Three to six points were marked along the axis, through which a spline curve $\mathbf{s}(r)$ was interpolated. Then, for each tracked cell i we determined its position along the spline by finding the value of r that minimized the distance d between the cell position $\mathbf{x}_i$ and the spline, i.e. $d(r_i) = min_r|\mathbf{s}(r) - \mathbf{x}_i|$. At each time point, the bottom-most cell of the crypt, i.e. that with the lowest value of r_i, was defined as position zero. Thus, the position along the axis p_i for cell i was defined as $p_i = r_i - min_i(r_i)$. To determine the angle around the axis θ_i for cell i, we considered a reference vector $\mathbf{u}$ pointing in the direction of the imaging objective, given by $\mathbf{u} = (0, 0, -1)$, and the vector $\mathbf{v}_i = \mathbf{x}_i - \mathbf{s}(r_i)$ defined by the position of the cell $\mathbf{x}_i$ and the position of minimum distance along the spline $\mathbf{s}(r_i)$. Then, the angle is given by $\theta_i = acos((\mathbf{u} \cdot \mathbf{v}_i)/uv)$.

2.4.9 Distance to Paneth cells

To estimate the distance between cells we used the following approach. For each cell at each time point we found the five closest cells within a 15 μm radius, which became the edges in a graph representation of the crypt (Fig. S2.6). These values were chosen because a visual inspection revealed an average nucleus size of 10 μm and an average of five neighbors per cell. This graph was then used to define the edge distance of a cell to

the nearest Paneth cell. At every time point during the lifetime of that cell, the minimum number of edges required to reach the nearest Paneth cell was recorded. The edge distance is then defined as the number of edges minus one. For example, a neighbor cell of a Paneth cell (1 edge) has a distance of zero. When the edge distance of a cell to a Paneth cell varied in time, we used the mode of its distance distribution, i.e. the most frequently-occuring value, as recorded during its lifetime.

2.4.10 *IN VIVO* CLONAL TRACING

All experiments were carried out in accordance with the guidelines of the animal welfare committee of the Netherlands Cancer Institute. $Lgr5^{EGFP-ires-CreERT2}$; $R26_{LSL-tdTomato}$ double heterozygous male and female mice (Bl6 background) were housed under standard laboratory conditions and received standard laboratory chow and water ad libitum prior to start of the experiment. 60 hours before sacrifice, mice received an intraperitoneal injection with 0.05 mg tamoxifen (Sigma, T5648; dissolved in oil) resulting in maximally 1 labeled cell per 10 crypts. After sacrifice, the distal small intestine was isolated, cleaned and flushed with ice cold PBSO, pinned flat and fixed for 1.5 hours in 4% PFA (7.4 pH) at $4°C$. The intestine was washed in PBT (1% Tween-20) for 10 min at $4°C$ after which it was cut into pieces of 2 cm and transferred to a 12 well plate for staining. The pieces were permeabilized for 5 hours in 3% BSA and 0.8% Triton X-100 in PBSO and stained overnight at $4°C$ using anti-RFP (Rockland, 600-401-379) and anti-GFP (Abcam, ab6673) antibodies. After 3 times 30 min washes at $4°C$ in 0.1% Triton X-100 and 0.2% BSA in PBSO, the pieces were incubated with Alexa fluor Donkey anti rabbit 568 (Invitrogen, A10042) and Alexa fluor Donkey anti goat 488 (Invitrogen, A11055) secondary antibodies overnight at $4°C$. After an overnight wash in PBT, the pieces were incubated with DAPI (Thermo Fisher Scientific, D1306) for 2 hour and subsequently washed in PBS for 1 hour at $4°C$. Next, the intestinal pieces were cleared using 'fast light-microscopic analysis of antibody-stained whole organs' (FLASH)[100]. In short, samples were moved to an embedding cassette and dehydrated in 30%, 75%, 2x 100% MetOH for 30 min each at room temperature. Subsequently, samples were put into MetOH in a glass dish and immersed in methyl salicylate diluted in MetOH: 25%, 75%, 2x 100% methyl salicylate (Sigma-Aldrich) 30 min each at room temperature protected from light. Samples were mounted in methyl salicylate in between two glass coverslips and images were recorded using an inverted Leica TCS SP8 confocal microscope. All images were collected in 12 bit with 25X water immersion objective (HC FLUOTAR L N.A. 0.95 W VISIR 0.17 FWD 2.4 mm). Image analysis was carried out independently by two persons. Afterwards, all discrepancies between both datasets were inspected, resulting in a single dataset. Each biologically stained cell was annotated once in the 3D-dimensional image. Different cells in the same crypt were marked as belonging to the same crypt, which is necessary to calculate the clone size for that crypt. Only crypts that were fully visible within the microscopy images were analyzed.

2.4.11 UNCERTAINTY ESTIMATION IN CLONE SIZE DISTRIBUTIONS

In organoids, the clone sizes are measured by calculating the number of offspring the cell will have 40 hours later. This calculation is performed for every hour of the time lapse, up to 40 hours before the end. *In vivo*, clone sizes are measured once per crypt, as we cannot view

the dynamics over time. To estimate the uncertainty in our clone size distribution, both in organoids and *in vivo*, we use a bootstrapping approach. We denote the total number of clones observed as N. We then used random resampling with replacement, by drawing N times a random clone from the data set of observed clones, to construct a new clone size distribution. We ran this procedure 100 times, each run storing the measured fraction of clones sizes. As a result, for every clone size we obtained a distribution of fractions, which we used to calculated the standard deviation of the fraction, as a measure of sampling error.

2.4.12 Computational model

Simulations were initialized by generating a collection of proliferating cells, each belonging to either the niche or differentiation compartment. For each parameter combination, the initial number of proliferating cells assigned to each compartment was obtained by rounding to the closest integer the values given by the equations for N_n and N_d in the main text. When the initial number of proliferating cells in the niche compartment was lower than the compartment size S, they were randomly distributed over the compartment, with the remaining positions taken up by non-proliferating cells in order to fill the compartment. Each proliferating cell c that was generated was assigned a current age A_c and a cell cycle time C_c, i.e. the age at which the cell will eventually divide. The current age was obtained by randomly drawing a number from an interval ranging from 0 hours to the mean cell cycle time obtained from experimental data, while the cell cycle was obtained by drawing a random number from a skew normal distribution, which was fitted to the experimental distribution of cell cycle times as shown in Fig. S2.3.

   Simulations were performed by iterating the following routine over time, until a total simulation time $T_{sim} = 10^6 h$ was reached. At each iteration i, we found the cell c_i that was due to divide next, and a time step Δt_i was defined by the time remaining for this cell to divide, i.e. $\Delta t_i = min_c(C_c - A_c)$. Then, the ages of all proliferating cells were updated and the division of cell c_i was executed. This was done by randomly choosing one of the three division modes defined in Fig. 2.4C, according to the probabilities determined by the parameters α and ϕ of the compartment to which the cell belonged. Any proliferating daughters that were born were initialized with age zero and a random cell cycle time drawn as described before. For the two-compartment model, if the proliferating cell belonged to the niche compartment, the distalmost cell within this compartment was transferred to the differentiation compartment, without changes to its proliferative state. This means that a proliferating cell that is transferred to the differentiation compartment will still divide, with the symmetry only determined by ϕ, even if α_d=-1, i.e. all divisions in the differentiation compartment generate non-proliferating daughters. This corresponds to the assumption that the decision to proliferate or not, as well as the symmetry between the resulting daughters, is set by the external environment (niche or differentiation compartments) the cell experiences at birth and cannot be reversed at a later point. Finally, the number of proliferating and non-proliferating cells in each compartment was updated accordingly. Cell rearrangements were implemented as follows. For each iteration i, with time step Δt_i, we drew the number of cell rearrangements from a Poisson distribution with mean $(r \cdot S)\Delta t_i$, where r is the rearrangement rate per cell. We then implemented each individual rearrangement by randomly selecting a cell at position $j \in (0, S-1)$ and swapping it with the cell at position $j+1$.

2

The model had six parameters, of which three $(\alpha_n, \alpha_d, \phi)$ were systematically varied in our simulations. The remaining parameters were constrained by the experiments. We picked the niche size S so that the total number of proliferating cells was 30, corresponding to the typical number of dividing cells observed in the experiments, through a procedure outline in the main text. We obtained the average cell cycle duration T, as well as its distribution, from the data in Fig. S2.3. Finally, we obtained the rearrangement rate r from the observed (a)symmetry in proliferative fate observed between cousin cells. For a 'well-mixed' niche compartment, $r \cdot T \gg 1$, cousin pairs showed asymmetric outcome as often as symmetric outcome (Fig. S2.6), in contrast to our experimental observations (Fig. 2.3A). In contrast, for infrequent cell rearrangement, $r \cdot T = 1$, cells expelled from this compartment close together in time are also closely related by lineage, leading to correlations in division outcome between cousins that reproduced those observed experimentally (Fig. S2.6, Fig. 2.3A).

For some parameter values, simulations were ended earlier than the total time T_{sim}. This occurred when no proliferating cells were left in either compartment (defined as a depletion event), or when the number of proliferating cells reached an arbitrarily set maximum limit of five times its initial value (defined as an overgrowth event, occurring only in the one-compartment model). In these cases, simulations were restarted until a total simulation time T_{sim} was reached, and the total number of events was recorded. Thus, the rate of depletion or overgrowth refers to the number of times simulations had to be restarted for each value of ϕ divided by the total simulation time.

To obtain statistics regarding fluctuations on the number of proliferating cells N through time, at each iteration i we kept track of the number of proliferating cells in the niche compartment d_i^n and in the differentiation compartment d_i^d. With these quantities, we could compute the standard deviation σ of N according to $\sigma^2 = \langle N^2 \rangle - \langle N \rangle^2$. Given that $N = N_n + N_d$, where N_n and N_d are the number of proliferating cells in the niche and differentiation compartments, σ can be expressed as $\sigma^2 = \langle N_n^2 \rangle - \langle N_n \rangle^2 + \langle N_d^2 \rangle - \langle N_d \rangle^2 + 2\langle N_n N_d \rangle - 2\langle N_n \rangle \langle N_d \rangle$, where $\langle N_{n,d} \rangle = \sum_i \frac{d_i^{n,d} \Delta t_i}{T}$, $\langle N_{n,d}^2 \rangle = \sum_i \frac{(d_i^{n,d})^2 \Delta t_i}{T}$ and $\langle N_n N_d \rangle = \sum_i \frac{d_i^n d_i^d \Delta t_i}{T}$.

2.5 SUPPLEMENTARY FIGURES
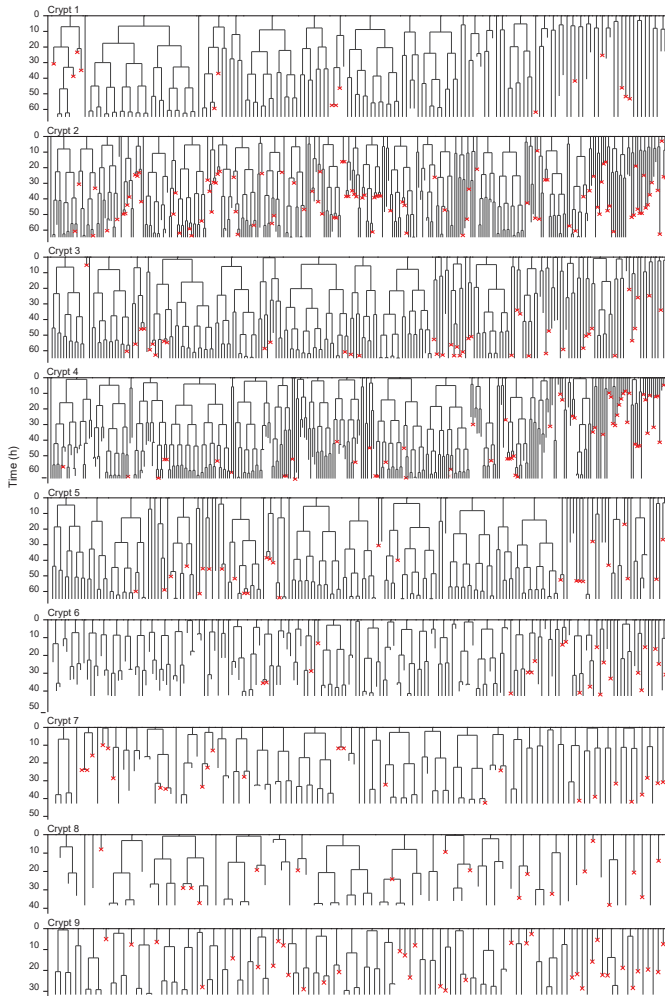
Fig S2.1: Lineage trees of all tracked cells. Lineage trees of cells tracked in nine different crypts. Cells in the initial time point are ordered according to their distance to the crypt base. Red crosses indicate cell deaths and incomplete lines indicate cells that could not be accurately traced further due to insufficient fluorescence intensity or movement outside of the field of view.

2
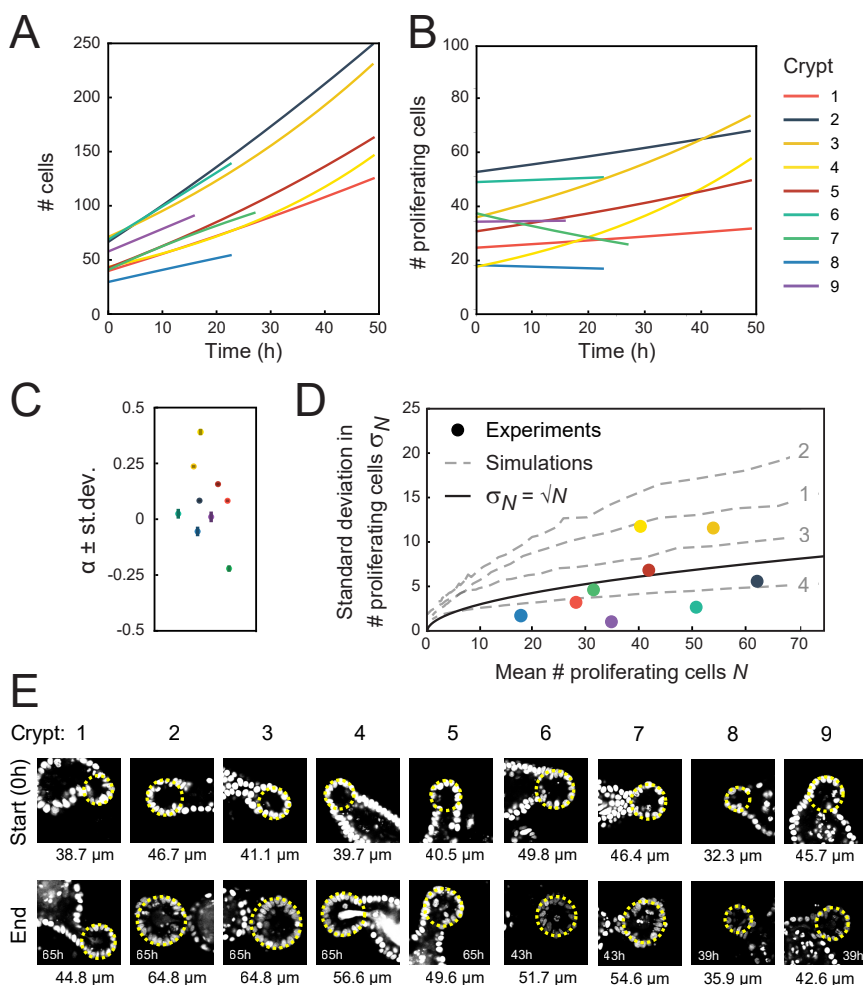
Fig S2.2: Crypt growth and heterogeneity. (A),(B) Fits of a simple cell proliferation model (Materials and Methods) to the experimental data in Fig. 2.2A,B. Each fit to the total number of cells (A) and number of proliferating cells (B) yields a single fitted value of the exponential growth rate α. (C) Fitted values of α, with the color of each marker corresponding to the crypts in (A),(B). Two crypts exhibited significant growth (crypts 3 and 4, $\alpha \geq 0.25$) while one crypt show decay in proliferating cell number (crypt 7, $\alpha = -0.25$). For most of the remaining crypts, α deviated significantly from zero, but otherwise the fitted growth was low. For this reason, the reported average growth rate in the main text excluded crypts 3,4 and 7. Including crypt 7 yields $\alpha = 0.0 \pm 0.1$. Error bars are the standard deviation in the fit of α. (D) Standard deviation of the number of proliferating cells, σ_D, versus the average, D, for each crypt, with color indicating crypts as in (A),(B). Black line shows the relationship expected for a Poisson birth-death process, $\sigma_D = sqrtD$. For crypts that exhibited growth (crypt 3 and 4), σ_D was larger than a Poisson process, while other crypts showed fluctuations close to or below what was expect for a Poisson process, implying that fluctuations were limited by some form of homeostatic control. Grey dashed lines show the same analysis for simulations of the 'Compartment' model (Fig. 2.4D), with individuals lines corresponding to the different scenarios 1-4 (indicated in grey) in Fig. 2.4E,F. For the suboptimal scenarios 1-3, fluctuations are larger than Poissonian, while the optimal scenario 4 reproduced the low fluctuations observed experimentally. (E) Fluorescence images of analyzed crypts 1-9 at the start and end of the experiment. Duration of the experiment is indicated in each 'end' panel. Diameter of the crypt at the start and end of the experiment is calculated by overlaying a circle (yellow line) over the z-slice at the center of the crypt. Overall, crypts display heterogeneity both in initial crypt size and growth of crypt diameter.

A

B
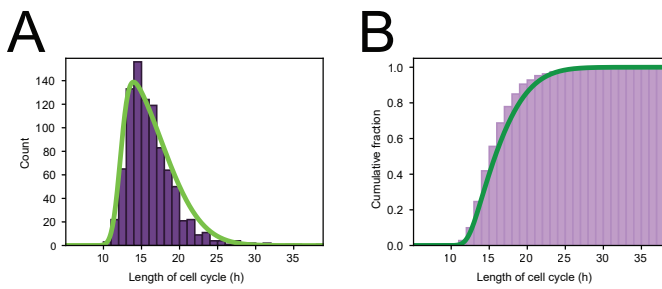
Fig S2.3: Cell cycle distribution. (A) Histogram of cell cycle times of all tracked dividing cells. Green line represents a skew normal distribution fitted to the data, with parameters: shape = 6.1, location = 12.2 h, and scale = 5.2 h. (B) Cumulative version of the histogram of panel (A).
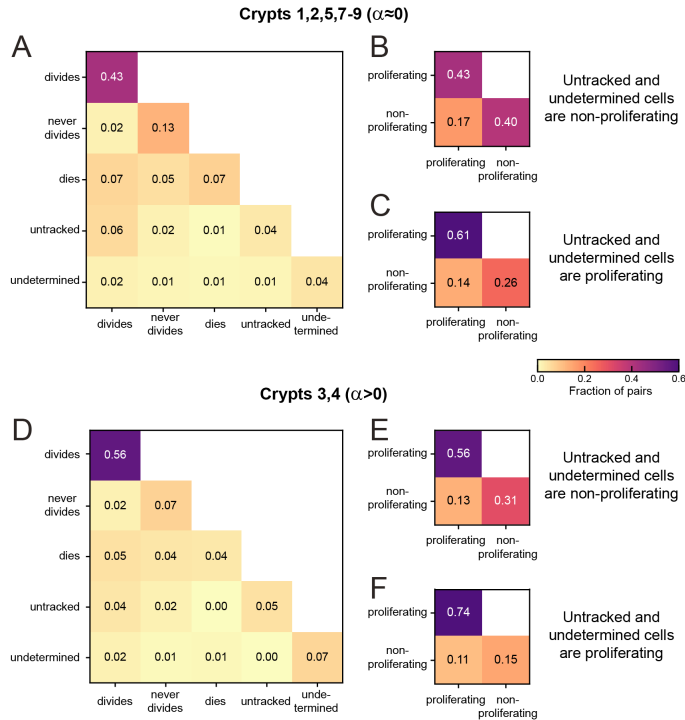
Fig S2.4: Sister pair divisions patterns and proliferation control. (A) Correlations in division patterns between sister pairs (S_1,S_2), for all cells born at least 15 h prior to the end of the experiment in crypts that exhibited low growth rate $\alpha \approx 0$ in Fig. S2.2B,C (Crypts 1,2,5,7-9). Sister pair fractions are also included for cells that were lost from cell tracking (untracked) or cells that could be tracked but where the experiment ended before a division could be observed or excluded (undetermined). (B) Fraction of sister pairs with proliferating and/or non-proliferating cells, under the assumption that untracked and undetermined cells are non-proliferating. This assumption matches our observation that untracked cells are located almost exclusively in the villus, where cells are less likely to proliferate, and that undetermined cells older than 15 h are most likely non-proliferating according to Fig. S2.3. Cells that died were classified as non-proliferating, as in Fig. 2.2A,B. Under this assumption, the fraction of symmetrically proliferating (43%) and non-proliferating sisters (40%) is approximately equal, consistent with constant number of proliferating cells and low growth rate α in Fig. 2.2A,B and Fig. S2.2B,C. (C) Fraction of sister pairs with proliferating and/or non-proliferating cells, under the assumption that all untracked and undetermined cells proliferate. Under this assumption, which is not supported by our experiments, the fraction of symmetrically proliferating (61%) and non-proliferating sisters (26%) is still relatively close to balanced, implying that the balance in proliferation observed in (B) is likely not impacted strongly if a small fraction of untracked or undetermined cells would have been proliferating. (D) Same as (A) but for crypts that exhibited an increase in number of proliferating cells (α>0, Crypts 3,4). (E),(F) Same as (B),(C) but for Crypts 3 and 4. Symmetrically proliferating sisters (56%) outnumber non-proliferating sisters (31%) even under the assumption that all untracked and undetermined sisters are non-proliferating, consistent with the growth in proliferating cells observed in these crypts.

2
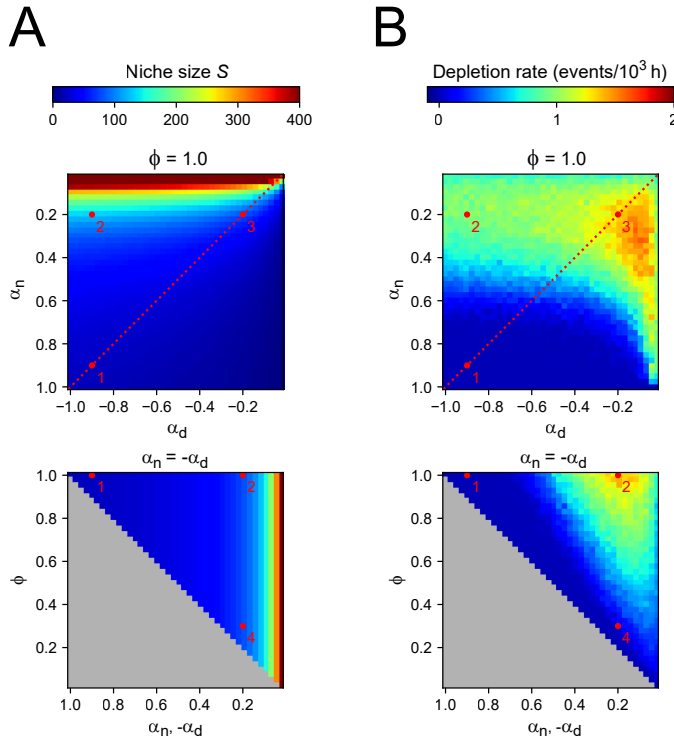
Fig S2.5: Two-compartment model. (A) Number of cells S in the niche compartment, as function of model parameters in the Compartment model. Top panel shows the effects of varying the bias towards proliferative daughters of the niche and differentiation compartments (α_n and α_d, respectively) when all divisions are symmetric ($\phi = 1$), and bottom panel shows the effects of varying the degree of symmetry when these compartments have opposite growth rates ($\alpha_n = -\alpha_d$, dashed line in top panel). The grey region in bottom panel corresponds to inaccessible parameter space. Numbers correspond to the parameter sets highlighted in Fig. 2.4 in the main text. (B) Rate at which proliferating cells were depleted. Every time a simulation ended due to depletion, i.e. all remaining cells are non-proliferating, a new simulation was started until a total simulation time of 10^6 hours was reached. Thus, the rate refers to the number of times simulations had to be restarted for each value of the parameters divided by the total simulation time. Spontaneous overgrowth was only observed in cases where α_n and α_d are both close to 0, in which case the rate was low ($\sim 10^{-5} h^{-1}$).
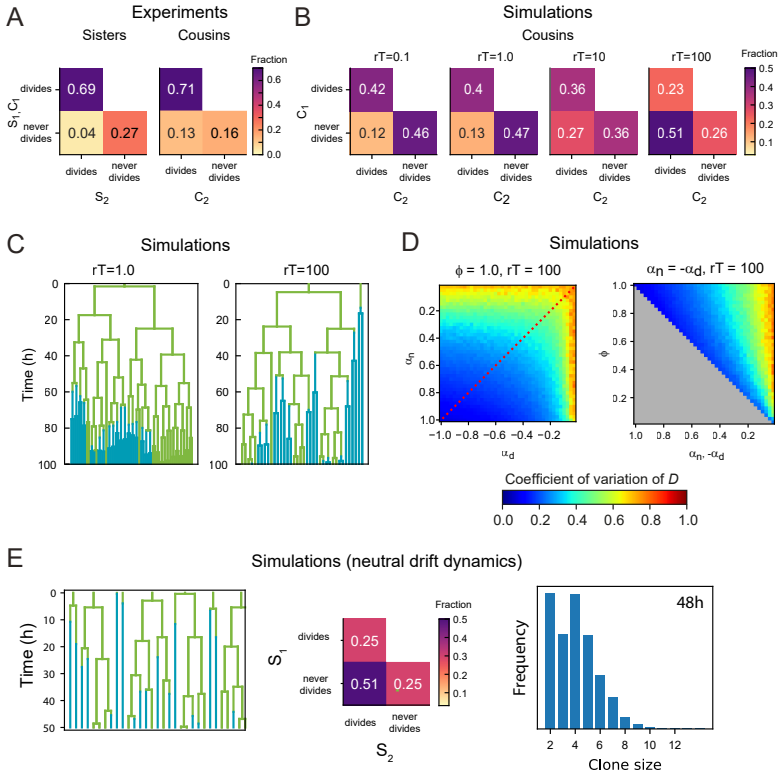
Fig S2.6: Dependence of lineage dynamics on cell rearrangements. (A) Experimentally observed correlations in division patterns between sister (S_1, S_2, n=499) and cousin cells (C_1,C_1, n=560), for cell pairs where neither cell died. (B) Correlations in division pattern between cousin cells (C_1,C_1) for simulations of the two-compartment model, for increasing cell rearrangement rate r. Here, the product $r \cdot T$, where T is the average cell cycle duration, indicates the approximate number of rearrangements experienced per cell cycle. For a 'well-stirred' proliferative compartment, $r \cdot T \gg 1$, asymmetric lineage outcome is more prevalent than symmetric outcome for cousin cells. However, for infrequent cell rearrangements, $r \cdot T \approx 1$, asymmetric lineage outcome for cousin cells is less prevalent than symmetric outcome, with a frequency that resembles that seen experimentally in (A). Data is averaged over 50 independent simulations, with $\alpha_n = -\alpha_d = 0.95$, $\phi = 0.95$, and the average number of proliferating cells $\langle D \rangle = 30$. (C) Example lineage trees obtained from simulations for different $r \cdot T$. Line color indicates whether the cell was in the proliferative (green) or non-proliferative compartment (blue). For $r \cdot T = 1$, closely related cells remain largely together in space, causing ejections from the proliferative compartment to be correlated within lineages. As a consequence, not only sisters, but also cousins and more distantly related cells keep proliferating or cease proliferation together. For $r \cdot T = 100$, this correlation within lineage trees is lost. (D) Coefficient of variation of the total number of proliferating cells D for simulations with a 'well-stirred' proliferative compartment, $r \cdot T = 100$. Left panel shows the effects of varying the growth rates of both compartments when all divisions are symmetric and right panel of varying the degree of symmetry when both compartments have opposite growth rates. Overall, the coefficient of variation shows a similar dependence on parameters as seen for the simulations with infrequent cell rearrangements, $r \cdot T = 1$, shown in Fig. 2.4 in the main text. (E) Simulations of a neutral drift dynamics model for N=30. This model is similar to the 'well-stirred' two-compartment model for the case where all cells are proliferative in the niche compartment ($\alpha_n = 1$, $\phi = 1$), and no cells are proliferative in the differentiation compartment ($\alpha_n = -1$, $\phi = 1$). However, the main difference is that in the neutral drift model, cells switch from proliferative to non-proliferative immediately upon exiting the niche compartment. This results in half of all divisions being asymmetric, as every cell has an independent chance of 50% to exit the niche and thus halt proliferation.

2
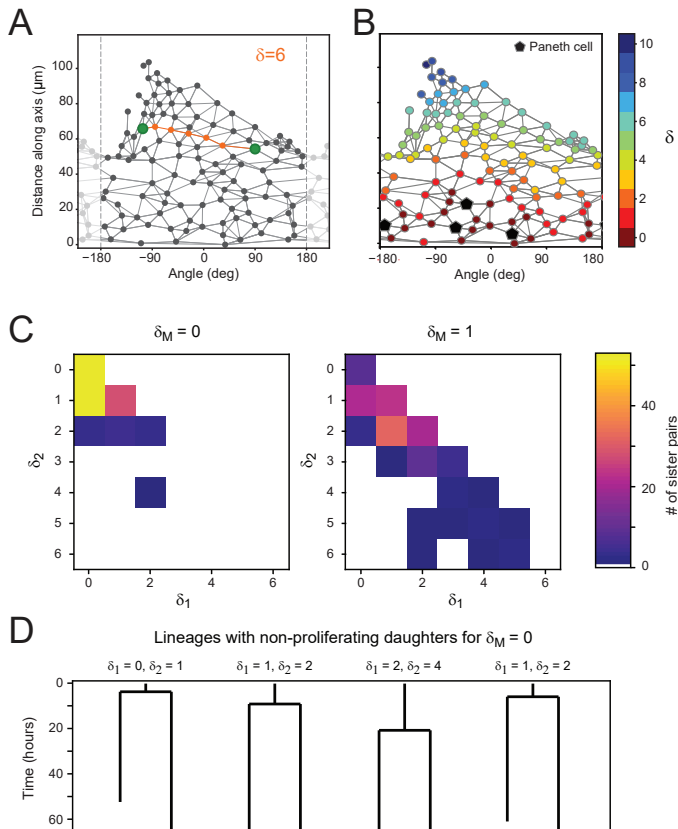
Fig S2.7: Proliferation dynamics as function of Paneth cell distance. (A) After crypt unwrapping and determination of neighbors, the link distance between two cells (green markers) is defined as the number of edges that constitute the shortest path connecting the two cells (indicated in orange, resulting in this case in a neighbor distance of $\delta = 6$). (B) Link distance δ of each cell to its closest Paneth cell, shown for a single time point. (C) Distribution of Paneth cell distances δ_1 and δ_2 of sister pairs generate from a mother cell either directly touching a Paneth cell ($\delta_M = 0$) or one cell removed from a Paneth cell ($\delta_M = 1$). (D) Examples of cell lineages for rare sister pairs that ceased proliferation, even though their mother was touching a Paneth cell ($\delta_M = 0$). For each sister pair, the distances δ_1 and δ_1 after division are given.

3

ORGANOID CELL FATE DYNAMICS IN SPACE AND TIME

X. Zheng, *M.A. Betjes, Y.J. Goos, G. Huelsz-Prince, H. Clevers, J.S. van Zon[#] and S.J. Tans[#]*

Organoids have emerged as an important tool to study tissue renewal. However, as methods to visualize the underlying cellular differentiation dynamics are lacking, key organizational principles remain unresolved. Here, we combine AI-enabled cell tracking with multiplexed endpoint antibody staining to show when and where cells differentiate in intestinal organoids, as well as correlations with their movement and genealogy. Notably, cells that ultimately differentiate and migrate to the villus region committed to their new type already deep inside the crypt – when still surrounded by their relatives that remain stem cells at the crypt bottom. Unexpected consequences of this early commitment are: 1) Secretory cells commit even before terminal division, causing secretory fates to emerge symmetrically in sister cells. 2) The relative abundances of secretory and absorptive cells is controlled mainly by proliferation after commitment. 3) Spatial patterning is achieved after commitment by type-dependent cell movement and rearrangements. This 'commit-then-sort' model contrasts with the idea that cells only commit after moving away from the crypt and into the transit amplifying region, and raises new questions about underlying commitment and sorting mechanisms. It may also be generally relevant, as the tissue architecture and molecular pathways are conserved in diverse stem cell systems. Our approach can be used widely for diverse organoid systems and combined with live-cell imaging.

# denotes co-corresponding authors.

3.1 Introduction

The past decade has brought groundbreaking advances in organoid technology, which enabled many new approaches to studying organ development, self-renewal, and pathology [31, 68, 82, 101, 130]. The benefit of organoids lies in their ability to *in vitro* generate the diverse cell types and 3D organization that characterize *in vivo* organ tissue. Key features of the cellular architecture have been established using immunostaining, fluorescence microscopy, and single-cell RNA sequencing[23, 57, 58, 92, 139]. However, these methods do not reveal the dynamics that is critical to the underlying cellular reorganization and differentiation – as exemplified for instance by the rapidly renewing intestine. Lineage tracing[81, 127, 145, 162] can visualize the offspring of some cells but not when or where cells adopt a new fate, nor their movements or lineage trees. In parallel, important advances have been realized in 3D time-lapse microscopy. Confocal and light-sheet imaging can visualize the dynamics of cell proliferation and migration [96, 119, 139, 160, 181], while machine learning methods can track cells in time [63, 79, 96, 155]. Yet, this approach has been limiting in studying the dynamics of differentiation. While fluorescent protein markers can in principle be used to identify cell types [4, 52, 148], the many involved types (over 5 in intestinal organoids) and nuclear labelling required for tracking presents major challenges in terms of phototoxicity, genetic construction, and wavelength overlap.

Hence, the dynamic basis of cellular organization has not been resolved for any organoid system[14]. In intestinal organoids, stem cells are thought to differentiate when moving into the transit amplifying (TA) region higher up in the crypt, driven by proliferation at the crypt bottom, upon which they stop proliferating and continue upwards to the villus region, where most differentiated cells reside and are ultimately shed into the lumen[15, 25, 28, 165]. Cues are provided by WNT that decreases along the crypt-villus axis and Notch inhibition between secretory and absorptive types that regulates their relative abundance[49, 50, 150]. This 'conveyor belt' model is appealing because it can naturally explain how different types are dynamically organized in space: cells driven towards the differentiated villus region are triggered to differentiate, while cells remaining in the crypt preserve their stem identity. However, with dynamic data lacking, it remains unclear if this principle holds and whether other mechanisms contribute. Addressing these issues require characterization of all cells within key regions.

We therefore developed a method that integrates type identification and tracking (TypeTracker). It works by propagating cell types back in time along lineage trees, using machine learning-based analysis of 3D video microscopy, multiplexed antibody staining of endpoint cells, and a rule-based propagation protocol (Fig. 3.1a). The resulting multi-dimensional data identifies the moment and location where cells differentiate, their movements and genealogical relations to other cells, and the neighbors they interacted with. It can be used for any organoid with proliferating and differentiating cells and requires only confocal microscopy, immunostaining, and data integration software.

Application to mouse intestinal organoids (Fig. 3.1b) revealed an unexpected principle for the interplay between differentiation and spatial organization. Type commitment occurred notably early: well before the differentiating cell lineages ceased to proliferate and moved upward to the villus region – at a moment when the cells still occupied the same region as their stem-cell relatives that continued to retain the stem identify and

remained deep inside the crypt. This early commitment had several notable features. Secretory fate emerged typically with identical types in pairs of sister cells, indicating their mothers had committed already, and contrasting with the notion that committed cells arrest their cell cycle[10, 21, 153]. While cells of different secretory types were observed, they were not closely related and rather emerged from distinct stem cell lineages. This finding challenges the existence of omni-potent secretory precursors that produce progeny of different secretory types[10, 21, 65, 135, 141, 166]. Absorptive lineages committed even longer before cell cycle arrest (over 5 divisions), providing an explaining for the high abundance of absorptive over secretory types. In contrast with current models[15, 18, 30], the stereotypical positioning of cell types was achieved through spatial segregation after commitment, and secretory sister cells separating more rapidly than neighboring cells of different types. Given the conserved nature of the underling pathways such as WNT, this 'commit-then-sort' mechanism may well be widely relevant. Our TypeTracker approach can be used broadly to elucidate the dynamic differentiation programs of organoid systems, how they are affected by mutations or external conditions, and can be integrated with live-cell monitoring of key cell biological processes.

3.2 Results

3.2.1 Overview of TypeTracker

Our method consists of four main steps (Fig. 3.1a). First, movies of organoids growing in Basement Membrane Extract (BME) gel are recorded by 3D confocal microscopy (Fig. S3.1a-c). We focus on intestinal organoids and image complete organoids or their crypt protrusions every 12 minutes for 60 hours, using a H2B-mCherry marker to detect cell nuclei (Fig. S3.1d). Second, we employ a convolutional neural network [79] to track the nuclei in space and time across several generations (Fig. 3.1b, Fig. 3.1e), and visualize their genealogical relations using lineage trees (Fig. 3.1c, Fig. S3.2). Consistently, proliferative lineages, which display up to seven divisions, are mostly found at the crypt bottom, while non-dividing cells are abundant in the villus-like region of the organoid. Third, we perform multiple rounds of antibody staining to determine the cell types at the movie endpoint, as detailed below (Fig. 3.1d, e). Hence, we identify the main types found in the intestine: stem, enteroendocrine, Paneth, goblet, enterocyte, transit-amplifying, as well as an immature mucus producing type. Fourth, we infer the cell types at earlier timepoints, starting at the endpoint of the lineage tree and progressively moving back along each branch to the beginning, using a set of rules that we describe in detail below. Hence, one obtains virtual organoids that present the spatial location, division events, movements, and type of all cells (Fig. 3.1f). The completeness of this method, which identifies all cells in a region of interest and associated lineage trees, enables our backpropagation approach and analysis of spatio-temporal correlations.

3.2.2 Cell type identification

We developed an approach to map cell type data, as obtained by several rounds of antibody staining, onto the endpoint of the movie and lineage trees (Fig. 3.1d, e). This method includes washing protocols that minimize organoid deformations, antibody stripping be-

tween rounds, and a min-cost flow solver algorithm [61] combined with manual correction to link cells in the staining images to the cells at the movie endpoint.
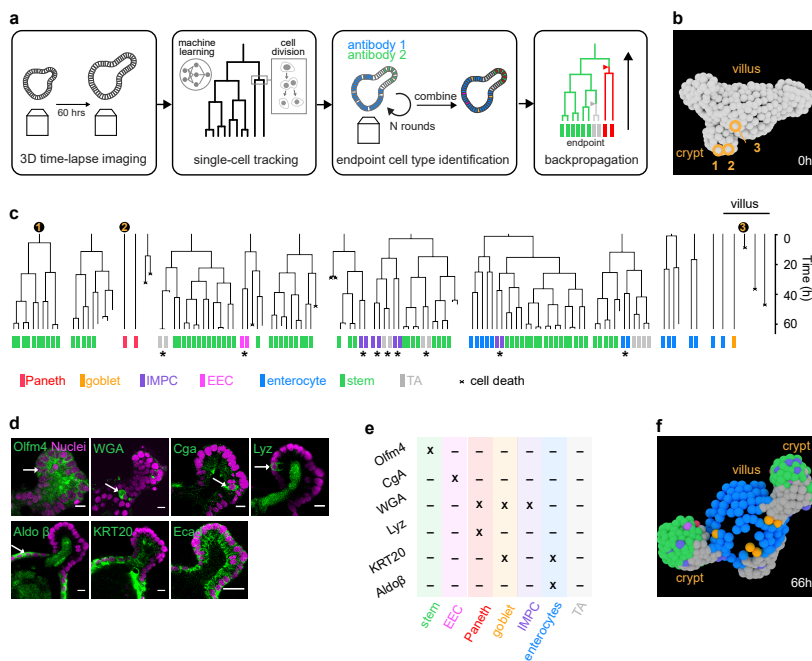
Fig 3.1: TypeTracker method overview and primary data. a, Method workflow. Step 1: Image several organoids in 3D for 60h. Step 2: Track all cells and determine lineage tree using convolutional neural network. Step 3: Identify cell type at movie endpoint using multiple rounds of antibody staining. Step 4: Map cell types onto lineage tree, and infer historical cell types including type transitions (triangles). b, Reconstructed cell positions at start of lineage tree. c, Example lineage trees and their mapped endpoint cell types. Numbers: lineages of three cells seen in panel b. Stars: endpoint sister pairs of same type, but of different type than cousins, suggesting type transition in mother cell. d, Nuclear marker (magenta) and antibody or dye staining (green): Olfactomedin 4 (Olfm4), Wheat Germ Agglutinin (WGA), Chromogranin A(Cga), Lysozyme (Lyz), Aldolase β (Aldoβ), Cytokeratin 20 (Krt20) and Ecadherin (Ecad). e, Cell type identification table. f, Reconstructed cell positions and type at end of the lineage tree (panel c), 66 hours after the start (panel b).

Stem cells were identified by Olfactomedin 4 (Olfm4) [165], enterocytes by Aldolase β (Aldoβ) [139] and enteroendocrine cells (EECs) by Chromogranin A (Cga) [91]. Consistently, Olfm4+ cells were found only at the crypt bottom, Cga+ cells in both the crypt and villus regions and Aldoβ+ cells exclusively in the villus region (Fig. 3.1f). Stem cells and EECs did not stain for any of the other markers used, while enterocytes also stained for Cytokeratin 20 (KRT20) [26], as expected. Wheat Germ Agglutinin (WGA), which stains intestinal mucus [13, 73], labeled cells in the crypt and villus regions. A subset of these were also positive for Lysozyme (Lyz) and thus identified as Paneth cells [129], while another subset expressed KRT20 and identified as goblet cells [26]. Consistently, the former often contained granules that are typical of Paneth cells, while the latter had a cup-shaped morphology

that characterizes goblet cells (Fig. S3.3). A remaining subset of WGA+ cells expressed neither Lyz nor KRT20. Evidence provided below suggests that these are immature Paneth and goblet cells, which we thus refer to as immature mucus producing cells (IMPCs). We identified a population of cells within the crypt that did not stain for any of our markers, which are identified as transit-amplifying (TA) cells based on evidence discussed below.

3.2.3 Sister cells adopt the same type

Prominent in our data is that endpoint types generally came in pairs, with sister cells consistently displaying the same fate (Fig. 3.1c). Statistical analysis showed that 97% of all endpoint sister (N=869 sister pairs in 9 organoids) were of the same type. All types, including secretory types, exhibited this symmetry, as evidenced by the dominant diagonal in the sister-sister cell type histogram (Fig. 3.2a). This consistent type-symmetry between sisters is notable. Intestinal stem cells are proposed to exit from their cell cycle when committing to a secretory fate [10, 21], which would rather yield asymmetry, as one sister may then adopt a secretory fate that the other does not. External cues can, in principle, produce a local environment that is similar for the two sister cells, and hence drive them to the same fate. However, *a priori* there is then no reason why only sisters should be impacted, as also non-sister cells like cousins can be neighbors. Importantly, the fates of many sister pairs were different than their direct cousins (Fig. 3.1c, stars). This showed that the underlying type transitions did affect sisters specifically and occurred during the observed growth period of the lineage. These data indicated that the type transitions rather occurred in the mother (or earlier generations), which subsequently divided to produce two daughters of the same type. Larger subtrees, which for instance showed two or more sister pairs of the same type (Fig. 3.1c, blue enterocyte subtree, Fig. S3.2), were consistent with divisions occurring after type commitment and hence producing cells of the same type.

3.2.4 Dependence of cell age on differentiation state

The age of the cells at the movie endpoint was defined as the time since the last observed division (Fig. 3.2b). Notably, the TA cells showed a statistically identical age distribution as the stem cells, in line with the notion that they are highly proliferative [7, 10, 30]. EECs, enterocytes, Paneth, and goblet cells also showed a broad distribution, but with an average age that was substantially larger than the stem and TA cells, consistent with their terminally differentiated nature. The ages of these terminally differentiated cells were rarely below 20 hours (Fig. 3.2b), suggesting that the involved markers (Cga, Aldoβ, Lyz and KRT20) took a substantial amount of time to become observable.

3.2.5 Cell type backpropagation

To infer the cell type along the lineages of the family tree, we used the lineage tree topology and the above observations (Fig. 3.2a, b). Starting at the lineage endpoints, we propagated the endpoint types back in time using this process: 1) From one timepoint to the previous timepoint, the type is initially assigned as unchanged if branch points (divisions) are not traversed, but may later be updated when a cell type transition is identified. 2) At branch points, the two involved daughters are considered: if both display the same (inferred) type,

the mother is assigned as that type, as discussed above (Fig. 3.2a). 3) If one daughter is a stem cell and the other is not, the mother is assigned as a stem cell, based on the notion that stem cells are generated from stem cells. 4) If one daughter is a TA cell and the other is not, nor a stem cell, the mother is assigned as a TA cell. This rule is based on the TA cells being proliferative like stem cells (Fig. 3.2b), which makes the alternative (the mother has the identity of the non-TA daughter) unlikely. In the last two cases (3 and 4), a type-transition is inferred in one of the daughters. We mark the latter with an arrow halfway the cell cycle (Fig. 3.2c). These rules allowed the backpropagation of complete trees from the end to the beginning (Fig. 3.2d, Fig. S3.4).

Next, we estimated stemness by quantifying the fluorescence intensity of Lgr5-GFP, a well-known stem-cell marker, in order to further test our method. Note that phototoxicity, which is stronger for GFP than for the mCherry that is used for nuclei tracking, limits the frequency and duration of such cell fate quantification during growth. The GFP signal at the movie endpoint was indeed correlated quantitatively with the measured Olfm4 intensity (Fig. S3.5a,b). Cells inferred as stem cells by backpropagation indeed also showed higher GFP expression, while inferred enterocytes or TA and goblet cells consistently showed lower GFP (Fig. S3.5c). Lineages that were inferred to lose stemness and transition to the TA type indeed showed decreasing GFP (Fig. S3.5d). Paneth cell granules, which can be visualized during organoid growth, also showed consistency between inferred and real-time measured type (Fig. 3.2f). Note that limitations of our method are described in the discussion.

3.2.6 Differentiation pathways

The observed differentiation pathways indicated notable features (Fig. 3.2d, Fig. S3.4). Trees typically displayed 1 to 3 cell type transitions, thus yielding sub-trees of the new type, while the old type was maintained in another sub-tree, and some lineages showed two consecutive type transitions. For instance, a stem cell tree was first shown to spawn a TA-subtree, which in turn generated an enterocyte subtree (Fig. 3.2d, tree 1). This order, in which TA is an intermediate type between stem and terminally differentiated types [15], is consistent with the sister-sister cell type histogram: besides the dominant diagonal, low-frequency off-diagonal entries indicated stem-TA sister pairs, and a few pairs of one TA and one terminally differentiated type, but never sister pairs showing two different terminally differentiated types (Fig. 3.2a). The latter would be in line with models where stem cells first differentiate into secretory precursors, which in turn can generate different terminally differentiated types [10, 21, 65, 135, 141, 166]. To further probe this notion, we extracted the largest possible subtrees from our data that contained two types, and found that none had two different secretory types, nor one secretory and one absorptive type. Instead, they typically combined TA and either stem (52.2%) or a terminally differentiated state (31.4%) (Fig. S3.6), consistent with the sister relations (Fig. 3.2a). Among these subtrees, we also found cases (16.4%) that combined stem and terminally differentiated states (Fig. 3.2d, tree 2 and 3), suggesting that these lineages have a negligible TA role.

3.2.7 DIVISION RATHER THAN DIFFERENTIATION RATES CONTROL ENTEROCYTE ABUNDANCE

Cell type transitions to enterocytes were less frequent than to the secretory types combined (about 1.5-fold), even as enterocytes outnumbered secretory cells. To investigate this issue, we quantified the number of consecutive divisions in each differentiation state (Fig. 3.2e). The EEC, goblet and IMPC secretory states mostly showed one division, sometimes two. In contrast with common thinking, we found Paneth cells to divide as well (Fig. 3.2e). The inferred Paneth cell divisions were indeed confirmed by the continuous presence of granules that are specific to Paneth cells and are observable without labeling (Fig. 3.2f). Next, we quantified the cell cycle duration for each cell type. Notably, these complete cell cycles that also showed division at the end were similarly long for all types including secretory and stem types (Fig. 3.2g). The lineages were observed to stop dividing subsequently, consistent with a cell cycle exit.

Enterocyte lineages displayed significantly more divisions than secretory cells. The former reached to up to 5 divisions, not far off from the 6 divisions seen for stem and TA states (Fig. 3.2e). Hence, after specification, absorptive lineages generated substantially more cells than secretory lineages, which thus offset their comparatively low transition rate. This finding is consistent with recent data in which absorptive lineages showed larger clone sizes than secretory lineages [127, 162]. Enterocytes were even found to exhibit the lowest mean cell cycle duration (12.5 h), significantly lower than for both stem (15.5 h) and TA cells (14.1 h) (Fig. 3.2g). Overall, these results indicate that relative abundance is controlled by the cell lineage dynamics, in particular the number of divisions after specification.

3.2.8 THE SPATIO-TEMPORAL DIFFERENTIATION PROGRAM

Access to spatial dynamics is a key benefit of our approach. The positions of inferred cell types mapped along the crypt-villus axis as expected, with stem and Paneth most towards the bottom, followed by IMPC, EEC, TA, enterocyte, and goblet[15, 25] (Fig. 3.3a, b, Fig. S3.7a). In addition, we can now map the point of commitment onto the spatial organoid structure. Commitments to secretory types were broadly distributed along the crypt-villus axis, but typically occurred deeper in the crypt than absorptive commitments (Fig. 3.3c). The latter also distributed broadly and were positioned well within the crypt. Notably, when we mapped full lineage trees along the crypt-villus axis, we found that these committing cells were still in the same approximate spatial region as their close relatives that maintained the stem fate (Fig. 3.3d, e, Fig. S3.7b, c). Spatial separation from these stem-cell relatives did occur after committing (Fig. 3.3d, e). This separation was most evident for lineages destined for the villus region (enterocytes and goblet cells), with the stem lineages they arose from remaining confined to the crypt (Fig. 3.3d, e, top trees). Such separation from relatives was not always observed, specifically for cells committing to a secretory type (IMPC) near the crypt bottom and remaining there (Fig. 3.3d bottom tree, Fig. 3.3e, top tree). Consistently, the mean migration speed is highest for enterocytes and goblet cells, and lowest for secretory fates like Paneth cells and IMPC's (Fig. 3.3f).

3.2.9 Promotion of sister separation

Secretory types were typically born as sisters (Fig. 3.2a) and, hence, as neighbors. We wondered how this finding relates to the observation of single Paneth and goblet cells being surrounded by stem cells and enterocytes, respectively [130, 180]. In our data, most neighbors that were not sisters (and hence can be of different type), were still neighbors after 2h (85%) and 10h (57%), independently of cell type (Fig. 3.3g,h, Fig. S3.7d). Neighbors that were sisters, which almost always were of the same type, separated more frequently after 2h (71% remains neighbors), likely due to arrangements directly following divisions. Surprisingly, Paneth and IMPC sisters showed even stronger separation over longer timescales, and more than the other types, with less than 20% still neighbors after 10h (Fig. 3.3i). Sisters, and in particular of these secretory types, thus appear to rearrange more strongly to achieve interspersion. These findings show that promoted cell separation contributes to cell type patterning in the epithelium.

3.3 Discussion

Before discussing the findings, we begin by reviewing the limitations of our approach. First, cell type transitions may be missed when they are too frequent. Specifically, it cannot deduce the presence of stem or TA cells, or transitions from them, if the tree endpoint only shows differentiated types. This issue can be mitigated partly by limiting the growth duration. Second, if cells would exhibit multiple sequential transitions without dividing, or show reversible transitions back to the stem or TA type, the method would be less suitable. Third, used antibodies may not identify immature types, which impacts marker-based methods more generally. Long type maturation is indeed suggested by our data, including the dominant sister symmetry (Fig. 3.2a), and the high age of differentiated cells at movie endpoint (Fig. 3.2b), noting that rapid type maturation after commitment would yield sister asymmetry in the staining. Moreover, our method provides a key advantage in overcoming this limitation, by detecting early commitment using lineage relations even when the phenotype is not detectably expressed yet.

Our data showed many features that are fully consistent with existing models of intestinal organoid renewal, including the presence of stem cell and TA zones, expected positions of differentiated cell types, and an effective migration along the crypt-villus axis driven by proliferation in the crypt bottom [15, 18, 25] (Fig. 3.3a, d-f). The temporal order of events that dynamic observation uniquely addresses was notable, however. Specifically, we found cells committing to a new type when still positioned in the same area as their stem cell relatives, well before their separation into the cell lineages that move towards the villus region and those that remain in the crypt (Fig. 3.3c-e). We did not observe the opposite: cells that first move away from their stem cell relatives and then differentiate while continuing to move upwards to the villus region, or downward to the crypt bottom. We found commitment even deeper in the crypt for secretory types such as Paneth cells that ended up at the crypt bottom, without showing the proposed downward migration after commitment [12, 15]. Another striking feature of the cellular organization was the rapid separation of neighboring cells, especially secretory sisters (Fig. 3.3h-i), showing how local cell rearrangement can contribute to spatial cell type patterning. Overall, our

data indicated a picture in which cells first commit and subsequently spatially sort and reorganize.

More observations were consistent with this early commitment picture. One example is the highly symmetric adoption of identical fates by sister cells (Fig. 3.2a). Also secretory fates were found to emerge symmetrically in sister cells, indicating that commitment occurred before cell cycle exit and hence the last division. It has been proposed that secretory differentiation occurs through an omni-potent secretory precursor that can generate all types of secretory cells [10, 21, 65, 135, 141, 166]. Our results suggest that this omni-potent secretory state, if it exists, occurs only briefly and is exclusively restricted to the mother cell, because otherwise different secretory fates would be seen among the mother's offspring. This conclusion was further supported by considering more distant relatives: subtrees containing two types at most never contained two different secretory types (Fig. S3.6). These results contrasts with the notion that cells exit their cell cycle directly upon committing to a secretory fate [10, 21, 153], and suggests division may be important to completing differentiation[182]. Reported clonal expansion of goblet cells after fate commitment in mouse colon is consistent with these findings [162]. Our data further showed that the relative abundance of absorptive over secretory cells was controlled more by increased divisions after enterocyte specification (Fig. 3.2e) than by more frequent enterocyte specification events, as for instance controlled by Notch signaling. Notch signaling between neighbors is proposed to restrict secretory fate to a single cell that is surrounded by non-secretory cells. Our observation of neighboring sisters with the same secretory fate (Fig. 3.3h-i) implies that Notch signaling affects cell fate early and transiently, likely in the mothers of secretory cells.

Our method can be applied broadly to study the spatio-temporal differentiation programs of organoid systems, and how they are impacted by external conditions such as metabolic compounds or interleukins, interacting cell types including bacteria and immune cells, and disease mutations. Its focus on spatial and temporal characterization makes it distinct from and complementary to other methods such as single cell RNA sequencing or multiplexed tissue imaging [53, 131]. The TypeTracker approach follows systematically all cells in a region of interest, thus allowing direct correlative analysis, and is straightforward to implement as it requires only confocal microscopy, antibody staining, and the algorithms we present here. It can also readily be combined with other measurements, such as endpoint Single Molecule Fluorescence In Situ Hybridization (smFISH) and real-time fluorescence microscopy of various cellular processes and signals.
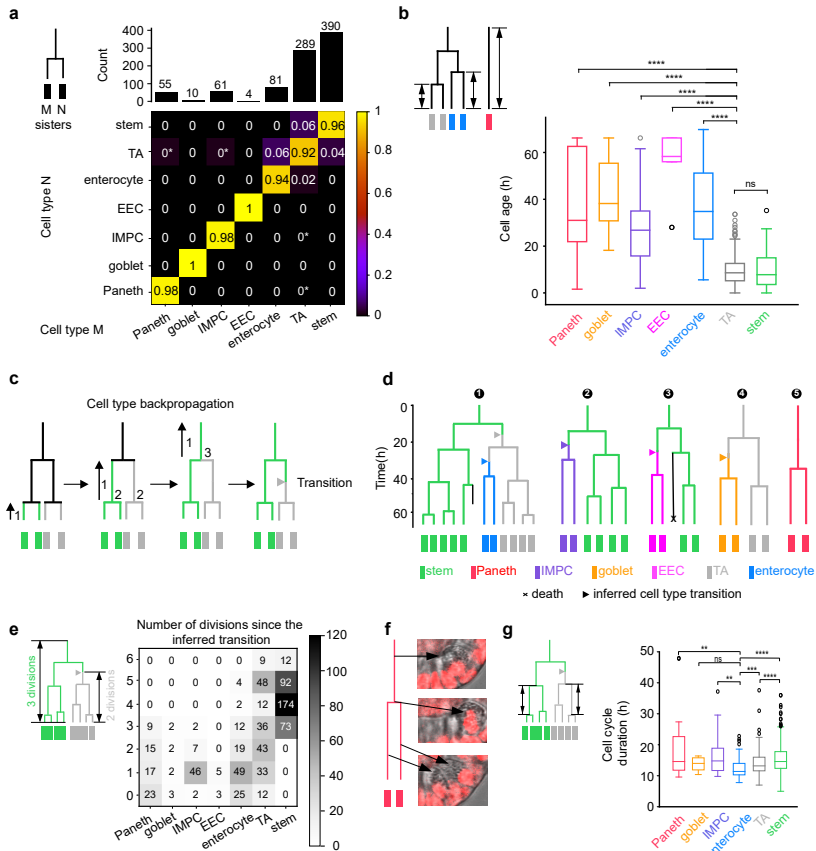
Fig 3.2: Differentiation pathways and cell type commitment. a, 2D histogram indicating the two cell types of sisters at the movie endpoint, as determined using antibody staining. Shown is the number of times a cell type combination was observed divided by the total of each column, indicated on top. Star: low frequency resulting from a single observation. The dominant diagonal shows sisters typically have the same type. b, Age of stained cells, quantified as the time since the last division, or since movie start for lineages without division. $****, p \leq 0.0001; ***, p \leq 0.001; **, p \leq 0.01; *, p \leq 0.05; ns, p > 0.05$. TA cells show the same age as stem cells, indicating their proliferative nature. Consistently, the differentiated cells (EECs, enterocytes, Paneth and goblet cells) are older. c, Cell-type backpropagation rules. 1: working backwards along each lineage, the inferred type is unchanged when not encountering branchpoints (divisions). 2: for branchpoints, if both daughters are the same type, the mother is assigned that type. 3: If only one daughter is a stem cell, the mother is assigned as a stem cell. 4 (not shown): If only one daughter is a TA cell, and the other is not a stem cell, the mother is assigned as a TA cell. In cases 3 and 4, a type-transition is inferred in one daughter (triangle). d, Example lineage trees as determined by TypeTracker. e, Number of observed divisions for each cell type. f, Paneth cell divisions. Granules are seen before and after division, evidencing Paneth cell division. g, Cell cycle duration for different cell types. Cell cycle durations were notably similar between types, while enterocytes exhibited lower mean cell cycle durations than TA cells, stem cells and the secretory cell types. All data in this figure were from nine organoids.

3
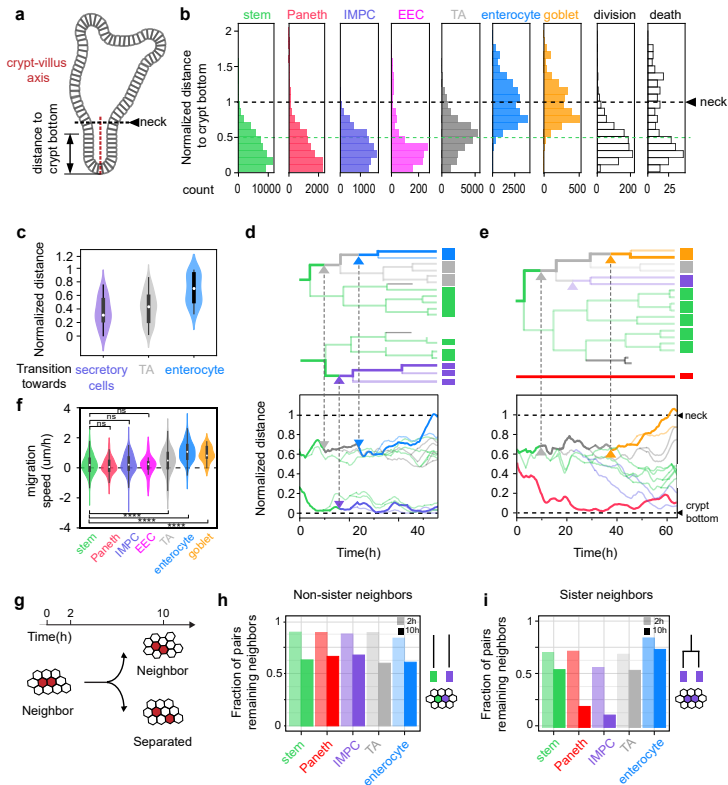
Fig 3.3: Spatio-temporal differentiation program. a, Organoid schematic diagram. b, Inferred cell types mapped along the normalized crypt-villus axis. c, Position of cells when they commit to a new type. d and e, Lineage trees mapped in space along the crypt-villus axis. Bottom trees: Transition to IMPC and position of Paneth cell deep in the crypt surrounded by stem cells. Top trees: Transitions to enterocytes or goblet cells higher in the crypt, but close to their stem cell relatives, followed by their movement to the villus region, rather than the other way around. f, Cell migration speed, as quantified by the migration distance along the crypt-villus axis after commitment or movie start, divided by the migration time. g, Diagram showing that cell separation is quantified as the fraction of neighboring cells that remain so after 2 and 10 h. h, Cell separation of neighbors. This neighbor loss can be quantified for each cell type. Most neighbors remained neighbors even after 10h, independently of cell type. i, Cell separation of sisters. Here the sisters generally are of the same type, due to the fate symmetry of sisters. Sisters thus separate faster than non-sisters, in particular sister Paneth cells and IMPCs.

3.4 Materials and methods

3.4.1 Organoid culture

Murine intestinal organoids carrying both a H2B-mCherry reporter and a Lgr5-GFP reporter were gifts from Norman Sachs and Joep Beumer, from the group of Hans Clevers in Hubrecht Institute. Organoids were embedded in 'domes' of basement membrane extract (BME, Trevingen) in tissue culture plates. They were further submerged in growth medium consisting of murine recombinant epidermal growth factor (EGF 50 ng/ml, Life Technologies), murine recombinant Noggin (100 ng/ml, Peprotech), human recombinant R-spondin 1 (500 ng/ml, Peprotech), n-Acetylcysteine (1 mM, Sigma-Aldrich), N2 supplement (1x, Life Technologies) and B27 supplement (1x, Life Technologies), Glutamax (2 mM, Life Technologies), HEPES (10 mM, Life Technologies), Penicilin/Streptomycin (100 U/ml 100 $\mu g/ml$, Life Technologies) in Advanced DMEM/F-12 (Life Technologies). Organoids were kept in incubators at $37°C$ and 5% CO_2. The medium was changed every two days. Each week, organoids were passaged by mechanically dissociating crypts using a narrowed glass pipette.

3.4.2 Organoid sample preparation for imaging

In conventional culture conditions, organoids were embedded in 'domes' of BME droplets and were thus at different heights relative to the plate bottom (Fig. S3.1a). Imaging organoids located far from the plate bottom required long working distance objectives and increased light exposure, leading to excessive phototoxicity. To improve the imaging procedures, we used the 4 well chambered cover glass (# 1.5 high performance cover glass) from Cellvis as imaging plates. Organoids were broken into single crypts, seeded in the imaging plates and put in fridge ($\sim 4°C$) for $\sim$ 10 minutes, allowing them to sink downwards to the cover glass. Afterwards, they would be incubated at $37°C$ with 5% CO_2 for 20 minutes so that the gel could solidify with organoids settled at the bottom of the wells (Fig. S3.1b). Growth medium was added after the incubation. Organoids were then kept in the incubator for around 2 days until the imaging experiments.

3.4.3 Time-lapse imaging with 3D confocal microscope

Time-lapse imaging was performed with a scanning confocal microscope (Leica TCS SP8) with a 40 x water immersion objective (NA = 1.10). Experiments were performed at $37°C$ with 5% CO_2. More than 20 organoids with already budded crypts were selected for imaging. Stacks of 30 z-slices with 2 μm step size were taken every 12 minutes per organoid. At each timepoint, imaging of H2B-mCherry was conducted with an excitation laser of 552 nm at 1 % of the laser power and the emission signals were collected with Leica HyD hybrid detectors whose filter range was set to be 557 nm - 789 nm.

3.4.4 Live-cell tracking

Live-cell tracking was conducted by OrganoidTracker, a software developed by our group [79]. The positions of each nucleus were predicted with a trained neural network and cells were then automatically linked between frames based on the relative positions and nuclear

sizes. The software could report warnings when the linking was less reliable and allowed for manual corrections.

3.4.5 3D reconstruction

3D reconstruction of organoids were made with Blender, a free and open-source 3D computer graphics software. Each cell was represented by a 3D sphere and could be colored based on the (inferred) cell types (Fig. 3.1b,f).

3.4.6 Organoid fixation and permeabilization

Organoid samples were fixed with 4 % formaldehyde (Sigma-Aldrich) at room temperature. In order to get rid of the gel but keep the organoids attached to the plate, we optimized the fixation protocol. After adding formaldehyde, we waited for ~ 10 minutes and then gentling washed the sample with PBS to remove the gel, which otherwise would hinder the penetration of antibodies and reduce imaging quality. 10 minutes was the optimized waiting time to ensure gel removal and more than 50 % of the imaged organoids attached to the cover glass (Fig. S3.1c). After gel removal, organoid samples were incubated in formaldehyde again for 20 minutes to complete the fixation procedures. Following fixation, permeabilization was performed by incubating the samples in 0.2 % Triton-X-100 (Sigma-Aldrich) for one hour at room temperature. All the washing procedures were performed gently to avoid removing organoids from the cover glass.

3.4.7 Staining with antibodies and dyes

Following fixation and permeabilization, organoids were blocked with 5 % skim milk in TBS at room temperature for one hour. Subsequently, organoids were incubated in blocking buffer containing primary antibody (see section antibodies) for two days at $4°C$, and then incubated with secondary antibody (see section antibodies) at room temperature for one hour. These procedures would be repeated for each antibody. Regarding the dyes, organoids were incubated with Wheat germ agglutinin (WGA) conjugated to CF©488A (5 $\mu g/ml$ Biotium) at room temperature for two hours and with $RedDot^{TM}$1 Far-Red Nuclear stain (1 : 200 Biotium) or $SYTOX^{TM}$1 Orange Nucleic Acid stain (1 : 5000 Thermo Fisher Scientific #S 11368) at room temperature for 20 minutes.

3.4.8 Antibody stripping

After imaging the results from each round of antibody staining, the primary antibodies were removed by incubation with elution buffer at room temperature for 15 minutes while shaking[139]. This was repeated six times with the elution buffer replaced between consecutive cycles. The elution buffer was prepared by adding 0.5 M Glycine (Sigma-Aldrich), 5 M Urea (Sigma-Aldrich), 5 M Guanidinium chloride (Sigma-Aldrich), 70 mM TCEP-HCL (Sigma-Aldrich) to H_2O, with pH adjusted to 2.5.

3.4.9 Antibodies and dyes

Primary antibodies	Dilution	Product information
Rabbit anti-lysozyme [EC 3.2.1.17]	1:800	Dako #A0099
Rabbit anti-Olfm4 [D6Y5A] XP	1:500	Cell signaling technology #39141
Recombinant rabbit anti-Aldolase β + Aldolase C [EPR3138Y]	1:300	Abcam #ab75751
Mouse anti-Human Cytokeratin 20 [Clone Ks20.8]	1:500	Dako #M701929-2
Mouse anti-Chr-A [C-12]	1:50	Santa Cruz Biotechnology #sc-393941
Rat anti-E-cadherin [DECMA-1]	1:400	Santa Cruz Biotechnology #sc-59778

Dyes	Dilution	Product information
WGA conjugated to CF©488A	$5\mu g/ml$	Biotium
$RedDot^{TM}$1 Far-Red Nuclear stain	1:200	Biotium
$SYTOX^{TM}$ Orange Nucleic Acid Stain	1:5000	Thermo Fisher Scientific #S11368

Secondary antibodies	Dilution	Product information
Goat anti-rabbit IgG *H&L* (Alexa Fluor©405) pre-adsorbed	1:1000	Abcam #ab175654
Goat anti-Rat IgG *H&L* (Alexa Fluor©555) pre-adsorbed	1:1000	Abcam #ab150166
Donkey anti-Mouse IgG *H&L* (Alexa Fluor©647)	1:500	Thermo Fisher #A31571
Donkey anti-Rabbit IgG *H&L* (Alexa Fluor©405)	1:1000	Abcam #ab175649

The order of staining, optimized to ensure good staining quality for all cell types, was based on the staining quality and stripping difficulty of each antibody (Fig. S3.1f).

3.4.10 Cell type identification

Olfactomedin 4 (Olfm4) and Chromogranin A (Cga) stained stem and enteroendocrine cells (EECs) respectively[91, 165]. Paneth and goblet cells were both stained by Wheat Germ Agglutinin (WGA), which stains mucus[13], and could be distinguished by affinity for Lysozyme (Lyz) and Cytokeratin 20 (KRT20) respectively. We also found cells labelled solely by WGA, which may be early Paneth or goblet cells, and were referred to as immature mucus producing cells (IMPCs). Enterocytes were stained by Aldolase β (Aldoβ) as well as KRT20 [26, 139]. A number of cells were negative for all the used markers and were referred as transit-amplifying (TA) cells.

3.4.11 MAPPING ENDPOINT CELL TYPES TO LINEAGES

During time-lapse imaging, the Leica software allowed recording of the imaged locations, which could thus be found back after imaging. To achieve this, the mounting stage of the microscope and the orientation of the cover glass should be consistent with the settings during time-lapse imaging. With our optimized protocols for sample preparation and fixation (see Section Organoid fixation, permeabilization and staining), we could keep more than 50 % of the imaged organoids with limited deformations in the plate after fixation. After staining and relocating the organoids that were imaged in time during growth, mapping all cells (including their type information) to the cells that were tracked could be still challenging, due to the constant movement of cells during growth and global rotation and deformation of organoids caused by the fixation and repeated staining and washing. To mitigate these issues, we fixed the organoids within 5 minutes after the time-lapse imaging and performed every washing step gently, in order to preserve the spatial context of single cells. The linking of cells before and after fixation could be achieved mostly based on the spatial context of each cell. Linking was done in two steps. In a first automated step, we used a min-cost flow solver algorithm, which integrally optimizes the linking for all the tracked cells, and was also employed for the similar task of tracking cells between frames during organoid growth. In a second step, we manually corrected the automated linking results by visual inspection of the movie and staining images. The fluorescence intensity of H2B-mCherry showed heterogeneity between cells during time-lapse imaging, which could be preserved during fixation. Therefore, the brightness of the nuclear marker could also assist cell linking before and after fixation.

3.4.12 ENDPOINT SISTER TYPE ANALYSIS

We studied the correlation of endpoint cell fates between sisters. For cells present at the endpoint, identified as specific type and with a sister, we checked the possible cell types of the sister pairs and counted the occurrence of each combination. For each cell type, we counted the number of sister pairs where at least one of them was of that type. If both sisters were of that type, the pair would be counted twice. Cells of different types had different abundance and majority of the sister pairs contained stem cells and/or TA cells. We then normalized the 2D histogram, via dividing the occurrence of each combination by the sum of each column, as shown in the bar plot in Fig. 2a. Therefore, the frequency within each column in Fig. 3.2a would sum up to be 1. The analysis was based on nine different organoids.

3.4.13 CELL AGE DISTRIBUTION ANALYSIS

For cells present at the endpoint, we could check the history of them and find the time when they were born. The duration between the birth time and the endpoint of imaging was measured as the cell age. Some cells were present from the beginning till the end. Their ages were then measured by the total length of the imaging experiment duration (~ 60 hours). The age distribution of each cell type was studied and plotted as a box plot in Fig. 3.2b, followed by statistical significance tests. Box plot elements represent the following: center line: median; box, quartiles; whiskers, range; fliers, outliers. The analysis was based on seven different organoids from experiments lasting ~ 60 hours.

3.4.14 Analysis within (sub-)trees containing two cell types

All of the (sub-) lineage trees with two different cell types were taken into account, unless more than 50 % of the cells within the lineage could not be tracked or died. The absolute count of each possible combination of the two cell types was shown in the 2D histogram (Fig. S3.6).

3.4.15 Cell type backpropagation

The assumption underlying the backpropagation of cell types is that changes in cell types are rare. This assumption could be supported by the found type symmetry between sisters since frequent type changes likely lead to different types in sisters. Starting at the lineage endpoints, we propagate the measured endpoint types back in time following this process:

Backpropagation along consecutive timepoints. From one timepoint to a previous timepoint, the type is initially assigned as unchanged if no tree branch points (divisions) is traversed (marked '1' in Fig. 3.2c).

Backpropagation of symmetric fate. For cell types identified by endpoint staining, we observed that sisters almost always assumed the same fate (Fig. 3.2a), suggesting that this fate was already set in the mother cell. Generalizing this observation, we assumed that if both sisters have the same (inferred) cell type, the inferred cell type of the mother cell is the same (marked '2' in Fig. 3.2c). Regarding cells with a dead sister, the mother is inferred the same type as the living daughter.

Backpropagation of asymmetric fate. The above backpropagation rule does not apply if two daughters have different (inferred) cell types. Therefore, we introduced two addition backpropagation rules. First, if at least one daughter's (inferred) cell type was stem cell, then the inferred cell type of the mother was also stem cell (marked '3' in Fig. 3.2c). Second, if the (inferred) cell type of one daughter was TA and the other daughter was not stem cell, then the inferred cell type of the mother was TA (not shown in Fig. 3.2c). These two rules were based on the capability of stem cells to generate all cell types and the transient property of TA cells between stem cells and differentiated cells.

Forward propagation of cell type changes. If a mother and a daughter cell had different (inferred) cell types, we interpreted this as a change in cell type that occurred during the lifetime of the daughter cell (marked with triangle in Fig. 3.2c,d).

These simple rules were sufficient to propagate backwards the lineage trees that we have encountered, unless the tree appeared very 'broken' where majority of the cells could not be tracked or died. All the lineage trees after backpropagation were shown in Fig. S3.4.

3.4.16 Imaging and quantification of a Lgr5 reporter

To test our backpropagation method, we performed time-lapse imaging, endpoint staining and live-cell tracking in an organoid line with both Lgr5-GFP, a well-known stem cell marker, and a H2B-mCherry reporter. To limit phototoxicity caused by GFP imaging, we

sampled the GFP channel about every 8 hours. The time-lapse imaging lasted for more than 24 hours, followed by endpoint staining.

Quantification of the membrane bound Lgr5-GFP fluorescence signals was conducted by determining the average fluorescence intensity within a 2D sphere with a diameter of 12 μm, which was sufficiently large to include one cell (Fig. S3.5a). The Olfm4 staining was on the membrane as well and measured with the same method. The Lgr5 signal at the endpoint was plotted against the measured Olfm4 intensity (Fig. S3.5b).

We quantified the fluorescence intensity of Lgr5-GFP in time. There were only few frames where Lgr5-GFP was imaged, therefore, most cells were only present in one or two of such frames. For cells only present in one frame, the measured GFP fluorescence within that frame would represent their Lgr5 signals. For cells present in multiple frames, their Lgr5 signals were obtained by averaging the GFP fluorescence between different frames. Quantification of Lgr5-GFP signals was performed for different (inferred) cell types (Fig. S3.5c). For lineages inferred to lose stemness and transition to the TA type, we plotted the Lgr5 signals in time during the lineage progression (Fig. S3.5d).

3.4.17 Measuring locations of cells along the crypt-villus axis

At each timepoint, the crypt-villus axis was manually annotated in the xy plane at the z position corresponding to the center of the crypt, since tracked crypts grew perpendicularly to the objective. Three to six points were marked along the axis, through which a spline curve was interpolated as the axis. For each tracked cell i we determined its position along the spline by finding the value of r_i that minimized the distance d between the cell position and the axis (Fig. S3.7a). The bottom-most cell of the crypt, i.e. that with the lowest value of r_i, was defined as position zero. Based on the shape and curvature of the epithelium, the location of crypt neck (where there was a sharp transition from crypt to villus) was estimated and annotated manually, as an indication of the length of the crypt. Since different crypts were of various length, we did a normalization of the locations based on the crypt neck location. For each cell's measured distance in μm within a certain frame, we divided it by the distance from the crypt neck within the same frame to the crypt bottom. Therefore, the length from crypt neck to bottom would remain one for each timepoint and each crypt. With this measurement, both the locations of different (inferred) cell types and the type transitions were mapped along the crypt-villus axis (Fig. 3.3a-e).

3.4.18 Measurement of migration speed along the axis

To estimate how fast a cell migrated along the axis, we searched for the locations of cells along the crypt-villus axis when they firstly showed up during tracking and the locations of cells when they were last present. The migration speed could be estimated by dividing the distance that the cell had migrated by the duration during which the cell was present (Fig. 3.3f).
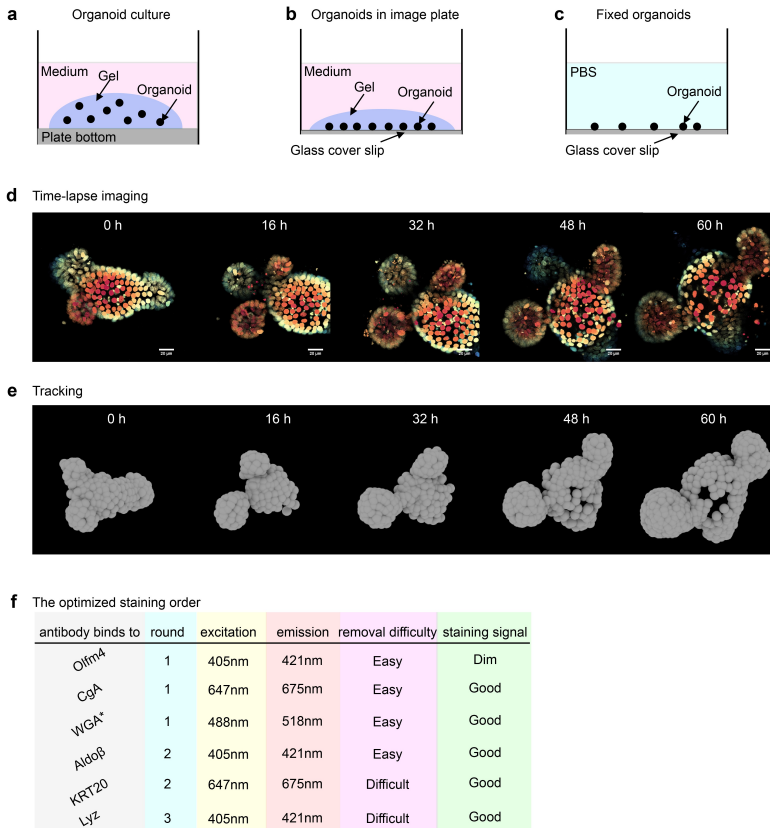
3.4.19 SEARCH FOR NEIGHBORS FOR EACH CELL

Defining neighboring cells in organoids based on nuclear signal is non-trivial. Cells could have varying numbers of neighbors because of the disorder in the epithelium. Distances between nuclei could vary between cell types and location (spread apart in the villus-like region and closely packed in the crypts). To obtain robust neighbor pairs, we functionally defined neighbors as pairs of nuclei without another nucleus in between (Fig. 3.7d). This condition was tested by a 'neighbor score', the ratio of the sum of the distances of the two cells of interest (*A&B*) to a third cell (*S*) and the distance between the two cells (*A&B*), namely $\frac{d_{AS}+d_{BS}}{d_{AB}}$. If the third cell *S* positioned perfectly in between the pair of interest *A&B*, the neighbor score would appear as the minimal value of 1 and *A* and *B* would not be identified as neighbors. If *A* and *B* were not separated by *S*, the three nuclei would form a triangle with high neighbor score between *A* and *B*. For each cell, we calculated the neighbor score for the twenty closest neighbors (in Euclidean distance) at every timepoint. If the neighbor score were higher than $\sqrt{2}$, we would consider them neighbors. This cut-off corresponded to diagonal neighbors in the case of a perfect square lattice. Using this cut-off, we found most cells with five or six neighbors, exactly as expected for the basal side of a curved epithelium8.

3.4.20 MEASUREMENT OF SEPARATION RATE

Separation rates were determined by following pairs of neighbors over time. For a new born cell, its neighbors were searched and selected with the method introduced above. The selection was conducted one hour after division, so that the nuclei would have returned to the basal side of the epithelium. If the selected neighbors divided, we would continue tracking one of the daughters (selected randomly) so that the following of the neighbor pairs would not be cut short by division. The separation rates were measured after following the neighbor pairs for 2 hours and 10 hours, by calculating the fraction the pairs staying as direct neighbors within the total of pairs that were followed. Regarding the rearrangement rates of sisters, we followed the sister pairs that shared the same (inferred) cell type. Separation rates of sister pairs were also measured after 2 hours and 10 hours, by calculating the fraction of sisters staying as direct neighbors within the total number of sister pairs being followed (Fig. 3.3h,i).

3.5 Supplementary figures

a Organoid culture

b Organoids in image plate

c Fixed organoids

d Time-lapse imaging

0 h   16 h   32 h   48 h   60 h

e Tracking

0 h   16 h   32 h   48 h   60 h

f The optimized staining order

antibody binds to	round	excitation	emission	removal difficulty	staining signal
Olfm4	1	405nm	421nm	Easy	Dim
CgA	1	647nm	675nm	Easy	Good
WGA*	1	488nm	518nm	Easy	Good
Aldoβ	2	405nm	421nm	Easy	Good
KRT20	2	647nm	675nm	Difficult	Good
LYZ	3	405nm	421nm	Difficult	Good

Fig S3.1: TypeTracker applied to mouse intestinal organoids. a, For conventional organoid culture, organoids were scattered in 'domes' of BME gel and located at various heights. b, For time-lapse imaging, organoids were seeded in a thin layer of BME gel in chambered cover glass slides. Immediate after seeding, samples were put in fridges for 10 minutes so that organoids all sank towards the cover glass. c, With our optimized protocol, more than 50 % of the imaged organoids would remain at their imaged locations after fixation. d, Time-lapse imaging of an organoid carrying the H2B-mCherry reporter with 3D confocal for 60 hours. Scale bar, 20 μm. Color encodes different z planes. e, Live-cell tracking of the organoid. In these 3D reconstructions, each cell was represented by a sphere centered at the estimated nuclear center. Cells were not tracked if they were located far away from the objective and would move away from the region of interest. e, The order of antibodies and dyes to use in different rounds was optimized based on the staining quality and stripping difficulty of each antibody.
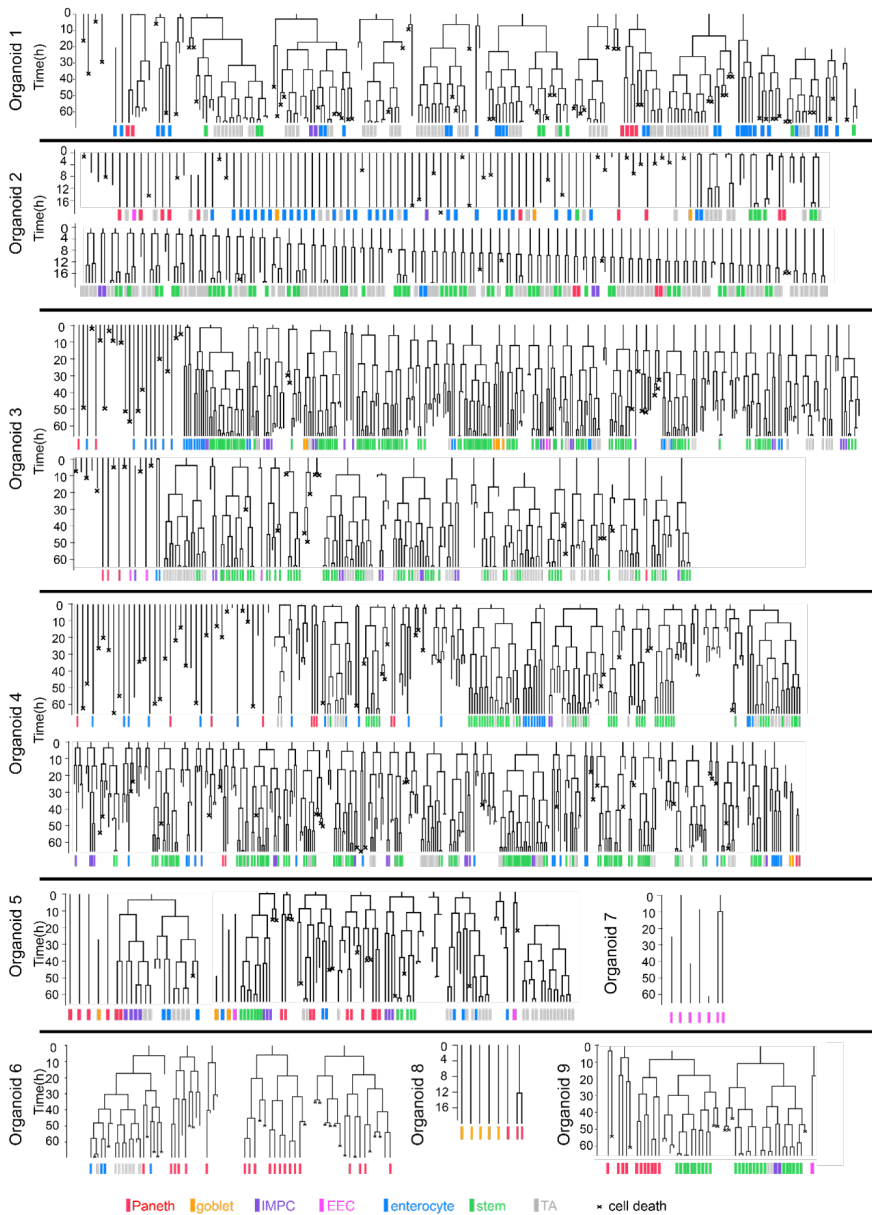
Fig S3.2: Gallery of lineage trees, generated from live-cell tracking, with cell types mapped at the endpoint. These trees are from nine different organoids.
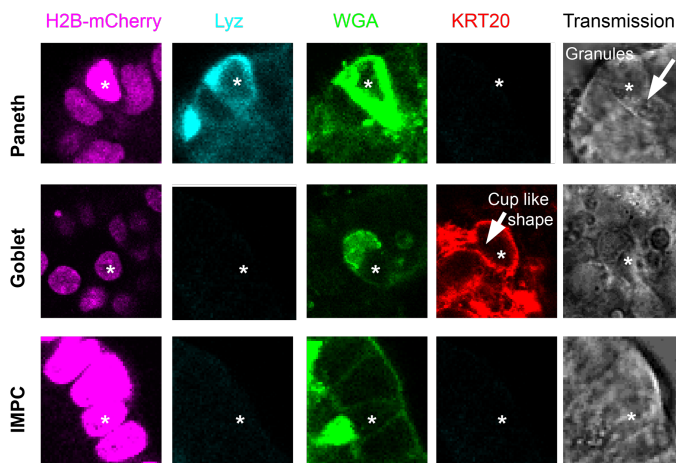
Fig S3.3: The identification of mature Paneth cells and goblet cells. Paneth cells (indicated with * in row 1) often showed extremely bright H2B-mCherry fluorescence signals compared with the neighbor cells, bright Lysozyme (Lyz) fluorescence signals at the basal side of the cell, bright Wheat Germ Agglutinin (WGA) staining and granules in the transmission channel. Goblet cells (indicated with * in row 2) often stained positive of Cytokeratin 20 (KRT20) and WGA, with a cup like shape. A group of cells that stained positive of WGA but negative of KRT20 or Lyz were called Immature Mucus producing cells (IMPCs, indicated with * in row 3). These cells could be early Paneth cells or goblet cells considering the mucus secretion functions that they had.

3
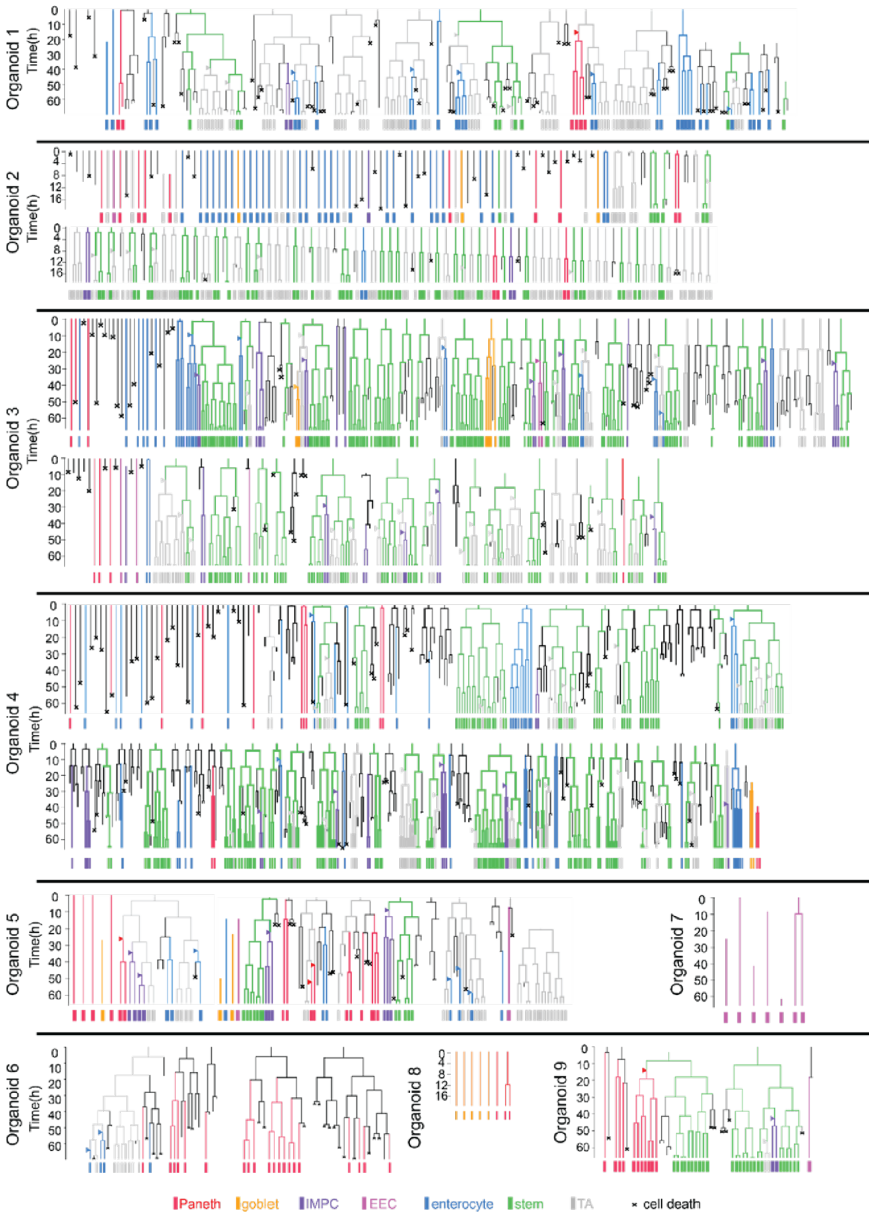
Fig S3.4: Gallery of lineage trees after backpropagation with inferred cell type transitions. Inferred cell types are shown with different colors. Type transitions are indicated by triangles, colored based on which type the cell was inferred to transition towards. These trees are from nine different organoids.

3
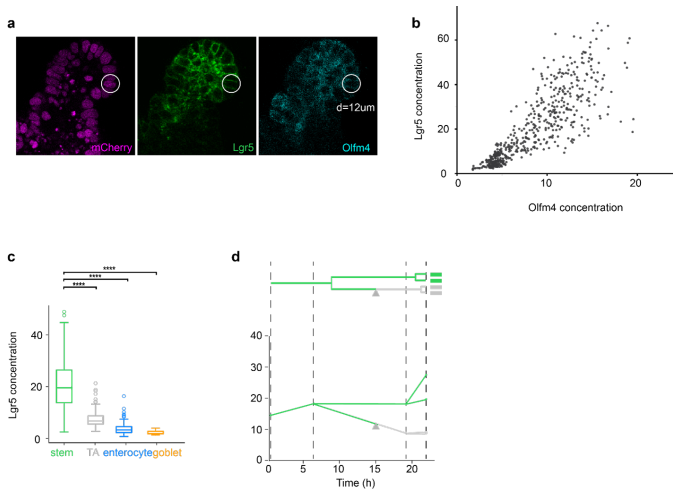
Fig S3.5: Imaging and tracking with a Lgr5 reporter confirmed the backpropagation method. a, Images of the nuclei (H2B-mCherry), Lgr5-GFP (fluorescent reporter of stem cells) and Olfm4 (antibody used to identify stem cells). A 2D circle (d = 12 μm) was used to measure the fluorescence concentration of each cell. b, The Lgr5 and Olfm4 fluorescence concentration, measured by averaging the fluorescence intensity within 2D circles as shown in a, were proportional in single cells. c, The Lgr5 fluorescence concentration plotted against different (inferred) cell types, with stem cells showing high Lgr5 concentration, TA cells showing lower concentration and enterocytes and goblet cells having almost no Lgr5 fluorescence signals. d, Lgr5 fluorescence concentration measured in lineages going through transitions from stem cells to TA cells. The concentration measured 4 hours after the inferred transition was much lower than the concentration measured 8 hours before the transition.
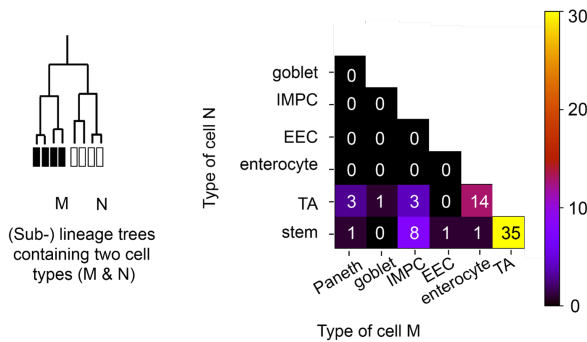
Fig S3.6: (Sub-) lineage trees containing two cell types often had at least one of the types as either stem cells or TA cells. All of the (sub-) lineage trees with two different cell types were taken into account, unless more than 50 % of the cells within the lineage could not be tracked or died. The occurrence of each possible combination of the two cell types was counted and shown in the 2D histogram. Combination of two different differentiated cell types, such as enterocytes and goblet cells, was never found. Differentiated cells were often found together with either stem cells or TA cells in the same lineage.

3
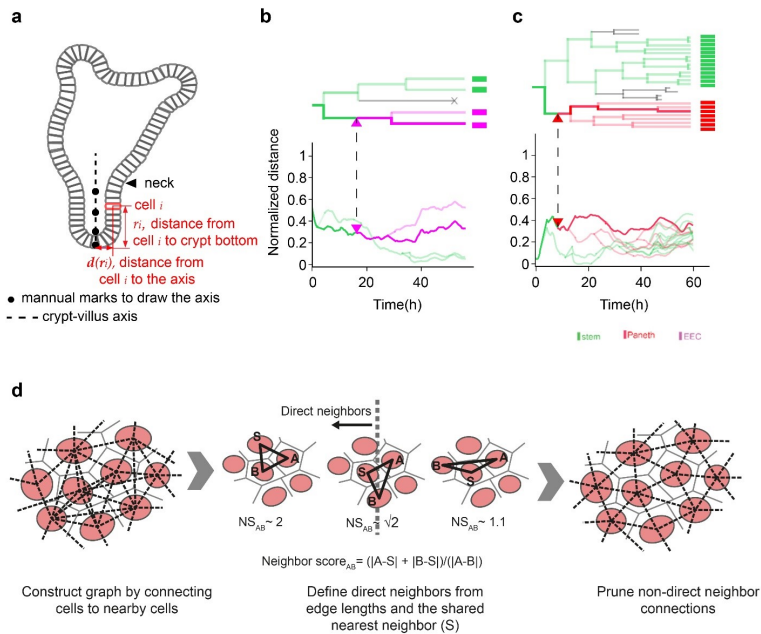
Fig S3.7: Following the spatial organization of cells during differentiation. a, The crypt-villus axis could be generated by interpolating through the manually annotated points. For each tracked cell i, we determined its position along the axis by finding the value of r_i that minimized the distance $d(r_i)$ between the cell position and the axis. b and c, The moving trajectories of cells within different lineages were colored by inferred cell types. Transitions to EECs and Paneth cells took place deep in the crypt, around 0.4, surrounded by stem cells which were often found from 0 to 0.6 along the axis. d, Neighbors were defined as pairs of nuclei without another nucleus in between. For each cell, the neighbor score for the twenty closest cells (in Euclidean distance) was calculated at every timepoint. If the neighbor score were higher than $\sqrt{2}$, cells would be identified as neighbors.

4

Loss of Paneth cell contact starts a differentiation timer

R.N.U. Kok, **X. Zheng***, T. Clement, K. Spoelstra, J.S. van Zon#, S.J. Tans#*

Wnt signaling is essential for development and tissue maintenance. In the small intestine, Paneth cells at the crypt bottom secrete Wnt, which maintains the proliferation and stemness of the neighboring stem cells. There are two competing models for Wnt signaling regulation after stem cells lose contact with Paneth cells. 1. Cells experience a decreasing Wnt gradient as their distances to Paneth cells increase. 2. Wnt signaling levels are only altered with each cell division by dilution of the amount of Wnt bound per cell. Here, we show that cells rapidly reduce their Wnt signaling levels once their contact with Paneth cells is lost, even in the absence of cell growth and division. If Paneth cell contact is not regained in time, cells differentiate even if the distance towards the nearest Paneth cell is short. These findings contradict the current models and suggest a new model of Wnt signaling dynamics: a timer model. In this model, the loss of contact with a Paneth cell triggers a timer for stem cell differentiation. Such a timer starts much earlier than the occurrence of cell divisions or cell migration further away from the crypt bottom.

---

* denotes co-first authors, # denotes co-corresponding authors.

4.1 Introduction

Wnt signaling plays an essential role in embryonic development, adult tissue maintenance and cancer [11, 118, 176]. In the adult small intestine, canonical Wnt signaling is required for stem cell maintenance, and overstimulating Wnt causes hyperproliferation of the epithelium [15, 46, 56, 139]. The size of the stem cell zone in the intestine is known to be regulated by the Wnt gradient along the crypt-villus axis, with maximum expression in the stem cell region at the crypt base and gradually decreasing along the crypt domain [45, 56, 150]. Therefore, a spatial model has often assumed that once a stem cell has moved a particular distance away from the source of Wnt ligands, it will start to differentiate. Such a model is appealing, as it provides an intuitive explanation for cellular differentiation. However, the time dynamics of the maintenance of the Wnt gradient and the regulation of cell differentiation have not been tested.

There are several indications of the insufficiency of such a simple spatial model. First, Farin et al. [45] showed that Wnt signaling only affects direct neighbor cells, thereby preventing any long-range signaling. The authors looked at mouse small intestinal organoids, where Paneth cells are the only source of Wnt [40, 74, 129, 168]. After the loss of contact with Paneth cells, Wnt dilutes after every cell division [45]. However, the authors did not track Wnt signaling over time and left open the question of how differentiation is controlled in time. Second, the spatial gradient of Wnt does not explain the origins of Paneth cells. Paneth cells are the only differentiated cell type commonly found next to stem cells at the bottom of the crypt. As a spatial model requires cell differentiation to take place outside the stem cell region, it was assumed that all Paneth cells were born higher in the crypt and then moved back into the stem cell region [52]. However, it has been reported that such a detour is not required for differentiation by Böttcher et al. [20]. In their work, the authors have shown that Paneth cells and enteroendocrine cells originate directly from stem cells low in the crypt. It is unclear how this observation fits into the spatial model of differentiation.

Here, we directly look at Wnt dynamics over time. We used intestinal organoids generated from a recently developed mouse model with an Axin2 reporter [164], which is an important and widely expressed Wnt target gene [93]. We combined live cell tracking of these organoids with endpoint antibody staining for the most common intestinal cell types. We used the resulting time-lapse movies to observe when cells lose and gain contact with other cells, when the Axin2 expression of the cells is changed, and which cell type the cells assume. In addition, we tested for causality by laser ablating individual Paneth cells and showed that once contact with Paneth cells is lost, cells rapidly decrease their Wnt target gene production, even before a division occurs. Our findings indicate that Wnt signaling is more likely to follow a timer model, where the amount of Wnt on the cell surface decreases rapidly after contact with Paneth cells is lost. Once the Wnt signaling level becomes low enough, cells would differentiate. This model provides a robust mechanism for differentiation: small lapses in Paneth contact will not cause accidental differentiation, but longer losses of contact will make stem cells differentiate, even if they do not move any further away from the Paneth cells.

4.2 Results

4.2.1 Characterizing Wnt signaling in time and space

We imaged Wnt dynamics using overnight time-lapse movies of mouse small intestinal organoids with confocal microscopy. The organoids were obtained from the intestine of an $Axin2^{P2A-rtTA3-T2A-3xNLS-SGFP2}$; $tetO-Cre$; $Rosa26^{mTmG}$ triple-heterozygous mouse [164]. Axin2 functions as an accurate reporter for cells that receive a Wnt signal, as it is one of the most widely expressed target genes of the canonical Wnt pathway. The Axin2 reporter, which shows nucleus-localized fluorescent signals (Fig. 4.1a), has been demonstrated to accurately respond to both Wnt inhibition and hyperactivation [164].
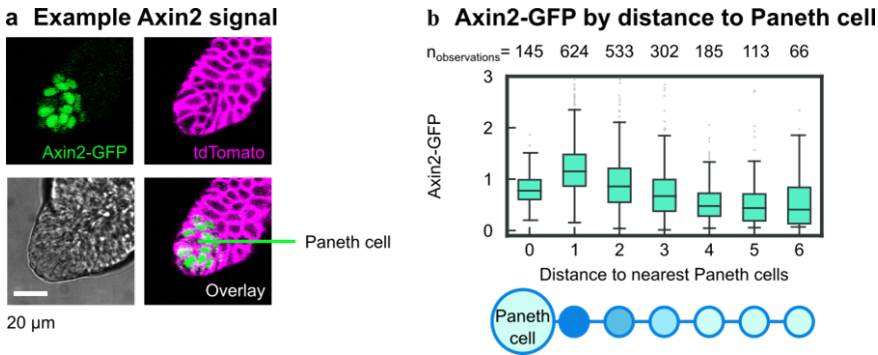
Fig 4.1: The relation between a cell's Axin2 signal and its distance to Paneth cells. a. A crypt of a mouse small intestinal organoid, showing Axin2-GFP signal and membrane-targeted tdTomato. b. Axin2-GFP signal as a function of the distance to the nearest Paneth cell.

We followed the Axin2-GFP expression of over 140 cells among three organoids. We tracked all cells manually by annotating the nucleus center of each cell. We then measured the total amount of GFP signal in each cell (Materials and Methods). Since Paneth cells are the only source of Wnt in these organoids, the Wnt signaling levels and Wnt target gene expressions should decrease as the distance to Paneth cells increases [45]. As expected, we found cells further away from Paneth cells showing lower Axin2-GFP signals (Fig. 4.1b). This spatial gradient can be explained using multiple models of Wnt signaling with different time dynamics. One model that can establish the spatial gradient is a spatial Wnt diffusion model, where the concentration of Wnt proteins decreases gradually as the distance to the nearest Paneth cell increases. Another model is the model of Farin et al. [45], which we refer to as the division dilution model. In this model, Wnt signaling levels are only altered with each cell division by dilution of the amount of Wnt bound per cell. The observed spatial gradient is therefore a result of a correlation: cells further away from Paneth cells would have divided more times and have fewer Wnt proteins on their surface.

4.2.2 The Axin2-gfp signals decrease when a cell loses contact with Paneth cells

We tracked Axin2-GFP levels in cells that were first in sustained (> 1 hour) contact with Paneth cells, but later remained out of contact for a prolonged amount of time (> 2 hours) (Fig. 4.2a). While the cells were still in contact with Paneth cells, their Axin2-GFP level was increasing. After losing contact with Paneth cells, the Axin2-GFP level in the vast majority of cells began to decline (Fig. 4.2b, Fig. S4.1).
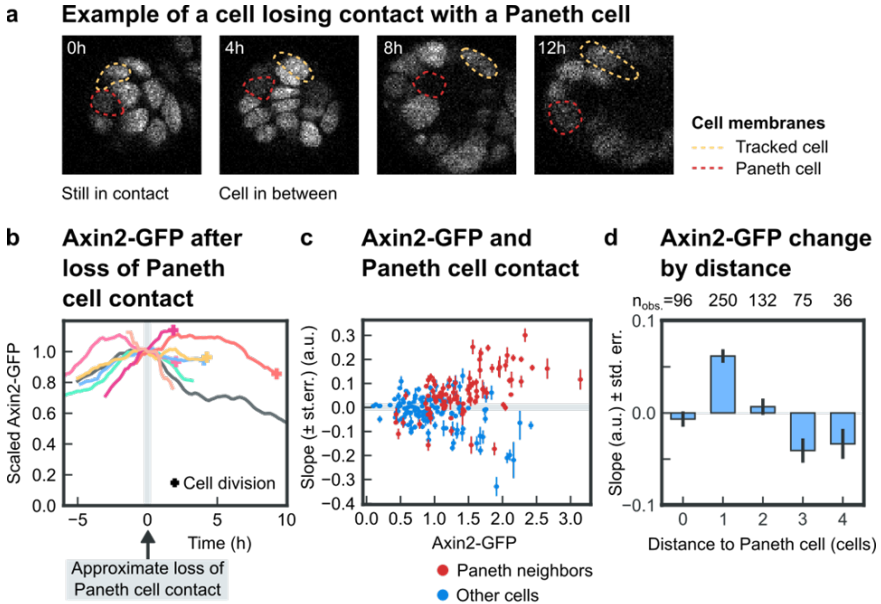
Fig 4.2: Axin2-GFP level decreases significantly after losing contact with Paneth cells. a. A cell (marked in red) that lost contact with a Paneth cell (marked in orange) during the time-lapse imaging. b. Axin2-GFP levels of cells, similar to the example in a, that was initially in contact with Paneth cells, but later, lost contact for at least two hours. Crosses mean cell divisions. c. The slope of Axin2-GFP dynamics, showing how Axin2-GFP changed over time, plotted against the Axin2-GFP levels. d. The slope of Axin2-GFP dynamics plotted against the distance to the closest Paneth cell.

To check whether these increases and decreases of Axin2-GFP (Fig. 4.2b) are common features in our dataset, we looked at shorter cell tracks, where cells did not divide or change their contact with Paneth cells during the imaging and tracking. Cells in contact with a Paneth cell (red dots) often had higher Axin2-GFP levels than cells not in contact (blue dots), and their Axin2-GFP levels tended to increase over time (Fig. 4.2c, Fig. 4.2d). In addition, the cells that were with high (>1.5) Axin2-GFP levels, but not in contact with Paneth cells demonstrated a significant decrease in Axin2-GFP signals (Fig. 4.2c), while cells in direct contact with Paneth cells showed the most increase of Axin2-GFP levels (Fig. 4.2d). The slopes of Axin2-GFP signals of the rest cells were close to or below zero (Fig. 4.2d). These results, especially the rapid decline of the Axin2-GFP signal for cells not in contact with Paneth cells, are not compatible with the division dilution model where the

level of Axin2-GFP should stay constant until the next cell division. Such a decline instead points towards a model where degradation of Wnt ligands plays a dominant role.
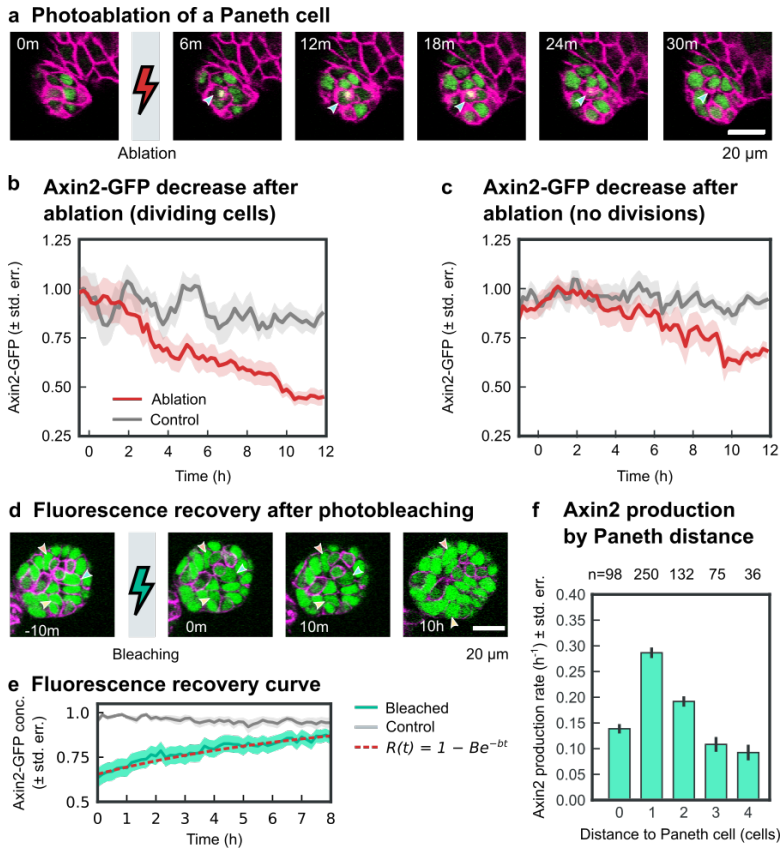
4.2.3 Ablating a Paneth cell causes a decline of Axin2-gfp in the neighbor cells

To further test whether loss of Paneth cell contact indeed causes the decline of cells' Axin2-GFP signals, we ablated single Paneth cells using an 800 nm laser in three different organoids [173]. We selected organoids with small crypts where most of the Paneth neighbors are not in contact with another Paneth cell. The ablation immediately destroyed the targeted cell and left a clear wound in the epithelium which healed within half an hour (Fig. 4.3a). We tracked Axin2-GFP levels of the original neighbors of the ablated Paneth cell for 10 hours. During this time, we saw a ~50% decline of the Axin2-GFP signal in the neighboring cells (Fig. 4.3b). No decline was observed in the two control organoids where Paneth cells were maintained (Fig. 4.3b).

The observed decrease in Axin2-GFP could be the result of passive dilution by cell growth or division. To test if this is true, we added palbociclib to the medium to prevent cell divisions and cell growth in the organoid (Fig. S4.2a, b). Ablation of Paneth cell led to a decrease in Axin2-GFP of about 33% (Fig. 4.3c) when divisions and growth were inhibited. Therefore, we conclude that the decrease in Axin2-GFP is not due to cell growth or division.

Notably, the ablation did not affect the second-degree neighbors of the Paneth cells. The Axin2-GFP signals in the second-degree neighbors showed a rapid decline, regardless of whether the Paneth cell was removed or not (Fig. S4.2c). This indicates that Paneth cells are indeed not able to sustain Wnt pathway activity in their second-degree neighbors [45], which makes our data incompatible with the spatial Wnt diffusion model. Instead, our results point towards a timer model. In this model, the Wnt proteins have high turnover rates. A continuous supply of Wnt proteins from Paneth cells is required to keep activating the signaling pathway. After the loss of contact with Paneth cells, a cell will not receive new Wnt proteins. Meanwhile, a timer to decrease Wnt signaling levels will be triggered.

To test whether such a timer model is plausible, both the GFP production and degradation rates need to be measured. The Axin2 production rate is equal to the GFP production rate, as the gene for the SGFP2-protein has been fused to the 3' end of the Axin2 gene [164]. In the Fluorescence Recovery After Photobleaching (FRAP) experiment, bleached cells showed a fluorescence recovery after approximately 8 hours (Fig. 4.3d, e). By fitting an exponential curve to the GFP recovery dynamics, we obtained the degradation rates of GFP: 16% per hour (Materials and Methods). Furthermore, the Axin2 and GFP production rates can be obtained based on the slope of the Axin2-GFP curves and the GFP degradation rates (Materials and Methods). The neighbors of Paneth cells had the highest Axin2-GFP production rates (Fig. 4.3f). And the second-degree neighbors showed significantly lower productions (Fig. 4.3f). Other cells, including Paneth cells and cells distant from Paneth cells, had very limited Axin2 production.

4

Fig 4.3: Ablating a Paneth cell caused decline of Axin2-GFP levels among the Paneth neighbors. a. Ablation of a single cell with a near-infrared laser. The tissue healed within 30 minutes. b. Influence of the ablation of Paneth cells on the Axin2-GFP signals of direct Paneth neighbors. Three Paneth cells were ablated in three different organoids. c. The influence of the ablation of Paneth cells on the Axin2-GFP signals of direct Paneth neighbors in organoids where cell divisions were inhibited. d. Example of fluorescence recovery in a crypt with three bleached cells. e. Fluorescence recovery curve of Axin2-GFP over time (n=6). f. Axin2 production rate plotted against distance to the nearest Paneth cell.

4.2.4 A timer model ensures robust differentiation

Inactivation of Wnt signaling can make a cell differentiate, as the Wnt target gene Ascl2 acts as a switch for stemness [136]. However, how this process is regulated in time remains unknown. What is the mechanism that prevents differentiation from happening too early or too late? We used antibody staining to identify the cell types, such as stem cells, Paneth cells, enteroendocrine cells, enterocytes, and goblet cells (Materials and Methods). In addition, a group of cells stained negative for both the stem cell marker and the markers of the differentiated cell types. They resemble the transit amplifying cells and are thus referred to as TA-like cells. We quantified the Axin2-GFP levels of different cell types (Fig. 4.4a). The measured Axin2-GFP levels of all cell types correlate with the single-cell RNA sequencing expression levels (dataset from Haber et al. [58], Fig. S4.3, sequencing data acquired at NCBI GEO database [9], accession GSE92332), and also correlate with the expression of other intestinal Wnt target genes that are important for cell fates, such Lgr5, Sox9, Myc, and Ascl2 [136]. Cell types with lower Axin2-GFP levels are also located further away from Paneth cells (Fig. 4.4b).

Next, we linked the Axin2-GFP dynamics to the cell types. We focus on cells identified as stem cells and TA-like cells at the endpoint. And only cells that were initially in contact with Paneth cells were selected. All of the selected cells had similar Axin2-GFP levels at the beginning. However, during the imaging, TA-like cells had less contact with Paneth cells and lower Axin2-GFP levels compared with stem cells (Fig. 4.4c). In addition, the Axin2-GFP levels of TA-like cells staying out of contact with Paneth cells during imaging gradually approached the Axin2-GFP levels of fully differentiated cells (Fig. 4.4d). These observations suggest that differentiation also starts after losing contact with Paneth cells.

Does being in contact with one Paneth cell guarantee stemness? In Fig. 4.4c, we noticed that only about half of Paneth cells' neighbors are stem cells. The rest are TA-like cells. They have lower Axin2 production rates compared to stem cells (Fig. 4.4e). One could assume that a single Paneth cell does not provide sufficient Wnt proteins to reliably sustain the stemness of its neighbor. In that case, multiple Paneth cells would be required to maintain a stem cell. However, we found that cells next to only one Paneth cell and cells next to two Paneth cells have the same Axin2-GFP levels and Axin2 production rates (Fig. 4.4f). Therefore, one single Paneth cell supplies sufficient Wnt proteins for maintaining stemness.

The occurrence of TA-like cells next to Paneth cells could result from some Paneth cells only secreting low amounts of Wnt proteins. However, even if all Paneth cells secreted ample amounts of Wnt proteins, the timer model would still predict that some cells next to a Paneth cell are TA-like cells. Epithelia are complex environments where cells can frequently lose and regain contact with other cells [5, 55]. Thus, we expect some TA-like cells to regain contact with Paneth cells. Once it occurs, TA-like cells will accumulate Wnt proteins. It takes time to accumulate sufficient Wnt proteins to activate the Wnt pathway and regain stemness. During the accumulation, these cells would still be identified as TA-like cells. Indeed, we observed some cells gaining contact with Paneth cells during imaging. And their Axin2 production rates increased after gaining contact with Paneth cells (Fig. S4.4).

If the crypt follows the timer model for differentiation, the duration of a cell being in contact with Paneth cells should be a better predictor of differentiation than the distance to the nearest Paneth cell. Indeed, Fig. 4.4g is consistent with this hypothesis. As illustrated in Fig. 4.4h, in the timer model any cell that is not in contact with Paneth cells for long enough would differentiate, irrespective of the distance to the Paneth cell.

In a way, a passive division dilution model is also a timer model, with the cell division functioning as the time step. However, in the division dilution model, the decrease in Wnt signaling is restricted to only 50% per cell cycle, while the timer model can achieve faster decreases. In addition, the division dilution model would lead to more variation in the timing of differentiation, since slowly dividing cells would differentiate much later than the fast-dividing cells. Furthermore, a simple computational model (Fig. S4.5) showed that the transition zone of stem-to-TA would be twice as broad in a division dilution model, compared to a timer model.
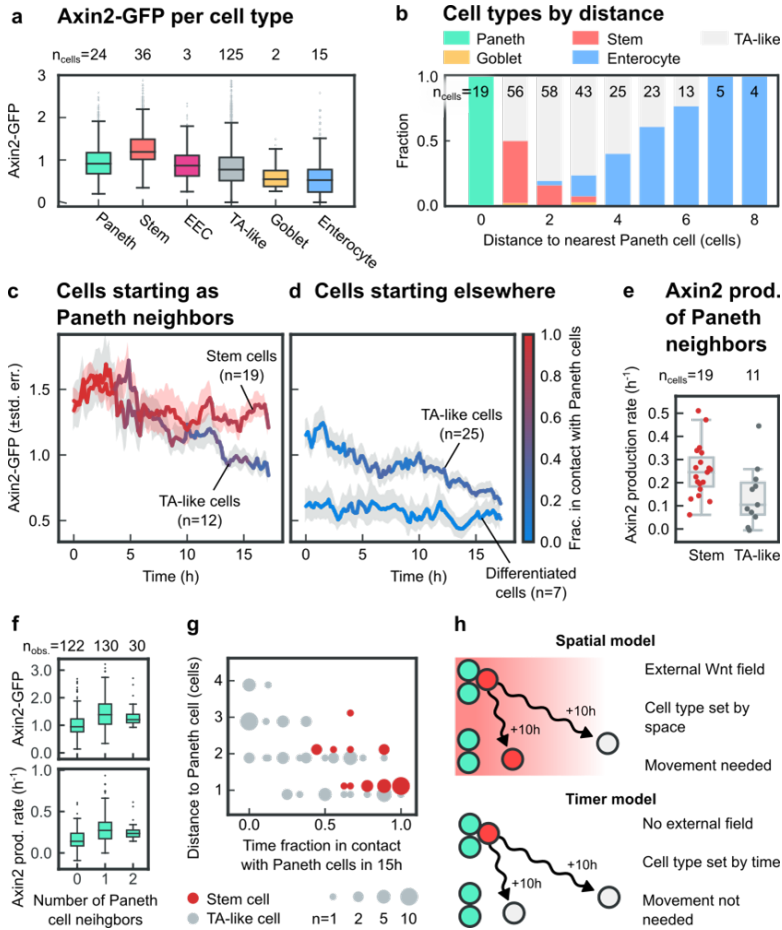
Fig 4.4: A timer model ensures robust differentiation. a. Axin2-GFP levels of various cell types, measured from the last division until the end of the time lapse. b. Distance to the nearest Paneth cell for various cell types at the end of the time lapse. c. Axin2-GFP levels of stem cells and TA-like cells that were initially in contact with Paneth cell. The color encodes the fraction of cells in direct contact with Paneth cells at different time points. d. Axin2-GFP levels of differentiated cells (goblet cells and enterocytes) that were out of contact of Paneth cells. e. Axin2 production rate measured for neighbor cells of Paneth cells, which are either stem cells or TA-like cells. The rate was averaged over the last four hours when the cell was present. In case a cell was less than four hours old at the end of the time lapse, we used the last four hours of the mother cell instead (p= 0.027; two-sided t-test assuming equal variance). f. Axin2-GFP levels and the production rates plotted against the number of Paneth cells that they are in contact with. g. Dot plot of distances to Paneth cells and the fraction of time that a cell has been in contact with a Paneth cell within 15 hours. h. Illustration of the main differences in the spatial and timer models.

4.3 Discussion

In this chapter, we imaged and tracked cells in intestinal organoids carrying an Axin2 reporter to follow the spatio-temporal dynamics of Wnt signaling. We used laser ablation to remove single Paneth cells. And endpoint antibody staining was performed to identify cell types. We showed quantitatively that cells rapidly reduce their Wnt signaling levels once their contact with Paneth cells is lost. This reduction was observed both in cells moving away from the Paneth cells and in cells whose neighbor Paneth cells are ablated. Such reduction is not due to dilution caused by cell growth or division, as we also observed the rapidly reducing Wnt signaling in conditions where growth and proliferation are inhibited. If Paneth cell contact is not regained in time, cells differentiate even if they remain close to Paneth cells. These findings contract the two current models for Wnt signaling pathways: the spatial diffusion model and the division dilution model. As a result, we proposed a timer model for Wnt signaling in the intestinal crypt. Once a cell loses contact with Paneth cells, the source of Wnt, its Wnt signaling levels will start decreasing. Stem cells will differentiate if their Wnt signaling levels become too low [136]. They will not differentiate if Paneth cell contact is only lost briefly. While we have shown that Axin2 expression decreases upon loss of contact with Paneth cells, we have not investigated the underlying molecular mechanism to achieve such responses. Wnt signaling is known to be controlled by both antagonists and potentiators. Both positive and negative feedback loops are involved in the regulation [106]. The rapid decrease of Wnt signaling levels observed in this chapter might be regulated via a negative feedback loop since Axin2 is also known to be part of the β-catenin destruction complex [72]. Such questions will require follow-up studies to address completely.

4.4 Materials and methods

4.4.1 Organoid culture

$Axin2^{P2A-rtTA3-T2A-3xNLS-SGFP2HOM}$;$Rosa26^{mTmG}$ murine intestinal organoids were gifts from the Van Amerongen lab (Universiteit van Amsterdam, The Netherlands) and are described in [164]. Organoids were cultured in 24-well cell culturing plates, at 37°C and 5% CO_2. Within each well, the organoids were embedded in 40 μL gel consisting of basement membrane extract (BME, Trevingen) mixed with Advanced DMEM/F-12 in a 2:1 to 3:1 volume ratio. The gel was overlaid with 0.4 mL growth medium. This medium consisted of Advanced DMEM/F-12 (Life Technologies) with the following added ingredients: murine recombinant epidermal growth factor (EGF 50 ng/mL, Life Technologies), murine recombinant Noggin (100 ng/mL, Peprotech), human recombinant, R-spondin 1 (500 ng/mL, Peprotech), n-Acetylcystein (1 mM, Sigma-Aldrich), N2 supplement (1x, Life Technologies), B27 supplement (1x, Life Technologies), Glutamax (2 mM, Life Technologies), HEPES (10mM, Life Technologies), Penicillin/Streptomycin (100 U/mL 100 $\mu g/mL$, Life Technologies). The organoids were passaged every week. The medium was refreshed every two to three days.

4.4.2 Time-lapse imaging

We first seeded mechanically dissociated organoids in 40 μL BME gel in four-well chambered cover glass (Cellvis). This was performed one day before the start of the time-lapse experiment. To prevent the gel from solidifying immediately, seeding was performed on a cold block. The imaging well was then put in a fridge until the organoids sank down to the bottom of the wells. Typically, this sedimentation process took about five to ten minutes. Afterwards, the chambered cover glass was put in the incubator for 20 to 30 minutes before the growth medium was added. ~ 3 hours before starting imaging, the growth medium was replaced by new growth medium supplemented with 1 μM SirDNA (Spirochrome) and 10 μM Verapamil (Spirochrome). SirDNA was used to mark the nuclei, allowing us to track Axin2-negative cells more easily.

A Leica confocal microscope was used for time-lapse imaging. In this setup, a controlled closed environment was used to maintain the temperature at 37°C, CO_2 at 9% and high humidity. The CO_2 concentration was kept at 9% instead of 5% due to leakiness of the system. A 40x water immersion objective (Leica) was used for image acquisition. Organoids were imaged every 12 minutes for up to 20 h. Z-stacks were made at 2 μm intervals, with a field of view of 233 by 233 μm. Z-ranges were specified for each organoid, with a maximum range of 70 μm. The following excitation wavelengths and laser intensities were used: 488 nm (3% or 1% intensity), 552 nm (1% intensity), 638 nm (1% intensity). An imaging well typically contained over 50 organoids, of which we only imaged a small number that were with only one to three crypts and close to the image plate bottom.

4.4.3 Antibody staining and cell type identification

After time-lapse imaging, organoids were immediately fixed using 4% formaldehyde in PBS. After fixation, the organoids were permeabilized using 0.2% Triton-X. The organoids

were then sequentially stained with several rounds of primary and secondary antibodies and dyes, as shown below.

Primary antibodies	Dilution	Product information
Rabbit anti-lysozyme [EC 3.2.1.17]	1:800	Dako #A0099
Rabbit anti-Olfm4 [D6Y5A] XP	1:500	Cell signaling technology #39141
Mouse anti-Human Cytokeratin 20 [Clone Ks20.8]	1:500	Dako #M701929-2
Mouse anti-Chr-A [C-12]	1:50	Santa Cruz Biotechnology #sc-393941

Dyes	Dilution	Product information
WGA conjugated to CF©488A	$5\mu g/ml$	Biotium

Secondary antibodies	Dilution	Product information
Goat anti-rabbit IgG *H&L* (Alexa Fluor©405) pre-adsorbed	1:1000	Abcam #ab175654
Donkey anti-Mouse IgG *H&L* (Alexa Fluor©647)	1:500	Thermo Fisher #A31571
Donkey anti-Rabbit IgG *H&L* (Alexa Fluor©405)	1:1000	Abcam #ab175649

Organoids were blocked in 5% skim milk for 1 h. Primary antibodies were diluted in the blocking solution and added to the blocked organoids. Organoids were incubated with the primary antibodies for two days and then washed with PBS. Following that, organoids were incubated with secondary antibodies diluted in TBS, for 1 h. If applicable, the organoids were also incubated with Wheat Germ Agglutamin (WGA) in PBS for 2 h. Imaging of stained organoids was done using the same Leica confocal microscope setup as for time-lapse imaging.

Using these combinations of antibodies and dyes mentioned before, different cell types can be identified.

Marker	Stem cell	Paneth cell	Goblet cell	Enterocyte	Enteroendocrine cell
Olfm4	+	-	-	-	-
Lysozyme	-	+	-	-	-
WGA	-	+	+	-	-
Cytokeratin 20	-	-	+	+	-
Chra	-	-	-	-	+

4.4.4 Ablation of Paneth cells

Imaging was performed on a confocal microscope (Nikon A1R MP) with a 40x oil immersion objective (NA = 1.30). 30 z-slices with 2 μm step size were taken per organoid every 12

minutes. Experiments were performed at $37°C$ and $5\text{-}8\%\ CO_2$, achieved by using a stage-top incubator (Okolab). Ablation was carried out using an 800 nm laser (tunable Ti:Sapphire laser, Mai Tai High Performance DeepSee, Spectra Physics; 100% power) for 40 to 60 ms, on a single point set at the center of the nucleus. Paneth cells were identified by their bright membrane-localized tdTomato signal and their low Axin2-GFP signal amidst neighbor cells with high Axin2-GFP signals (Fig. 4.1a).

4.4.5 Fluorescence recovery after photobleaching

The experiment was performed on the same microscope as the ablation experiments. GFP in three cells per crypt was partially bleached for 5 seconds at 20% laser power (Nikon LU-N4 laser unit, 488 nm laser). The remaining cells served as controls. Bleached and control cells were manually tracked for up to 10 hours and fluorescence intensity levels of GFP signal were measured until cell division, death or moving out of frame. Fluorescence intensities were measured using a manually drawn 2D ellipse inside the nucleus [126, 133, 134]. For each individual recovery curve, we normalized the fluorescence intensity by the average intensity of the four images taken before bleaching, and we fitted the function $f(t) = 1 - Be^{-bt}$ to the individual recovery curves in Python with the fraction of bleached molecules B and the degradation rate of GFP b as free fitting parameters. Cells that showed less than 5% recovery in the first 100 minutes were excluded from analysis.

4.4.6 Automatic extraction of fluorescence values

For extracting fluorescence curves outside the FRAP experiment, a different, less labor-intensive method was used compared to drawing ellipses. In addition, instead of measuring the fluorescent concentration, this method measures the total fluorescence of a nucleus. The centers of the nuclei in the crypt were manually tracked from the start to end of the time-lapse imaging in OrganoidTracker [79]. The automated tracking module of OrganoidTracker could not be used, as the cells do not contain a nuclear reporter. Every pixel in the 3D images was then assigned to the nearest nuclear center position, with a maximum distance of 7 μm (Fig. S4.6). The sum of intensities of all pixels belonging to a cell is regarded as the total fluorescence of the cell. When a trace of a single cell is shown in this chapter, the measured values are averaged over the two hours before and the two hours after. When multiple cells are shown together, the Axin2-GFP values of the cells are averaged, but no time averaging is performed.

4.4.7 Measuring GFP production and degradation

We set up a simple production-degradation model to describe how the GFP signal evolves over time:

$$\Phi \underset{f}{\overset{b}{\rightleftharpoons}} G$$

Here, G is the measured concentration of GFP, which can be produced at rate f and degraded at rate b. This reaction equation results in the following differential equation:

$$\frac{dG}{dt} = f - b * G(t)$$

We assume that the GFP degradation rate b is equal in all cases, but we allow the production rate f to vary over time for each cell. This setup allows us to measure b from a Fluorescence Recovery After Photobleaching (FRAP) experiment, which then enables measuring f for all other cells. Because GFP and Axin2 are produced together, we can measure the production rate of Axin2 for all cells with this model.

For the FRAP experiment, we bleached several cells in the bottom of the crypt (Fig. 4.3d). Cells here show a constant amount of GFP, as verified by the gray line in Fig. 4.3e. Therefore, for these cells $dG/dt = 0$, and the recovery of the bleached cells can be fit to $\frac{G(t)}{G_0} = 1 - Be^{(-bt)}$ to obtain the degradation rate b. Here, G_0 is the measured concentration of GFP before bleaching and B the fraction of bleached GFP.

4.4.8 Determining neighbors of cells

Neighbors of cells were manually annotated every 10 time points, which corresponds to every two hours. To do this, connections were established between all cells for which the membranes touched, as observed in the tdTomato channel.

4.4.9 Computational model

A one-dimensional array of cells was set up. This array represents a column of cells, with the crypt at the bottom and the villus region at the top. The length of the column was set to 14. All cells in the simulation are proliferating. For each position in the column, the program stores whether a cell that occupies that position is currently in contact with a Paneth cell. The Paneth cells themselves are not modelled explicitly. In addition, for each cell the program stores its Wnt and Axin2 level. The entire situation is sketched in Fig. S4.5a.

Note that whenever a cell moves, it takes its Wnt and Axin2 levels with it to the new position. However, the state of whether the cell is currently in contact with a Paneth cell is not moved along with the cell. The reasoning here is that bound Wnt proteins and Axin2 proteins move together with a cell, but the Paneth cells stay at their original position.

The simulation proceeds in time steps of 5 minutes. In every time step, the following actions are performed for each cell, proceeding from the bottommost cell to the topmost cell:

Simulating divisions. The time until the next division is decreased by 5 minutes. If the timer reaches zero or becomes negative, the cell divides. Division proceeds as follows: The cell is replaced by two daughter cells, which pushes all cells above one position upwards. This causes the topmost cell in the column to be removed from the simulation. The Wnt and Axin2 levels of the mother cell are divided equally over the two daughter cells. Therefore, for each daughter cell the Wnt and Axin2 level is half of that of the mother cell. Both daughter cells have their division timer reset to a value drawn from a Gaussian distribution with a mean of 16.2 hours and a standard deviation of 3.2 hours.

Simulating rearrangements. With a chance of 1 in 16 per hour (or equivalently 1 in 192 per time step of 5 minutes), the cell swaps with the cell above. As an exception, the topmost cell in the column cannot swap. This rearrangement rate corresponds to about one rearrangement for every division, which follows our experimental observation.

Updating Paneth contact. If the cell is in contact with a Paneth cell, it has a chance of 1/32 per hour to disconnect, which approximates the experimentally observed rate. Else, if the cell is not in contact with a Paneth cell, it has a defined chance to connect to a Paneth cell. This chance depends on the position in the column and has been defined such that cells at that position will be in contact for a certain fraction of their time. These fractions are, from bottom to top, 0.75, 0.65, 0.55, 0.45, 0.35, 0.25, 0.15, 0.05, 0, 0, 0, 0, 0 and 0, and approximate the experimental data. The chance of gaining Paneth contact is then calculated for each position as $\frac{Paneth contact time fraction}{1 - Paneth contact time fraction} \cdot Paneth disconnect chance$.

Updating Wnt. The Wnt level of the cell is updated as follows:

$$Wnt_{new} = Wnt_{old} + (f_{Wnt} - b_{Wnt} \cdot Wnt_{old}) \cdot \Delta t$$

The production rate per hour f_{Wnt} was set to 1/6 if the cell was in contact with a Paneth cell, otherwise it was set to 0. The degradation rate per hour b_{Wnt} was set to 1/6 for the timer model and 0 for the division dilution model. Δt is the duration of a time step in hours, which for a time step of 5 minutes is equal to 5/60.

Updating Axin2. The Axin2 level of the cell was updated as follows:

$$Axin2_{new} = Axin2_{old} + (f_{Axin2} - b_{Axin2} \cdot Axin2_{old}) \cdot \Delta t$$

The production rate per hour was set to scale with the Wnt level: $f_{Axin2} = Wnt_{new}$, the degradation rate per hour b_{Axin2} was set to 1/6.2. Δt is still the duration of a time step in hours.

A crypt is simulated by first running the simulation for one thousand hours, and then recording the crypt for 17 hours. The output of the recording of 20 crypts is then analyzed using the same scripts as that were used for experimental data.

4.4.10 RNA sequencing data analysis

Single-cell RNA sequencing data of organoids cultured in control conditions [58] were obtained from the GEO database [9, 41] using accession number GSE92332. Normalization, feature selection and scaling of the UMI count table was done using the R package Seurat v4 [59].

4.5 Supplementary figures
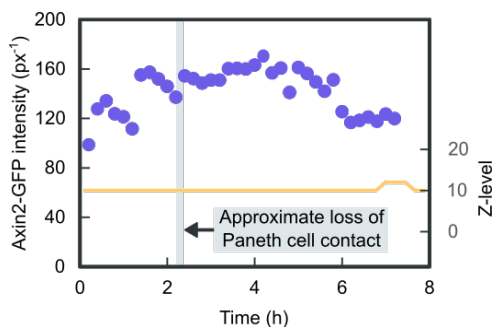
Fig S4.1: Axin2-GFP level decreased after losing contact with Paneth cells. The Axin2-GFP concentration over time was manually measured (hand-drawn eclipses within the nucleus). Once the cell lost contact with the Paneth cell, the Axin2-GFP concentration first stopped increasing, and then started to decrease after a few hours. The cell remained at the same height from the objective and did not divide. Therefore, the decrease in GFP signal must be due to degradation. The cell shown here is the same cell in Fig. 4.2a.
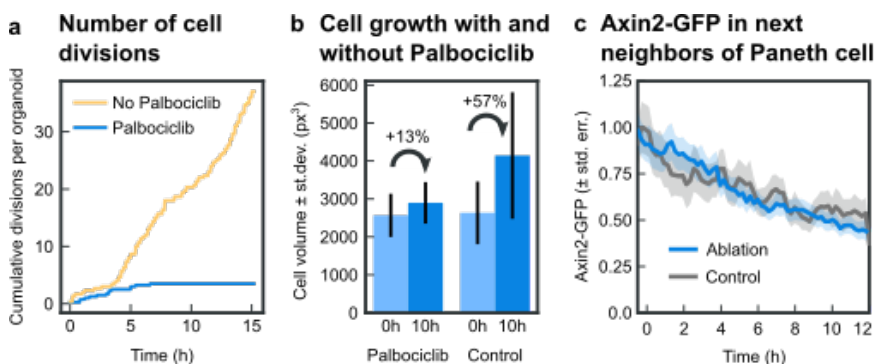
Fig S4.2: Ablating a Paneth cell caused decline of Axin2-GFP levels among the Paneth neighbors. a. Cumulative number of cell divisions for organoids in normal medium and for organoids where Palbociclib was added to the medium several hours before imaging. b. Effect of Palbociclib on cell volume growth. If a cell divides (in the normal medium condition only), the volume was summed by adding the volumes of the two daughter cells. c. Decrease of Axin2-GFP signal in the next neighbors of a Paneth cell in three organoids (in the normal medium condition, without Palbociclib). The next neighbors of Paneth cells (not direct neighbor but two cells away) showed the same decrease in Axin2-GFP both near the ablation regions and far from the ablation regions.
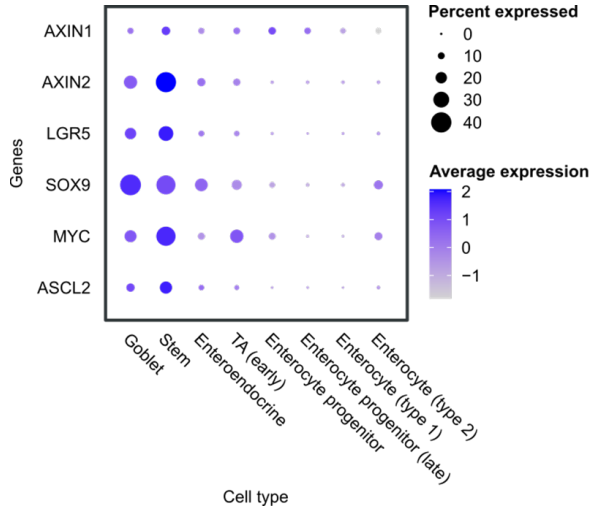
Fig S4.3: The expression of a set of genes in various cell types in intestine. All the genes are Wnt target genes, except for AXIN1 which is part of the Beta-catenin destruction complex and used as a baseline for gene expression. Data from the mouse intestinal organoid dataset of Haber et al. [58] (data accessible at NCBI GEO database [9], accession GSE92332).
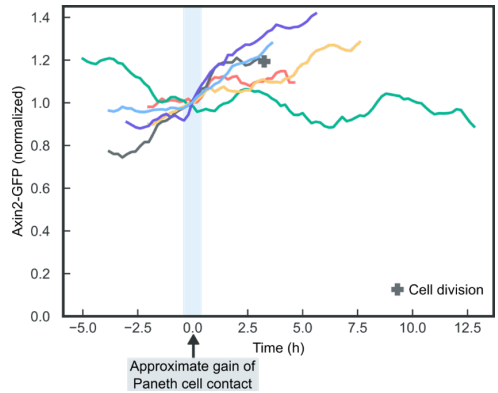
Fig S4.4: Axin2-GFP levels of individual cells that were initially out of contact with Paneth cells for at least two hours, and then regained contact for at least three hours. The time axis was defined such that time point zero corresponds to the approximate moment in which Paneth cell contact was gained. Axin2-GFP levels were normalized such that they are set to 1 at time point zero. Axin2-GFP levels are displayed until a cell loses Paneth contact again, or until the cell divides.

4
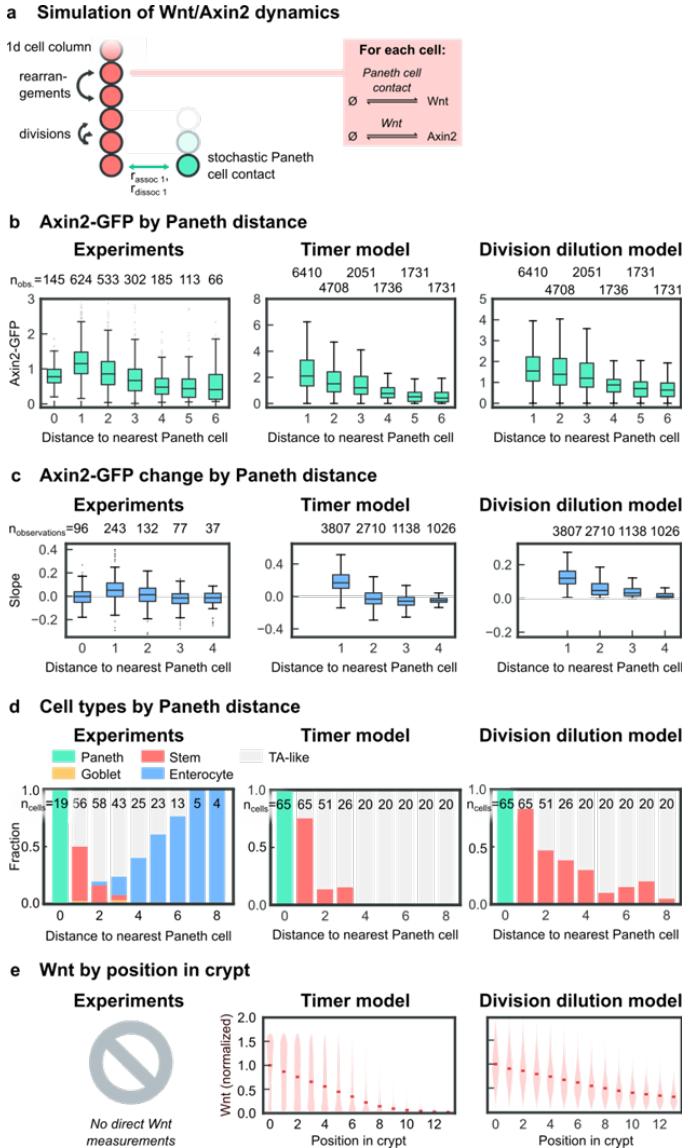
Fig S4.5: Comparisons of the computational models with experimental data. a. Illustration of the computational model. Cells are placed in a 1d-column and can rearrange and divide. Each cell can associate and dissociate from a Paneth cell, at rates that depend on the position. Cells that are in contact with Paneth cells activate their Wnt signaling, and Axin2 production is linear with the Wnt level. b. Axin2-GFP signal as a function of the distance to the nearest Paneth cell. Left panel is a copy of Fig. 4.1c, other panels are a result of performing the same analysis on simulation data. c. Change of Axin2-GFP signal over time as a function of the distance to the nearest Paneth cell. Left panel is a copy of Fig. 4.2d, other panels are a result of performing the same analysis on simulation data. d. Cell type frequencies as a function of distance to the closest Paneth cells. Left panel is a copy of Fig. 4.4b, other panels are a result of performing the same analysis on simulation data. e. Wnt levels as a function of the position in the crypt. Position 0 the bottom of the crypt, position 13 would be in the villus.
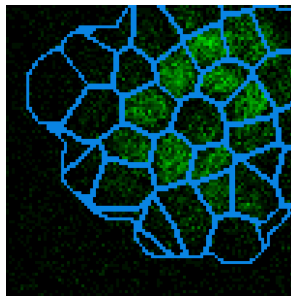
Fig S4.6: Measurement of Axin2-GFP signal. Every pixel is assigned to the closest nucleus center, with a maximum distance of 7 *μm*.

5

CONCLUSION AND OUTLOOK

This final chapter briefly summarises the main findings of this thesis. We also propose promising future routes to apply live cell tracking methods in organoids to obtain more insights into organ development and disease mechanisms. This includes tracking in platforms such as healthy human intestinal organoids, organoids recapitulating Inflammatory Bowel Disease, cancer organoids, and organoids co-cultured with bacteria and immune cells. These applications will advance our knowledge of the differentiation trajectories in the human intestine, the influence of signaling pathways on the differentiation dynamics, the microbes-epithelium interactions, the Inflammatory Bowel Disease development, and cancer development and treatment.

In this thesis, we presented several key discoveries regarding the regulation of proliferation and differentiation in mouse small intestinal organoids, which model intestinal tissue homeostasis. These studies were all driven by live-cell tracking methods (**Chapter 1**) with adaptations tailored to specific research questions. We first performed time-lapse microscopy to track cells in growing crypts for many generations to reconstruct the lineage dynamics. Surprisingly, we found highly symmetric proliferative behaviors between sister cells, suggesting that the daughter cell proliferation is controlled by the mother cells. Our simulation revealed that this proliferative symmetry in sisters can be a good strategy to minimize cell number fluctuations and ensure homeostasis (**Chapter 2**). Next, we investigated the cell type transitions during differentiation with our TypeTracker method, which is an integrated approach combining live-cell tracking, multiplexed endpoint antibody staining, and a backpropagation algorithm to infer differentiation trajectories. It has brought several novel insights regarding cell fate commitment that challenged the conventional knowledge, such as the early commitment of secretory cells before terminal division, the cell type abundance regulated by proliferation, and a potential 'commit-then-sort' model where spatial patterning is achieved after commitment. The results also questioned the existence of an omnipotent secretory progenitor (**Chapter 3**). The Wnt signaling pathway is known to play a significant role in intestinal homeostasis and differentiation. However, the spatiotemporal dynamics of Wnt signaling remain unknown. We, therefore, utilized mouse intestinal organoids carrying an Axin2 reporter (a Wnt target gene). We interrogated the organoids by imaging and tracking Axin2 dynamics, monitoring the contact between cells, and perturbing the system via ablating single cells. We learned that the loss of contact with a Paneth cell leads to a fast decline in Axin2 levels, even when divisions and growth are inhibited. This finding suggests a timer model where Wnt degrades rapidly after losing contact with Paneth cells, contradicting two important proposed models: the spatial gradient model and the division dilution model (**Chapter 4**).

These findings help advance our knowledge of the intestinal organization. Here, we also propose some potential future projects based on our methods to further strengthen the understanding of tissue homeostasis and disease development.

Follow differentiation dynamics in human organoids. Mice and mouse intestinal organoids have been used frequently to model human intestinal organization. The intestines in both species are anatomically similar. However, due to diverging diets, feeding patterns, body sizes, and metabolic requirements, differences in intestinal development between humans and mice should be considered when translating results from mouse models to humans [104]. Consequently, human intestinal organoids are better model systems to monitor the development of human tissues and diseases. Nonetheless, most of the current human intestinal organoids [51, 71, 113] could not fully recapitulate the cell type diversity and 3D structure of the intestinal tissues yet, such as the generation of Paneth cells or budding. Recently, an optimized culture protocol, with Interleukin 22 (IL-22) supplemented in the medium, has been reported, enabling the human organoids to generate extensive budding and harbor all cell types including Paneth cells [62] (Fig. 5.1a). In this study, the organoids carried fluorescent reporters tagging key genes to characterize different secretory cell types, including Mucin2 (MUC2) for goblet cells, Defensin Alpha 5 (DEFA5) for Paneth cells, and Chromogranin A (CHGA) for Enteroendocrine cells (Fig. 5.1a). We participated in this study with our live cell tracking approach to investigate the origin of Paneth

cells. We performed time-lapse imaging in all three fluorescent channels simultaneously, manually tracked single cells, such as Paneth cells and goblet cells, and then quantified the fluorescence signals of each tracked cell [62]. MUC2 is a protein that forms a mucus layer within the intestine and characterizes goblet cells. Most of the MUC2+ cells were goblet cells and they showed high MUC2 expression throughout the imaging, but no fluorescence of other markers (Fig. 5.1c). We also observed a decrease in MUC2 expression in some cells, accompanied by an increase in the expression of DEFA5, an antimicrobial peptide (Fig. 5.1b). These cells were Paneth cells and we directly observed them being generated from MUC2+ cells, which might be the secretory progenitor cells [62]. Furthermore, introducing a nuclear reporter to the organoids and applying TypeTracker will reveal the differentiation dynamics of all other cell types. In addition, quantitation of marker gene expression levels will generate gene expression dynamics during inferred type transitions.
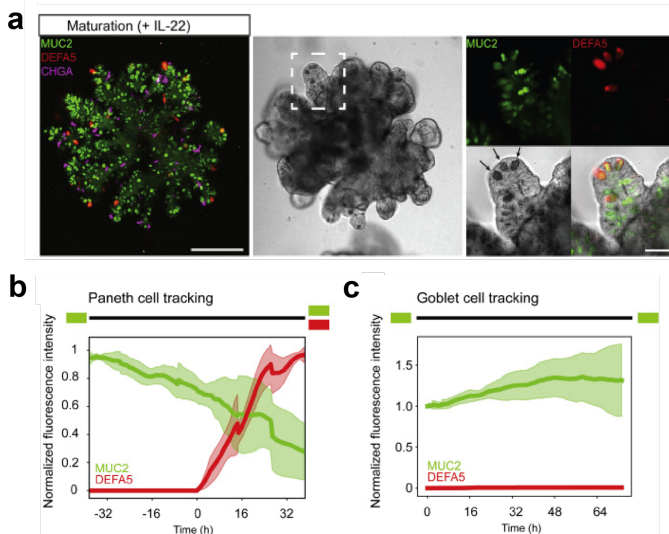
Fig 5.1: IL-22 was used to increase the number of active Paneth cells (DEFA5+) in human small intestinal organoids [62]. a, Fluorescence images of human intestinal organoids with goblet cells (MUC2+), Paneth cells (DEFA5+), and Enteroendocrine cells (CHGA+). b, Temporal dynamics of normalized fluorescence signals in single Paneth cells, averaged from 3 organoids, 8 Paneth cells with standard error (shadow area). c, Temporal dynamics of normalized fluorescence signals in single goblet cells, averaged from 3 organoids, 7 goblet cells with standard error (shadow area).

Follow the influence of signaling pathways on the differentiation trajectories. In the intestinal epithelium, the balance between stem cell self-renewal and differentiation is coordinated by several signaling pathways, such as the Wnt/β-catenin, Notch, BMP, and EGF signaling pathways [15, 150]. The effect of these signals on cell fate specification has been studied extensively. In these studies, the cell type composition of the intestine was investigated after blocking or enhancing certain signaling. For instance, blocking Notch signaling via gamma-secretase inhibitor led to a massive conversion of proliferative cells into secretory cells [167]. However, the dynamic processes of such conversions have never been addressed. Applying the TypeTracker method to intestinal organoids before and after

the signaling perturbations, such as adding DAPT to the medium to block Notch signaling, can resolve the type transition dynamics caused by the perturbations. It can further indicate where the conversions occur, right above the stem cell compartment or throughout the crypt. Our tracking method is also compatible with other advanced manipulation techniques, such as optogenetics [60] and microfluidics [149]. These techniques modify signal levels in pulses or within individual cells, and will facilitate understanding of signal dynamics to an unprecedented degree. Interestingly, perturbing signaling pathways, by adding or withdrawing certain components in the growth medium, can also enrich specific cell types [19]. Therefore, tracking organoids in such medium conditions further enables following the differentiation dynamics of rare cell types, such as Tuft cells.

Follow the microbes-epithelium interactions. Microbial communities play an important role in mediating human health and disease. The majority of these microorganisms reside within the intestines [43]. The gut microbiota increases nutrient uptake, protects the host against foreign pathogens, and contributes to the development of intestinal mucosa and the immune system [172]. It is also involved in the development of human diseases such as infectious diseases, liver diseases, gastrointestinal cancers, and metabolic diseases [43, 172]. Therefore, understanding the interactions between the microbiota and the epithelium is of significant importance. Intestinal organoids are useful tools to follow the microbes-epithelium interactions *in vitro*. Several approaches have been used so far for introducing microorganisms into organoids: disrupted organoids, 2D organoid culture, and microinjections [124]. For instance, human intestinal organoids were exposed to genotoxic pks^+ E.coli that was injected into the lumen. Sequencing the organoids before and after the exposure revealed a distinct mutational signature. This signature was also detected in a subset of human colorectal cancer genomes. This study implied that the specific mutational process is caused by past exposure to the genotoxic bacteria [112, 114]. Within such co-culture platforms, the detailed interaction processes are yet to be resolved, such as do bacteria prefer infecting certain cell types or are some cell types more prone to die after infection. Answering these questions is critical in understanding the development of the disease and generating effective treatment. Live cell imaging and tracking will be excellent tools for such research.

Investigate Inflammatory Bowel Disease development. Inflammatory Bowel Disease (IBD) is a prevalent disease around the world. Due to a lack of knowledge of disease mechanisms, it remains difficult to have efficient treatment [3]. Identified mechanisms causing IBD include: loss of immune tolerance to commensal bacteria, inflammatory immune cell defects, defects in autophagy, and tight junction dysregulation [3, 32, 146]. Therefore, IBD is the result of a complex interplay between the intestinal epithelium, the immune system, and the microbiota [128]. These interactions are challenging to understand *in vivo*. Therefore, an *in vitro* co-culture system, including intestinal organoids, the immune system, and the microbiota holds great promise. A previous co-culture model of macrophages and intestinal enteroid monolayers has been developed [105]. Enteroid monolayers are mechanically disrupted 3D organoids seeded on Transwell [3]. This system enables imaging and observation of communication between epithelium and macrophages, such as intraepithelial macrophage projections. In addition, it is compatible with bacterial infections. This co-culture system is an excellent tool for studying the mechanism of IBD. For instance, polymorphisms in Nucleotide-binding oligomerization domain-containing

protein 2 (NOD2) are highly associated with IBD [3]. NOD2 is a pattern recognition receptor expressed by a range of cells, including monocytes, dendritic cells, macrophages, and enterocytes [3]. Recognition of cell wall proteins from bacteria by NOD2 induces a signaling cascade that leads to inducing inflammatory cytokine responses and bacterial clearance [3, 69, 107]. Mutations in NOD2 may reduce the protective mucins and bacterial clearance [116]. The introduction of NOD2 mutations to intestinal organoids and/or immune cells can provide direct observations of the effects of mutations. Issues such as whether NOD2 mutations inhibit the generation of goblet cells or alter the function of goblet cells can be addressed with the live-cell tracking. In addition, different NOD2 mutations can be introduced to understand if some mutations have more significant roles in changing organoid homeostasis and immune responses.

Research the development and treatment of cancer. Cancer organoids are miniature, three-dimensional models made from patient tumors and studied in the laboratory [86, 170]. Performing live-cell tracking in cancer organoids can characterize features important to understand cancer progression, such as the proliferation properties, differentiation dynamics, and division event errors [17]. However, patient organoids often contain multiple mutations. It remains challenging to understand which effects are caused by which mutations. Therefore, introducing each mutation separately to healthy organoids via CRISPR/Cas9 technology offers a better platform for such questions [39]. Spatiotemporal dynamics of organoids carrying a single mutation will bring detailed insights into how each mutation changes the differentiation and divisions. For example, if a mutation can change the cell cycle length or if a mutation enriches certain cell types. Furthermore, a recent study shows that live-cell imaging could also be applied to study the dynamic interactions between engineered immune cells and patient breast cancer organoids [35]. In this study, they recorded the process of the engineered T cells killing cancer organoids and found high heterogeneity in T cells' abilities to kill. They also revealed a specific cluster of engineered T cells with the highest efficiency in killing cancer organoids [35]. These investigations should be expanded to other organoid platforms and immune cells. They have great potential to contribute to the optimization of cellular immunotherapies targeted on solid tumors.

Bibliography

References

[1] A. Alladin, L. Chaible, L. Garcia del Valle, R. Sabine, M. Loeschinger, M. Wachsmuth, J.-K. Hériché, C. Tischer and M. Jechlinger. Tracking cells in epithelial acini by light sheet microscopy reveals proximity effects in breast cancer initiation. *eLife*, 9:e54066, 2020.

[2] F. Amat, W. Lemon, D. P. Mossing, K. McDole, Y. Wan, K. Branson, E. W. Myers, and P. J. Keller. Fast, accurate reconstruction of cell lineages from large-scale fluorescence microscopy data. *Nature Methods*, 11(9):951–958, 2014.

[3] H. C. K. Angus, A. G. Butt, M. Schultz, and R. A. Kemp. Intestinal organoids as a tool for inflammatory bowel disease research. *Frontiers in medicine*, 6:334, 2019.

[4] B. Artegiani, D. Hendriks, J. Beumer, R. Kok, X. Zheng, I. Joore, S. Chuva de Sousa Lopes, J. van Zon, S. Tans, and H. Clevers. Fast and efficient generation of knock-in human organoids using homology-independent crispr-cas9 precision genome editing. *Nature Cell Biology*, 22(3):321–331, 2020.

[5] M. Azkanaz, B. Corominas-Murtra, S. I. J. Ellenbroek, L. Bruens, A. T. Webb, D. Laskaris, K. C. Oost, S. J. A. Lafirenze, K. Annusver, H. A. Messal, S. Iqbal, D. J. Flanagan, D. J. Huels, F. Rojas-Rodríguez, M. Vizoso, M. Kasper, O. J. Sansom, H. J. Snippert, P. Liberali, B. D. Simons, P. Katajisto, E. Hannezo, and J. van Rheenen. Retrograde movements determine effective stem cell numbers in the intestine. *Nature*, 607(7919):548–554, 2022.

[6] Z. Bao, J. I. Murray, T. Boyle, S. L. Ooi, M. J. Sandel, and R. H. Waterston. Automated cell lineage tracing in caenorhabditis elegans. *Proceedings of the National Academy of Sciences*, 103(8):2707–2712, Feb. 2006.

[7] N. Barker. Adult intestinal stem cells: critical drivers of epithelial homeostasis and regeneration. *Nature Reviews Molecular Cell Biology*, 15(1):19–33, 2014.

[8] C. S. Baron and A. van Oudenaarden. Unravelling cellular relationships during development and regeneration using genetic lineage tracing. *Nature Reviews Molecular Cell Biology*, 20(12):753–765, 2019.

[9] T. Barrett, S. E. Wilhite, P. Ledoux, C. Evangelista, I. F. Kim, M. Tomashevsky, K. A. Marshall, K. H. Phillippy, P. M. Sherman, M. Holko, A. Yefanov, H. Lee, N. Zhang, C. L. Robertson, N. Serova, S. Davis, and A. Soboleva. Ncbi geo: archive for functional genomics data sets–update. *Nucleic acids research*, 41:D991–5, Jan 2013.

[10] O. Basak, M. van de Born, J. Korving, J. Beumer, S. van der Elst, J. H. van Es, and H. Clevers. Mapping early fate determination in lgr5+ crypt stem cells using a novel ki67-rfp allele. *The EMBO journal*, 33:2057–68, Sep 2014.

[11] E. Batlle and H. Clevers. Cancer stem cells revisited. *Nature medicine*, 23:1124–1134, Oct 2017.

[12] E. Batlle, J. T. Henderson, H. Beghtel, M. M. W. van den Born, E. Sancho, G. Huls, J. Meeldijk, J. Robertson, M. van de Wetering, T. Pawson, and H. Clevers. Beta-catenin and tcf mediate cell positioning in the intestinal epithelium by controlling the expression of ephb/ephrinb. *Cell*, 111:251–63, Oct 2002.

[13] S. Bel, M. Pendse, Y. Wang, Y. Li, K. A. Ruhn, B. Hassell, T. Leal, S. E. Winter, R. J. Xavier, and L. V. Hooper. Paneth cells secrete lysozyme via secretory autophagy during bacterial infection of the intestine. *Science (New York, N.Y.)*, 357:1047–1052, Sep 2017.

[14] M. A. Betjes, X. Zheng, R. N. U. Kok, J. S. van Zon, and S. J. Tans. Cell tracking for organoids: Lessons from developmental biology. *Frontiers in cell and developmental biology*, 9:675013, 2021.

[15] J. Beumer and H. Clevers. Cell fate specification and differentiation in the adult mammalian intestine. *Nature Reviews Molecular Cell Biology*, 22(1):39–53, 2021.

[16] A. C. F. Bolhaqueiro, B. Ponsioen, B. Bakker, S. J. Klaasen, E. Kucukkose, R. H. van Jaarsveld, J. Vivié, I. Verlaan-Klink, N. Hami, D. C. J. Spierings, N. Sasaki, D. Dutta, S. F. Boj, R. G. J. Vries, P. M. Lansdorp, M. van de Wetering, A. van Oudenaarden, H. Clevers, O. Kranenburg, F. Foijer, H. J. G. Snippert, and G. J. P. L. Kops. Ongoing chromosomal instability and karyotype evolution in human colorectal cancer organoids. *Nature Genetics*, 51(5):824–834, 2019.

[17] Y. Bollen, E. Stelloo, P. van Leenen, M. van den Bos, B. Ponsioen, B. Lu, M. J. van Roosmalen, A. C. F. Bolhaqueiro, C. Kimberley, M. Mossner, W. C. H. Cross, N. J. M. Besselink, B. van der Roest, S. Boymans, K. C. Oost, S. G. de Vries, H. Rehmann, E. Cuppen, S. M. A. Lens, G. J. P. L. Kops, W. P. Kloosterman, L. W. M. M. Terstappen, C. P. Barnes, A. Sottoriva, T. A. Graham, and H. J. G. Snippert. Reconstructing single-cell karyotype alterations in colorectal cancer identifies punctuated and gradual diversification patterns. *Nature genetics*, 53:1187–1195, Aug 2021.

[18] V. Bonis, C. Rossell, and H. Gehart. The intestinal epithelium - fluid fate and rigid structure from crypt bottom to villus tip. *Frontiers in Cell and Developmental Biology*, 9, May 2021.

[19] K. E. Boonekamp, T. L. Dayton, and H. Clevers. Intestinal organoids as tools for enriching and studying specific and rare cell types: advances and future directions. *J Mol Cell Biol*, 12(8):562–568, Aug. 2020.

[20] A. Böttcher, M. Büttner, S. Tritschler, M. Sterr, A. Aliluev, L. Oppenländer, I. Burtscher, S. Sass, M. Irmler, J. Beckers, C. Ziegenhain, W. Enard, A. C. Schamberger, F. M. Ver-hamme, O. Eickelberg, F. J. Theis, and H. Lickert. Non-canonical wnt/pcp signalling

regulates intestinal stem cell lineage priming towards enteroendocrine and paneth cell fates. *Nature cell biology*, 23:23–31, Jan 2021.

[21] S. J. A. Buczacki, H. I. Zecchini, A. M. Nicholson, R. Russell, L. Vermeulen, R. Kemp, and D. J. Winton. Intestinal label-retaining cells are secretory precursors expressing lgr5. *Nature*, 495(7439):65–69, 2013.

[22] J. C. Caicedo, S. Cooper, F. Heigwer, S. Warchal, P. Qiu, C. Molnar, A. S. Vasilevich, J. D. Barry, H. S. Bansal, O. Kraus, M. Wawer, L. Paavolainen, M. D. Herrmann, M. Rohban, J. Hung, H. Hennig, J. Concannon, I. Smith, P. A. Clemons, S. Singh, P. Rees, P. Horvath, R. G. Linington, and A. E. Carpenter. Data-analysis strategies for image-based cell profiling. *Nature Methods*, 14(9):849–863, 2017.

[23] J. G. Camp, F. Badsha, M. Florio, S. Kanton, T. Gerber, M. Wilsch-Bräuninger, E. Lewitus, A. Sykes, W. Hevers, M. Lancaster, J. A. Knoblich, R. Lachmann, S. Pääbo, W. B. Huttner, and B. Treutlein. Human cerebral organoids recapitulate gene expression programs of fetal neocortex development. *Proceedings of the National Academy of Sciences*, 112(51):15672–15677, Dec. 2015.

[24] D. Camsund, M. J. Lawson, J. Larsson, D. Jones, S. Zikrin, D. Fange, and J. Elf. Time-resolved imaging-based crispri screening. *Nature Methods*, 17(1):86–92, 2020.

[25] C. Capdevila, M. Trifas, J. Miller, T. Anderson, P. A. Sims, and K. S. Yan. Cellular origins and lineage relationships of the intestinal epithelium. *American Journal of Physiology-Gastrointestinal and Liver Physiology*, 321(4):G413–G425, Aug. 2021.

[26] C. W. M. Chan, N. A. Wong, Y. Liu, D. Bicknell, H. Turley, L. Hollins, C. J. Miller, J. L. Wilding, and W. F. Bodmer. Gastrointestinal differentiation marker cytokeratin 20 is regulated by homeobox gene cdx1. *Proceedings of the National Academy of Sciences*, 106(6):1936–1941, Feb. 2009.

[27] K. H. Chen, A. N. Boettiger, J. R. Moffitt, S. Wang, and X. Zhuang. Spatially resolved, highly multiplexed rna profiling in single cells. *Science*, 348(6233):aaa6090, Apr. 2015.

[28] H. Cheng and C. P. Leblond. Origin, differentiation and renewal of the four main epithelial cell types in the mouse small intestine. v. unitarian theory of the origin of the four epithelial cell types. *The American journal of anatomy*, 141:537–61, Dec 1974.

[29] E. Clayton, D. P. Doupé, A. M. Klein, D. J. Winton, B. D. Simons, and P. H. Jones. A single type of progenitor cell maintains normal epidermis. *Nature*, 446:185–9, Mar 2007.

[30] H. Clevers. The intestinal crypt, a prototype stem cell compartment. *Cell*, 154:274–84, Jul 2013.

[31] H. Clevers. Modeling development and disease with organoids. *Cell*, 165(7):1586–1597, June 2016.

[32] R. Cooney, J. Baker, O. Brain, B. Danis, T. Pichulik, P. Allan, D. J. P. Ferguson, B. J. Campbell, D. Jewell, and A. Simmons. Nod2 stimulation induces autophagy in dendritic cells influencing bacterial handling and antigen presentation. *Nature Medicine*, 16(1):90–97, 2010.

[33] B. Corominas-Murtra, C. L. G. J. Scheele, K. Kishi, S. I. J. Ellenbroek, B. D. Simons, J. van Rheenen, and E. Hannezo. Stem cell lineage survival as a noisy competition for niche access. *Proceedings of the National Academy of Sciences*, 117(29):16969–16975, July 2020.

[34] E. Czech, B. A. Aksoy, P. Aksoy, and J. Hammerbacher. Cytokit: a single-cell analysis toolkit for high dimensional fluorescent microscopy imaging. *BMC Bioinformatics*, 20(1):448, 2019.

[35] J. F. Dekkers, M. Alieva, A. Cleven, F. Keramati, A. K. L. Wezenaar, E. J. van Vliet, J. Puschhof, P. Brazda, I. Johanna, A. D. Meringa, H. G. Rebel, M.-B. Buchholz, M. Barrera Román, A. L. Zeeman, S. de Blank, D. Fasci, M. H. Geurts, A. M. Cornel, E. Driehuis, R. Millen, T. Straetemans, M. J. T. Nicolasen, T. Aarts-Riemens, H. C. R. Ariese, H. R. Johnson, R. L. van Ineveld, F. Karaiskaki, O. Kopper, Y. E. Bar-Ephraim, K. Kretzschmar, A. M. M. Eggermont, S. Nierkens, E. J. Wehrens, H. G. Stunnenberg, H. Clevers, J. Kuball, Z. Sebestyen, and A. C. Rios. Uncovering the mode of action of engineered t cells in patient cancer organoids. *Nature biotechnology*, Jul 2022.

[36] E. Delaune, P. Francois, N. Shih, and S. Amacher. Single-cell-resolution imaging of the impact of notch signaling and mitosis on segmentation clock dynamics. *Developmental Cell*, 23(5):995–1005, Nov. 2012.

[37] D. P. Doupé, M. P. Alcolea, A. Roshan, G. Zhang, A. M. Klein, B. D. Simons, and P. H. Jones. A single progenitor population switches behavior to maintain and repair esophageal epithelium. *Science (New York, N.Y.)*, 337:1091–3, Aug 2012.

[38] D. P. Doupé and N. Perrimon. Visualizing and manipulating temporal signaling dynamics with fluorescence-based tools. *Science Signaling*, 7(319):re1–re1, Apr. 2014.

[39] J. Drost, R. H. van Jaarsveld, B. Ponsioen, C. Zimberlin, R. van Boxtel, A. Buijs, N. Sachs, R. M. Overmeer, G. J. Offerhaus, H. Begthel, J. Korving, M. van de Wetering, G. Schwank, M. Logtenberg, E. Cuppen, H. J. Snippert, J. P. Medema, G. J. P. L. Kops, and H. Clevers. Sequential cancer mutations in cultured human intestinal stem cells. *Nature*, 521:43–7, May 2015.

[40] A. Durand, B. Donahue, G. Peignon, F. Letourneur, N. Cagnard, C. Slomianny, C. Perret, N. F. Shroyer, and B. Romagnolo. Functional intestinal stem cells after paneth cell ablation induced by the loss of transcription factor math1 (atoh1). *Proceedings of the National Academy of Sciences of the United States of America*, 109:8965–70, Jun 2012.

[41] R. Edgar, M. Domrachev, and A. E. Lash. Gene expression omnibus: Ncbi gene expression and hybridization array data repository. *Nucleic acids research*, 30:207–10, Jan 2002.

[42] G. T. Eisenhoffer and J. Rosenblatt. Bringing balance by force: live cell extrusion controls epithelial cell numbers. *Trends in cell biology*, 23:185–92, Apr 2013.

[43] Y. Fan and O. Pedersen. Gut microbiota in human metabolic health and disease. *Nature Reviews Microbiology*, 19(1):55–71, 2021.

[44] O. M. Fannon, A. Bithell, B. J. Whalley, and E. Delivopoulos. A fiber alginate co-culture platform for the differentiation of mesc and modeling of the neural tube. *Frontiers in neuroscience*, 14:524346, 2020.

[45] H. F. Farin, I. Jordens, M. H. Mosa, O. Basak, J. Korving, D. V. F. Tauriello, K. de Punder, S. Angers, P. J. Peters, M. M. Maurice, and H. Clevers. Visualization of a short-range wnt gradient in the intestinal stem-cell niche. *Nature*, 530(7590):340–343, 2016.

[46] H. F. Farin, J. H. Van Es, and H. Clevers. Redundant sources of wnt regulate intestinal stem cells and promote formation of paneth cells. *Gastroenterology*, 143:1518–1529.e7, Dec 2012.

[47] J. Feigelman, S. Ganscha, S. Hastreiter, M. Schwarzfischer, A. Filipczyk, T. Schroeder, F. J. Theis, C. Marr, and M. Claassen. Analysis of cell lineage trees by exact bayesian inference identifies negative autoregulation of nanog in mouse embryonic stem cells. *Cell Systems*, 3(5):480–490.e13, Nov. 2016.

[48] W. Feller. Die grundlagen der volterraschen theorie des kampfes ums dasein in wahrscheinlichkeitstheoretischer behandlung. *Acta Biotheoretica*, 5:11–40, 1939.

[49] T. Fevr, S. Robine, D. Louvard, and J. Huelsken. Wnt/β-catenin is essential for intestinal homeostasis and maintenance of intestinal stem cells. *Molecular and cellular biology*, 27:7551–9, Nov 2007.

[50] S. Fre, M. Huyghe, P. Mourikis, S. Robine, D. Louvard, and S. Artavanis-Tsakonas. Notch signals control the fate of immature progenitor cells in the intestine. *Nature*, 435(7044):964–968, 2005.

[51] M. Fujii, M. Matano, K. Toshimitsu, A. Takano, Y. Mikami, S. Nishikori, S. Sugimoto, and T. Sato. Human intestinal organoids maintain self-renewal capacity and cellular diversity in niche-inspired culture condition. *Cell stem cell*, 23:787–793.e6, Dec 2018.

[52] H. Gehart and H. Clevers. Tales from the crypt: new insights into intestinal stem cells. *Nature reviews. Gastroenterology & hepatology*, 16:19–34, Jan 2019.

[53] C. Giesen, H. A. O. Wang, D. Schapiro, N. Zivanovic, A. Jacobs, B. Hattendorf, P. J. Schüffler, D. Grolimund, J. M. Buhmann, S. Brandt, Z. Varga, P. J. Wild, D. Günther, and B. Bodenmiller. Highly multiplexed imaging of tumor tissues with subcellular resolution by mass cytometry. *Nature Methods*, 11(4):417–422, 2014.

[54] A. Giladi, M. Cohen, C. Medaglia, Y. Baran, B. Li, M. Zada, P. Bost, R. Blecher-Gonen, T.-M. Salame, J. U. Mayer, E. David, F. Ronchese, A. Tanay, and I. Amit. Dissecting cellular crosstalk by sequencing physically interacting cells. *Nature Biotechnology*, 38(5):629–637, 2020.

[55] H. F. Gómez, M. S. Dumond, L. Hodel, R. Vetter, and D. Iber. 3d cell neighbour dynamics in growing pseudostratified epithelia. *eLife*, 10:e68135, oct 2021.

[56] A. Gregorieff, D. Pinto, H. Begthel, O. Destré, M. Kielman, and H. Clevers. Expression pattern of wnt signaling components in the adult intestine. *Gastroenterology*, 129:626–38, Aug 2005.

[57] D. Grün, A. Lyubimova, L. Kester, K. Wiebrands, O. Basak, N. Sasaki, H. Clevers, and A. van Oudenaarden. Single-cell messenger rna sequencing reveals rare intestinal cell types. *Nature*, 525(7568):251–255, 2015.

[58] A. L. Haber, M. Biton, N. Rogel, R. H. Herbst, K. Shekhar, C. Smillie, G. Burgin, T. M. Delorey, M. R. Howitt, Y. Katz, I. Tirosh, S. Beyaz, D. Dionne, M. Zhang, R. Raychowdhury, W. S. Garrett, O. Rozenblatt-Rosen, H. N. Shi, O. Yilmaz, R. J. Xavier, and A. Regev. A single-cell survey of the small intestinal epithelium. *Nature*, 551(7680):333–339, 2017.

[59] Y. Hao, S. Hao, E. Andersen-Nissen, W. M. Mauck, S. Zheng, A. Butler, M. J. Lee, A. J. Wilk, C. Darby, M. Zager, P. Hoffman, M. Stoeckius, E. Papalexi, E. P. Mimitou, J. Jain, A. Srivastava, T. Stuart, L. M. Fleming, B. Yeung, A. J. Rogers, J. M. McElrath, C. A. Blish, R. Gottardo, P. Smibert, and R. Satija. Integrated analysis of multimodal single-cell data. *Cell*, 184(13):3573–3587.e29, 2021.

[60] J. Hartmann, D. Krueger, and S. De Renzis. Using optogenetics to tackle systems-level questions of multicellular morphogenesis. *Current Opinion in Cell Biology*, 66:19–27, 2020.

[61] C. Haubold, J. Aleš, S. Wolf, and F. A. Hamprecht. A generalized successive shortest paths solver for tracking dividing targets. In B. Leibe, J. Matas, N. Sebe, and M. Welling, editors, *Computer Vision - ECCV 2016*, pages 566–582, Cham, 2016. Springer International Publishing.

[62] G.-W. He, L. Lin, J. DeMartino, X. Zheng, N. Staliarova, T. Dayton, H. Begthel, W. J. van de Wetering, E. Bodewes, J. van Zon, S. Tans, C. Lopez-Iglesias, P. J. Peters, W. Wu, D. Kotlarz, C. Klein, T. Margaritis, F. Holstege, and H. Clevers. Optimized human intestinal organoid model reveals interleukin-22-dependency of paneth cell formation. *Cell stem cell*, 29:1333–1345.e6, Sep 2022.

[63] Z. He, A. Maynard, A. Jain, T. Gerber, R. Petri, H.-C. Lin, M. Santel, K. Ly, J.-S. Dupré, L. Sidow, F. Sanchis Calleja, S. M. J. Jansen, S. Riesenberg, J. G. Camp, and B. Treutlein. Lineage recording in human cerebral organoids. *Nature Methods*, 19(1):90–99, 2022.

[64] M. Held, I. Santeramo, B. Wilm, P. Murray, and R. Lévy. Ex vivo live cell tracking in kidney organoids using light sheet fluorescence microscopy. *PLOS ONE*, 13(7):e0199918, July 2018.

[65] J. Heuberger, F. Kosel, J. Qi, K. S. Grossmann, K. Rajewsky, and W. Birchmeier. Shp2/mapk signaling controls goblet/paneth cell fate decisions in the intestine. *Proceedings of the National Academy of Sciences*, 111(9):3472–3477, Mar. 2014.

[66] D. G. Hicks, T. P. Speed, M. Yassin, and S. M. Russell. Maps of variability in cell lineage trees. *PLOS Computational Biology*, 15(2):e1006745, Feb. 2019.

[67] S. Hormoz, Z. S. Singer, J. M. Linton, Y. E. Antebi, B. I. Shraiman, and M. B. Elowitz. Inferring cell-state transition dynamics from lineage trees and endpoint single-cell measurements. *Cell Systems*, 3(5):419–433.e8, Nov. 2016.

[68] H. Hu, H. Gehart, B. Artegiani, C. Löpez-Iglesias, F. Dekkers, O. Basak, J. van Es, S. M. Chuva de Sousa Lopes, H. Begthel, J. Korving, M. van den Born, C. Zou, C. Quirk, L. Chiriboga, C. M. Rice, S. Ma, A. Rios, P. J. Peters, Y. P. de Jong, and H. Clevers. Long-term expansion of functional mouse and human hepatocytes as 3d organoids. *Cell*, 175:1591–1606.e19, Nov 2018.

[69] J. P. Hugot, M. Chamaillard, H. Zouali, S. Lesage, J. P. Cézard, J. Belaiche, S. Almer, C. Tysk, C. A. O'Morain, M. Gassull, V. Binder, Y. Finkel, A. Cortot, R. Modigliani, P. Laurent-Puig, C. Gower-Rousseau, J. Macry, J. F. Colombel, M. Sahbatou, and G. Thomas. Association of nod2 leucine-rich repeat variants with susceptibility to crohn's disease. *Nature*, 411:599–603, May 2001.

[70] S. Itzkovitz, I. Blat, T. Jacks, H. Clevers, and A. van Oudenaarden. Optimality in the development of intestinal crypts. *Cell*, 148(3):608–619, Feb. 2012.

[71] T. Jardé, W. H. Chan, F. J. Rossello, T. Kaur Kahlon, M. Theocharous, T. Kurian Arackal, T. Flores, M. Giraud, E. Richards, E. Chan, G. Kerr, R. M. Engel, M. Prasko, J. F. Donoghue, S.-I. Abe, T. J. Phesse, C. M. Nefzger, P. J. McMurrick, D. R. Powell, R. J. Daly, J. M. Polo, and H. E. Abud. Mesenchymal niche-derived neuregulin-1 drives intestinal stem cell proliferation and regeneration of damaged epithelium. *Cell stem cell*, 27:646–662.e7, Oct 2020.

[72] E.-h. Jho, T. Zhang, C. Domon, C.-K. Joo, J.-N. Freund, and F. Costantini. Wnt/beta-catenin/tcf signaling induces the transcription of axin2, a negative regulator of the signaling pathway. *Molecular and cellular biology*, 22:1172–83, Feb 2002.

[73] M. Kim, C. Fevre, M. Lavina, O. Disson, and M. Lecuit. Live imaging reveals listeria hijacking of e-cadherin recycling as it crosses the intestinal barrier. *Current biology : CB*, 31:1037–1047.e4, Mar 2021.

[74] T.-H. Kim, S. Escudero, and R. A. Shivdasani. Intact function of lgr5 receptor-expressing intestinal stem cells in the absence of paneth cells. *Proceedings of the National Academy of Sciences of the United States of America*, 109:3932–7, Mar 2012.

[75] D. J. Kiviet, P. Nghe, N. Walker, S. Boulineau, V. Sunderlikova, and S. J. Tans. Stochasticity of metabolism and growth at the single-cell level. *Nature*, 514(7522):376–379, 2014.

[76] A. M. Klein, D. P. Doupé, P. H. Jones, and B. D. Simons. Kinetics of cell division in epidermal maintenance. *Physical review. E, Statistical, nonlinear, and soft matter physics*, 76:021910, Aug 2007.

[77] A. M. Klein, T. Nakagawa, R. Ichikawa, S. Yoshida, and B. D. Simons. Mouse germ line stem cells undergo rapid and stochastic turnover. *Cell stem cell*, 7:214–24, Aug 2010.

[78] A. M. Klein and B. D. Simons. Universal patterns of stem cell fate in cycling adult tissues. *Development (Cambridge, England)*, 138:3103–11, Aug 2011.

[79] R. N. U. Kok, L. Hebert, G. Huelsz-Prince, Y. J. Goos, X. Zheng, K. Bozek, G. J. Stephens, S. J. Tans, and J. S. van Zon. Organoidtracker: Efficient cell tracking using machine learning and manual error correction. *PLOS ONE*, 15(10):e0240802, Oct. 2020.

[80] R. N. U. Kok, S. J. Tans, and J. S. van Zon. Minimizing cell number fluctuations in self-renewing tissues with a stem cell niche. *bioRxiv*, page 2022.03.10.483777, Jan. 2022.

[81] K. Kretzschmar and F. Watt. Lineage tracing. *Cell*, 148(1):33–45, Jan. 2012.

[82] M. A. Lancaster, M. Renner, C.-A. Martin, D. Wenzel, L. S. Bicknell, M. E. Hurles, T. Homfray, J. M. Penninger, A. P. Jackson, and J. A. Knoblich. Cerebral organoids model human brain development and microcephaly. *Nature*, 501(7467):373–379, 2013.

[83] A. D. Lander, K. K. Gokoffski, F. Y. M. Wan, Q. Nie, and A. L. Calof. Cell lineages and the logic of proliferative control. *PLOS Biology*, 7(1):e1000015, Jan. 2009.

[84] A. J. Langlands, A. A. Almet, P. L. Appleton, I. P. Newton, J. M. Osborne, and I. S. Näthke. Paneth cell-rich regions separated by a cluster of lgr5+ cells initiate crypt fission in the intestinal stem cell niche. *PLOS Biology*, 14(6):e1002491, June 2016.

[85] E. Lein, L. E. Borm, and S. Linnarsson. The promise of spatial transcriptomics for neuroscience in the era of molecular cell typing. *Science*, 358(6359):64–69, Oct. 2017.

[86] B. L. LeSavage, R. A. Suhar, N. Broguiere, M. P. Lutolf, and S. C. Heilshorn. Next-generation cancer organoids. *Nature Materials*, 21(2):143–159, 2022.

[87] L. Li and T. Xie. Stem cell niche: structure and function. *Annual review of cell and developmental biology*, 21:605–31, 2005.

[88] J.-R. Lin, B. Izar, S. Wang, C. Yapp, S. Mei, P. M. Shah, S. Santagata, P. K. Sorger, A. K. Chakraborty, A. Raj, C. Marr, and P. Horváth. Highly multiplexed immunofluorescence imaging of human tissues and tumors using t-cycif and conventional optical microscopes. *eLife*, 7:e31657, 2018.

[89] L. Lindenburg and M. Merkx. Engineering genetically encoded fret sensors, 2014.

[90] C. Lopez-Garcia, A. M. Klein, B. D. Simons, and D. J. Winton. Intestinal stem cell replacement follows a pattern of neutral drift. *Science (New York, N.Y.)*, 330:822–5, Nov 2010.

[91] O. Louthan. Chromogranin a in physiology and oncology. *Folia biologica*, 57:173–81, 2011.

[92] I. Lukonin, D. Serra, L. Challet Meylan, K. Volkmann, J. Baaten, R. Zhao, S. Meeusen, K. Colman, F. Maurer, M. B. Stadler, J. Jenkins, and P. Liberali. Phenotypic landscape of intestinal organoid regeneration. *Nature*, 586(7828):275–280, 2020.

[93] B. Lustig, B. Jerchow, M. Sachs, S. Weiler, T. Pietsch, U. Karsten, M. van de Wetering, H. Clevers, P. M. Schlag, W. Birchmeier, and J. Behrens. Negative feedback loop of wnt signaling through upregulation of conductin/axin2 in colorectal and liver tumors. *Molecular and cellular biology*, 22:1184–93, Feb 2002.

[94] J. Massey, Y. Liu, O. Alvarenga, T. Saez, M. Schmerer, and A. Warmflash. Synergy with tgfβ ligands switches wnt pathway dynamics from transient to sustained during human pluripotent cell differentiation. *Proceedings of the National Academy of Sciences*, 116(11):4989–4998, Mar. 2019.

[95] U. Mayr, D. Serra, and P. Liberali. Exploring single cells in space and time during tissue development, homeostasis and regeneration. *Development (Cambridge, England)*, 146, Jun 2019.

[96] K. McDole, L. Guignard, F. Amat, A. Berger, G. Malandain, L. A. Royer, S. C. Turaga, K. Branson, and P. J. Keller. in toto imaging and reconstruction of post-implantation mouse development at the single-cell level. *Cell*, 175(3):859–876.e33, Oct. 2018.

[97] A. McKenna and J. A. Gagnon. Recording development with single cell dynamic lineage tracing. *Development*, 146(12):dev169730, June 2019.

[98] K. L. McKinley, N. Stuurman, L. A. Royer, C. Schartner, D. Castillo-Azofeifa, M. Delling, O. D. Klein, R. D. Vale, and J. Rosenblatt. Cellular aspect ratio and cell division mechanics underlie the patterning of cell progeny in diverse mammalian epithelia. *eLife*, 7:e36739, 2018.

[99] E. Meijering, A. E. Carpenter, H. Peng, F. A. Hamprecht, and J.-C. Olivo-Marin. Imagining the future of bioimage analysis. *Nature Biotechnology*, 34(12):1250–1255, 2016.

[100] H. A. Messal, J. Almagro, M. Zaw Thin, A. Tedeschi, A. Ciccarelli, L. Blackie, K. I. Anderson, I. Miguel-Aliaga, J. van Rheenen, and A. Behrens. Antigen retrieval and clearing for whole-organ immunofluorescence by flash. *Nature protocols*, 16:239–262, Jan 2021.

[101] A. J. Miller, B. R. Dye, D. Ferrer-Torres, D. R. Hill, A. W. Overeem, L. D. Shea, and J. R. Spence. Generation of lung organoids from human pluripotent stem cells in vitro. *Nature Protocols*, 14(2):518–540, 2019.

[102] J. R. Moffitt, J. Hao, D. Bambah-Mukku, T. Lu, C. Dulac, and X. Zhuang. High-performance multiplexed fluorescence in situ hybridization in culture and tissue

with matrix imprinting and clearing. *Proceedings of the National Academy of Sciences*, 113(50):14456–14461, Dec. 2016.

[103] M. Mohme, C. L. Maire, K. Riecken, S. Zapf, T. Aranyossy, M. Westphal, K. Lamszus, and B. Fehse. Optical barcoding for single-clone tracking to study tumor heterogeneity. *Molecular Therapy*, 25(3):621–633, Mar. 2017.

[104] T. L. A. Nguyen, S. Vieira-Silva, A. Liston, and J. Raes. How informative is the mouse for human gut microbiota research? *Disease Models & Mechanisms*, 8(1):1–16, 01 2015.

[105] G. Noel, N. W. Baetz, J. F. Staab, M. Donowitz, O. Kovbasnjuk, M. F. Pasetti, and N. C. Zachos. A primary human macrophage-enteroid co-culture model to investigate mucosal gut physiology and host-pathogen interactions. *Scientific Reports*, 7(1):45270, 2017.

[106] R. Nusse and H. Clevers. Wnt/beta-catenin signaling, disease, and emerging therapeutic modalities. *Cell*, 169:985–999, Jun 2017.

[107] Y. Ogura, D. K. Bonen, N. Inohara, D. L. Nicolae, F. F. Chen, R. Ramos, H. Britton, T. Moran, R. Karaliuskas, R. H. Duerr, J. P. Achkar, S. R. Brant, T. M. Bayless, B. S. Kirschner, S. B. Hanauer, G. Nunez, and J. H. Cho. A frameshift mutation in nod2 associated with susceptibility to crohn's disease. *Nature*, 411:603–6, May 2001.

[108] I. A. Okkelman, T. Foley, D. B. Papkovsky, and R. I. Dmitriev. Live cell imaging of mouse intestinal organoids reveals heterogeneity in their oxygenation. *Biomaterials*, 146:86–96, 2017.

[109] M. Omerzu, N. Fenderico, B. de Barbanson, J. Sprangers, J. de Ridder, and M. M. Maurice. Three-dimensional analysis of single molecule fish in human colon organoids. *Biology open*, 8, Aug 2019.

[110] W. Pei, T. B. Feyerabend, J. Rössler, X. Wang, D. Postrach, K. Busch, I. Rode, K. Klapproth, N. Dietlein, C. Quedenau, W. Chen, S. Sauer, S. Wolf, T. Höfer, and H.-R. Rodewald. Polylox barcoding reveals haematopoietic stem cell fates realized in vivo. *Nature*, 548(7668):456–460, 2017.

[111] E. Pennisi. Development cell by cell. *Science*, 362(6421):1344–1345, Dec. 2018.

[112] C. Pleguezuelos-Manzano, J. Puschhof, A. Rosendahl Huber, A. van Hoeck, H. M. Wood, J. Nomburg, C. Gurjao, F. Manders, G. Dalmasso, P. B. Stege, F. L. Paganelli, M. H. Geurts, J. Beumer, T. Mizutani, Y. Miao, R. van der Linden, S. van der Elst, J. C. Ambrose, P. Arumugam, E. L. Baple, M. Bleda, F. Boardman-Pretty, J. M. Boissiere, C. R. Boustred, H. Brittain, M. J. Caulfield, G. C. Chan, C. E. H. Craig, L. C. Daugherty, A. de Burca, A. Devereau, G. Elgar, R. E. Foulger, T. Fowler, P. Furió-Tarí, J. M. Hackett, D. Halai, A. Hamblin, S. Henderson, J. E. Holman, T. J. P. Hubbard, K. Ibáñez, R. Jackson, L. J. Jones, D. Kasperaviciute, M. Kayikci, L. Lahnstein, L. Lawson, S. E. A. Leigh, I. U. S. Leong, F. J. Lopez, F. Maleady-Crowe, J. Mason, E. M. McDonagh, L. Moutsianas, M. Mueller, N. Murugaesu, A. C. Need, C. A. Odhams, C. Patch,

D. Perez-Gil, D. Polychronopoulos, J. Pullinger, T. Rahim, A. Rendon, P. Riesgo-Ferreiro, T. Rogers, M. Ryten, K. Savage, K. Sawant, R. H. Scott, A. Siddiq, A. Sieghart, D. Smedley, K. R. Smith, A. Sosinsky, W. Spooner, H. E. Stevens, A. Stuckey, R. Sultana, E. R. A. Thomas, S. R. Thompson, C. Tregidgo, A. Tucci, E. Walsh, S. A. Watters, M. J. Welland, E. Williams, K. Witkowska, S. M. Wood, M. Zarowiecki, K. C. Garcia, J. Top, R. J. L. Willems, M. Giannakis, R. Bonnet, P. Quirke, M. Meyerson, E. Cuppen, R. van Boxtel, H. Clevers, and G. E. R. Consortium. Mutational signature in colorectal cancer caused by genotoxic pks+ e. coli. *Nature*, 580(7802):269–273, 2020.

[113] C. Pleguezuelos-Manzano, J. Puschhof, S. van den Brink, V. Geurts, J. Beumer, and H. Clevers. Establishment and culture of human intestinal organoids derived from adult stem cells. *Current Protocols in Immunology*, 130(1):e106, Sept. 2020.

[114] J. Puschhof, C. Pleguezuelos-Manzano, A. Martinez-Silgado, N. Akkerman, A. Saftien, C. Boot, A. de Waal, J. Beumer, D. Dutta, I. Heo, and H. Clevers. Intestinal organoid cocultures with microbes. *Nature Protocols*, 16(10):4633–4649, 2021.

[115] K. Ragkousi and M. C. Gibson. Cell division and the maintenance of epithelial order. *Journal of Cell Biology*, 207(2):181–188, 10 2014.

[116] D. Ramanan, M. S. Tang, R. Bowcutt, P. Loke, and K. Cadwell. Bacterial sensor nod2 prevents inflammation of the small intestine by restricting the expansion of the commensal bacteroides vulgatus. *Immunity*, 41:311–24, Aug 2014.

[117] D. A. Rennerfeldt, J. S. Raminhos, S. M. Leff, P. Manning, and K. J. Van Vliet. Emergent heterogeneity in putative mesenchymal stem cell colonies: Single-cell time lapsed analysis. *PLOS ONE*, 14(4):e0213452, Apr. 2019.

[118] E. Y. Rim, H. Clevers, and R. Nusse. The wnt pathway: From signaling mechanisms to synthetic modulators. *Annual review of biochemistry*, 91:571–598, Jun 2022.

[119] A. C. Rios and H. Clevers. Imaging organoids: a bright future ahead. *Nature Methods*, 15(1):24–26, 2018.

[120] L. Ritsma, S. I. J. Ellenbroek, A. Zomer, H. J. Snippert, F. J. de Sauvage, B. D. Simons, H. Clevers, and J. van Rheenen. Intestinal crypt homeostasis revealed at single-stem-cell level by in vivo live imaging. *Nature*, 507(7492):362–365, 2014.

[121] M. J. Rodríguez-Colman, M. Schewe, M. Meerlo, E. Stigter, J. Gerrits, M. Pras-Raves, A. Sacchetti, M. Hornsveld, K. C. Oost, H. J. Snippert, N. Verhoeven-Duif, R. Fodde, and B. M. T. Burgering. Interplay between metabolic identities in the intestinal crypt supports stem cell function. *Nature*, 543(7645):424–427, 2017.

[122] S. G. Rodriques, R. R. Stickels, A. Goeva, C. A. Martin, E. Murray, C. R. Vanderburg, J. Welch, L. M. Chen, F. Chen, and E. Z. Macosko. Slide-seq: A scalable technology for measuring genome-wide expression at high spatial resolution. *Science*, 363(6434):1463–1467, Mar. 2019.

[123] A. B. Rosenbloom, M. Tarczyński, N. Lam, R. S. Kane, L. J. Bugaj, and D. V. Schaffer. β-catenin signaling dynamics regulate cell fate in differentiating neural stem cells. *Proceedings of the National Academy of Sciences*, 117(46):28828–28837, Nov. 2020.

[124] J. Rubert, P. J. Schweiger, F. Mattivi, K. Tuohy, K. B. Jensen, and A. Lunardi. Intestinal organoids: A tool for modelling diet-microbiome-host interactions. *Trends in Endocrinology & Metabolism*, 31(11):848–858, Nov. 2020.

[125] P. Rué and A. Martinez Arias. Cell dynamics and gene expression control in tissue homeostasis and development. *Molecular systems biology*, 11:792, Feb 2015.

[126] C. T. Rueden, J. Schindelin, M. C. Hiner, B. E. DeZonia, A. E. Walter, E. T. Arena, and K. W. Eliceiri. Imagej2: Imagej for the next generation of scientific image data. *BMC Bioinformatics*, 18(1):529, 2017.

[127] L. E. Sanman, I. W. Chen, J. M. Bieber, V. Steri, C. Trentesaux, B. Hann, O. D. Klein, L. F. Wu, and S. J. Altschuler. Transit-amplifying cells coordinate changes in intestinal epithelial cell-type composition. *Developmental cell*, 56:356–365.e9, Feb 2021.

[128] R. B. Sartor. Mechanisms of disease: pathogenesis of crohn's disease and ulcerative colitis. *Nature clinical practice. Gastroenterology & hepatology*, 3:390–407, Jul 2006.

[129] T. Sato, J. H. van Es, H. J. Snippert, D. E. Stange, R. G. Vries, M. van den Born, N. Barker, N. F. Shroyer, M. van de Wetering, and H. Clevers. Paneth cells constitute the niche for lgr5 stem cells in intestinal crypts. *Nature*, 469:415–8, Jan 2011.

[130] T. Sato, R. G. Vries, H. J. Snippert, M. van de Wetering, N. Barker, D. E. Stange, J. H. van Es, A. Abo, P. Kujala, P. J. Peters, and H. Clevers. Single lgr5 stem cells build crypt-villus structures in vitro without a mesenchymal niche. *Nature*, 459:262–5, May 2009.

[131] D. Schapiro, H. W. Jackson, S. Raghuraman, J. R. Fischer, V. R. T. Zanotelli, D. Schulz, C. Giesen, R. Catena, Z. Varga, and B. Bodenmiller. histocat: analysis of cell phenotypes and interactions in multiplex image cytometry data. *Nature Methods*, 14(9):873–876, 2017.

[132] M. Schiegg, P. Hanslovsky, C. Haubold, U. Koethe, L. Hufnagel, and F. A. Hamprecht. Graphical model for joint segmentation and tracking of multiple dividing cells. *Bioinformatics*, 31(6):948–956, Mar. 2015.

[133] J. Schindelin, I. Arganda-Carreras, E. Frise, V. Kaynig, M. Longair, T. Pietzsch, S. Preibisch, C. Rueden, S. Saalfeld, B. Schmid, J.-Y. Tinevez, D. J. White, V. Hartenstein, K. Eliceiri, P. Tomancak, and A. Cardona. Fiji: an open-source platform for biological-image analysis. *Nature Methods*, 9(7):676–682, 2012.

[134] C. A. Schneider, W. S. Rasband, and K. W. Eliceiri. Nih image to imagej: 25 years of image analysis. *Nature Methods*, 9(7):671–675, 2012.

[135] S. E. Schonhoff, M. Giel-Moloney, and A. B. Leiter. Neurogenin 3-expressing progenitor cells in the gastrointestinal tract differentiate into both endocrine and non-endocrine cell types. *Developmental biology*, 270:443–54, Jun 2004.

[136] J. Schuijers, J. P. Junker, M. Mokry, P. Hatzis, B.-K. Koo, V. Sasselli, L. G. van der Flier, E. Cuppen, A. van Oudenaarden, and H. Clevers. Ascl2 acts as an r-spondin/wnt-responsive switch to control stemness in intestinal crypts. *Cell stem cell*, 16:158–70, Feb 2015.

[137] D. H. Scoville, T. Sato, X. C. He, and L. Li. Current view: intestinal stem cells and signaling. *Gastroenterology*, 134:849–64, Mar 2008.

[138] Y. Sei, J. Feng, C. C. Chow, and S. A. Wank. Asymmetric cell division-dominant neutral drift model for normal intestinal stem cell homeostasis. *American journal of physiology. Gastrointestinal and liver physiology*, 316:G64–G74, Jan 2019.

[139] D. Serra, U. Mayr, A. Boni, I. Lukonin, M. Rempfler, L. Challet Meylan, M. B. Stadler, P. Strnad, P. Papasaikas, D. Vischi, A. Waldt, G. Roma, and P. Liberali. Self-organization and symmetry breaking in intestinal organoid development. *Nature*, 569(7754):66–72, 2019.

[140] M. Shoshkes-Carmel, Y. J. Wang, K. J. Wangensteen, B. Tóth, A. Kondo, E. E. Massasa, S. Itzkovitz, and K. H. Kaestner. Subepithelial telocytes are an important source of wnts that supports intestinal crypts. *Nature*, 557(7704):242–246, 2018.

[141] N. Shroyer, D. Wallis, K. Venken, H. Bellen, and H. Zoghbi. Shroyer nf, wallis d, venken kj, bellen hj, zoghbi hy.. gfi1 functions downstream of math1 to control intestinal secretory cell subtype allocation and differentiation. gene dev 19: 2412-2417. *Genes & development*, 19:2412–7, Nov. 2005.

[142] J. Sidhaye and J. A. Knoblich. Brain organoids: an ensemble of bioassays to investigate human neurodevelopment and disease. *Cell Death & Differentiation*, 28(1):52–67, 2021.

[143] B. D. Simons and H. Clevers. Strategies for homeostatic stem cell self-renewal in adult tissues. *Cell*, 145:851–62, Jun 2011.

[144] S. Skylaki, O. Hilsenbeck, and T. Schroeder. Challenges in long-term imaging and quantification of single-cell dynamics. *Nature Biotechnology*, 34(11):1137–1144, 2016.

[145] H. J. Snippert, L. G. van der Flier, T. Sato, J. H. van Es, M. van den Born, C. Kroon-Veenboer, N. Barker, A. M. Klein, J. van Rheenen, B. D. Simons, and H. Clevers. Intestinal crypt homeostasis results from neutral competition between symmetrically dividing lgr5 stem cells. *Cell*, 143(1):134–144, Oct. 2010.

[146] M. Sobczak, A. Fabisiak, N. Murawska, E. Wesolowska, P. Wierzbicka, M. Wlazlowski, M. Wójcikowska, H. Zatorski, M. Zwolińska, and J. Fichna. Current overview of extrinsic and intrinsic factors in etiology and progression of inflammatory bowel diseases. *Pharmacological reports : PR*, 66:766–75, Oct 2014.

[147] K. F. Sonnen and C. Y. Janda. Signalling dynamics in embryonic development. *Biochem J*, 478(23):4045–4070, Dec. 2021.

[148] K. F. Sonnen, V. M. Lauschke, J. Uraji, H. J. Falk, Y. Petersen, M. C. Funk, M. Beaupeux, P. Francois, C. A. Merten, and A. Aulehla. Modulation of phase shift between wnt and notch signaling oscillations controls mesoderm segmentation. *Cell*, 172(5):1079–1090.e12, Feb. 2018.

[149] K. F. Sonnen and C. A. Merten. Microfluidics as an emerging precision tool in developmental biology. *Developmental Cell*, 48(3):293–311, 2019.

[150] M. Spit, B.-K. Koo, and M. M. Maurice. Tales from the crypt: intestinal niche signals in tissue renewal, plasticity and cancer. *Open Biology*, 8(9):180120, Sept. 2018.

[151] T. Stadler, S. Skylaki, K. D. Kokkaliaris, and T. Schroeder. On the statistical analysis of single cell lineage trees. *Journal of Theoretical Biology*, 439:160–165, 2018.

[152] P. L. Ståhl, F. Salmén, S. Vickovic, A. Lundmark, J. F. Navarro, J. Magnusson, S. Giacomello, M. Asp, J. O. Westholm, M. Huss, A. Mollbrink, S. Linnarsson, S. Codeluppi, A. Borg, F. Pontén, P. I. Costea, P. Sahlén, J. Mulder, O. Bergmann, J. Lundeberg, and J. Frisén. Visualization and analysis of gene expression in tissue sections by spatial transcriptomics. *Science*, 353(6294):78–82, July 2016.

[153] D. Stamataki, M. Holder, C. Hodgetts, R. Jeffery, E. Nye, B. Spencer-Dene, D. J. Winton, and J. Lewis. Delta1 expression, cell cycle exit, and commitment to a specific secretory fate coincide within a few hours in the mouse intestinal stem cell system. *PLOS ONE*, 6(9):e24484, Sept. 2011.

[154] C. Stringer, T. Wang, M. Michaelos, and M. Pachitariu. Cellpose: a generalist algorithm for cellular segmentation. *Nature Methods*, 18(1):100–106, 2021.

[155] K. Sugawara, c. Çevrim, M. Averof, M. W. Mathis, A. M. Walczak, A. Iqbal, and C. Tischer. Tracking cell lineages in 3d by incremental deep learning. *eLife*, 11:e69380, 2022.

[156] J. E. Sulston, E. Schierenberg, J. G. White, and J. N. Thomson. The embryonic cell lineage of the nematode caenorhabditis elegans. *Developmental Biology*, 100(1):64–119, 1983.

[157] Z. Sun and N. L. Komarova. Stochastic modeling of stem-cell dynamics with control. *Mathematical biosciences*, 240:231–40, Dec 2012.

[158] C.-M. Svensson, A. Medyukhina, I. Belyaev, N. Al-Zaben, and M. T. Figge. Untangling cell tracks: Quantifying cell migration by time lapse image data analysis. *Cytometry*, 93(3):357–370, Mar. 2018.

[159] P. S. Swain. Lecture notes on stochastic models in systems biology. *arXiv preprint arXiv:1607.07806*, 2016.

[160] N. P. Tallapragada, H. M. Cambra, T. Wald, S. Keough Jalbert, D. M. Abraham, O. D. Klein, and A. M. Klein. Inflation-collapse dynamics drive patterning and morphogenesis in intestinal organoids. *Cell stem cell*, 28:1516–1532.e14, Sep 2021.

[161] V. H. Teixeira, P. Nadarajan, T. A. Graham, C. P. Pipinikas, J. M. Brown, M. Falzon, E. Nye, R. Poulsom, D. Lawrence, N. A. Wright, S. McDonald, A. Giangreco, B. D. Simons, S. M. Janes, and B. Hogan. Stochastic homeostasis in human airway epithelium is achieved by neutral competition of basal cell progenitors. *eLife*, 2:e00966, 2013.

[162] B. Tóth, S. Ben-Moshe, A. Gavish, N. Barkai, and S. Itzkovitz. Early commitment and robust differentiation in colonic crypts. *Mol Syst Biol*, 13(1):902, Jan. 2017.

[163] V. Ulman, M. Maška, K. E. G. Magnusson, O. Ronneberger, C. Haubold, N. Harder, P. Matula, P. Matula, D. Svoboda, M. Radojevic, I. Smal, K. Rohr, J. Jaldén, H. M. Blau, O. Dzyubachyk, B. Lelieveldt, P. Xiao, Y. Li, S.-Y. Cho, A. C. Dufour, J.-C. Olivo-Marin, C. C. Reyes-Aldasoro, J. A. Solis-Lemus, R. Bensch, T. Brox, J. Stegmaier, R. Mikut, S. Wolf, F. A. Hamprecht, T. Esteves, P. Quelhas, Ö. Demirel, L. Malmström, F. Jug, P. Tomancak, E. Meijering, A. Muñoz-Barrutia, M. Kozubek, and C. Ortiz-de Solorzano. An objective comparison of cell-tracking algorithms. *Nature Methods*, 14(12):1141–1152, 2017.

[164] A. A. A. van de Moosdijk, Y. B. C. van de Grift, S. M. A. de Man, A. L. Zeeman, and R. van Amerongen. A novel axin2 knock-in mouse model for visualization and lineage tracing of wnt/ctnnb1 responsive cells. *Genesis (New York, N.Y. : 2000)*, 58:e23387, Sep 2020.

[165] L. G. van der Flier and H. Clevers. Stem cells, self-renewal, and differentiation in the intestinal epithelium. *Annual review of physiology*, 71:241–60, 2009.

[166] J. H. van Es, T. Sato, M. van de Wetering, A. Lyubimova, A. N. Yee Nee, A. Gregorieff, N. Sasaki, L. Zeinstra, M. van den Born, J. Korving, A. C. M. Martens, N. Barker, A. van Oudenaarden, and H. Clevers. Dll1+ secretory progenitor cells revert to stem cells upon crypt damage. *Nature cell biology*, 14:1099–1104, Oct 2012.

[167] J. H. van Es, M. E. van Gijn, O. Riccio, M. van den Born, M. Vooijs, H. Begthel, M. Cozijnsen, S. Robine, D. J. Winton, F. Radtke, and H. Clevers. Notch/gamma-secretase inhibition turns proliferative cells in intestinal crypts and adenomas into goblet cells. *Nature*, 435:959–63, Jun 2005.

[168] J. H. van Es, K. Wiebrands, C. López-Iglesias, M. van de Wetering, L. Zeinstra, M. van den Born, J. Korving, N. Sasaki, P. J. Peters, A. van Oudenaarden, and H. Clevers. Enteroendocrine and tuft cells support lgr5 stem cells on paneth cell depletion. *Proceedings of the National Academy of Sciences of the United States of America*, 116:26599–605, Dec 2019.

[169] O. Viader-Llargués, V. Lupperger, L. Pola-Morell, C. Marr, H. López-Schier, and T. T. Whitfield. Live cell-lineage tracing and machine learning reveal patterns of organ regeneration. *eLife*, 7:e30823, 2018.

[170] G. Vlachogiannis, S. Hedayat, A. Vatsiou, Y. Jamin, J. Fernández-Mateos, K. Khan, A. Lampis, K. Eason, I. Huntingford, R. Burke, M. Rata, D.-M. Koh, N. Tunariu, D. Collins, S. Hulkki-Wilson, C. Ragulan, I. Spiteri, S. Y. Moorcraft, I. Chau, S. Rao, D. Watkins, N. Fotiadis, M. Bali, M. Darvish-Damavandi, H. Lote, Z. Eltahir, E. C. Smyth, R. Begum, P. A. Clarke, J. C. Hahne, M. Dowsett, J. de Bono, P. Workman, A. Sadanandam, M. Fassan, O. J. Sansom, S. Eccles, N. Starling, C. Braconi, A. Sottoriva, S. P. Robinson, D. Cunningham, and N. Valeri. Patient-derived organoids model treatment response of metastatic gastrointestinal cancers. *Science*, 359(6378):920–926, Feb. 2018.

[171] D. E. Wagner and A. M. Klein. Lineage tracing meets single-cell omics: opportunities and challenges. *Nature Reviews Genetics*, 21(7):410–427, 2020.

[172] B. Wang, M. Yao, L. Lv, Z. Ling, and L. Li. The human microbiota in health and disease. *Engineering*, 3(1):71–82, 2017.

[173] B.-G. Wang, I. Riemann, H. Schubert, K.-J. Halbhuber, and K. Koenig. In-vivo intratissue ablation by nanojoule near-infrared femtosecond laser pulses. *Cell and tissue research*, 328:515–20, Jun 2007.

[174] K. Weber, M. Thomaschewski, M. Warlich, T. Volz, K. Cornils, B. Niebuhr, M. Täger, M. Lügehetmann, J.-M. Pollok, C. Stocking, M. Dandri, D. Benten, and B. Fehse. Rgb marking facilitates multicolor clonal cell tracking. *Nature Medicine*, 17(4):504–509, 2011.

[175] C. Weinreb, A. Rodriguez-Fraticelli, F. D. Camargo, and A. M. Klein. Lineage tracing on transcriptional landscapes links state to fate during differentiation. *Science*, 367(6479):eaaw3381, Feb. 2020.

[176] K. E. Wiese, R. Nusse, and R. van Amerongen. Wnt signalling: conquering complexity. *Development (Cambridge, England)*, 145, Jun 2018.

[177] D. J. Winton and B. A. Ponder. Stem-cell organization in mouse small intestine. *Proceedings. Biological sciences*, 241:13–8, Jul 1990.

[178] C. Wolff, J.-Y. Tinevez, T. Pietzsch, E. Stamataki, B. Harich, L. Guignard, S. Preibisch, S. Shorte, P. J. Keller, P. Tomancak, A. Pavlopoulos, and A. Sánchez Alvarado. Multi-view light-sheet imaging and tracking with the mamut software reveals the cell lineage of a direct developing arthropod limb. *eLife*, 7:e34410, 2018.

[179] F. Xing, Y. Xie, H. Su, F. Liu, and L. Yang. Deep learning in microscopy image analysis: A survey. *IEEE Transactions on Neural Networks and Learning Systems*, 29(10):4550–4568, 2018.

[180] Q. Yang, N. A. Bermingham, M. J. Finegold, and H. Y. Zoghbi. Requirement of math1 for secretory cell lineage commitment in the mouse intestine. *Science (New York, N.Y.)*, 294:2155–8, Dec 2001.

[181] M. Yuan, X. Yang, J. Lin, X. Cao, F. Chen, X. Zhang, Z. Li, G. Zheng, X. Wang, X. Chen, and J.-R. Yang. Alignment of cell lineage trees elucidates genetic programs for the development and evolution of cell types. *iScience*, 23(7), July 2020.

[182] M. L. Zhao, A. Rabiee, K. M. Kovary, Z. Bahrami-Nejad, B. Taylor, and M. N. Teruel. Molecular competition in g1 controls when cells simultaneously commit to terminally differentiate and exit the cell cycle. *Cell Reports*, 31(11), June 2020.

[183] X. Zheng, M. A. Betjes, Y. J. Goos, G. Huelsz-Prince, H. Clevers, J. S. van Zon, and S. J. Tans. Following cell type transitions in space and time by combining live-cell tracking and endpoint cell identity in intestinal organoids. *bioRxiv*, page 2022.06.27.497728, Jan. 2022.

About the author

Xuan Zheng was born in November 1992 in Shanxi, a mountainous area in the north of China. In 2010, she moved to Hangzhou, a picturesque city in the south of China, to study Optics in Zhejiang University. There she started her passion towards imaging.

2014 was the year of adventure for Xuan. She received a TU Delft Excellence scholarship, moved to the Netherlands and joined the master program of Applied Physics in Delft. After a summer internship in *imec* (Leuven, Belgium) about lensfree imaging in 2015, she returned to Delft and wrote her master thesis regarding imaging bacterial chromosomes under the supervision of Dr. Fabai Wu and Prof. Cees Dekker. She obtained her Master degree of Applied Physics in the summer of 2016 and stayed in the lab as a research assistant to explore further the thesis project. In 2017, she moved to Sweden and conducted a research internship about protein DNA interactions in the group of Prof. Johan Elf in Uppsala University.

2018 was another year of milestone for her. In February that year, she started her PhD in the Biophysics group of Prof. Sander Tans and the Quantitative Developmental Biology group of Dr. Jeroen van Zon at AMOLF, Amsterdam, where she performed the research presented in this thesis.

At the beginning of 2023, Xuan joined the Organoid Group (previously the lab of Prof. Hans Clevers) at the Hubrecht Institute in Utrecht as a postdoc to pursue further in the field of organoids.

LIST OF PUBLICATIONS

RELATED TO THIS THESIS

B. Artegiani*, D. Hendriks*, J. Beumer, R. Kok, **X. Zheng**, I. Joore, S. Chuva de Sousa Lopes, J. van Zon, S.J. Tans and H. Clevers, ***Fast and efficient generation of knock-in human organoids using homology-independent CRISPR–Cas9 precision genome editing***, Nature Cell Biology 22, 321–331 (2020).

R.N.U. Kok, L. Hebert, G. Huelsz-Prince, Y.J. Goos, **X. Zheng**, K. Bozek, G.J. Stephens, S.J. Tans# and J. van Zon#. ***OrganoidTracker: Efficient cell tracking using machine learning and manual error correction***, PLOS ONE 15(10) (2020).

M.A. Betjes*, **X. Zheng***, R.N.U. Kok*, J.S. van Zon# and S.J. Tans#, ***Cell tracking for organoids: Lessons from developmental biology***, Frontiers in cell and developmental biology, 9:675013 (2021). **(Chapter 1)**

G.W. He*, L. Lin*, J. DeMartino, **X. Zheng**, N. Staliarova, T. Dayton, H. Begthel, W.J. van de Wetering, E. Bodewes, J. van Zon, S.J. Tans, C. Lopez-Iglesias, P.J. Peters, W. Wu, D. Kotlarz, C. Klein, T. Margaritis, F. Holstege and H. Clevers, ***Optimized human intestinal organoid model reveals interleukin-22-dependency of paneth cell formation***, Cell stem cell, 29(9) (2022).

G. Huelsz-Prince, R.N.U. Kok, Y.J. Goos, L. Bruens, **X. Zheng**, S.I. Ellenbroek, J. van Rheenen, S.J. Tans and J.S. van Zon, ***Mother cells control daughter cell proliferation in intestinal organoids to minimize proliferation fluctuations***, ELife 11: e80682 (2022). **(Chapter 2)**

X. Zheng, M.A. Betjes, Y.J. Goos, G. Huelsz-Prince, H. Clevers, J.S. van Zon# and S.J. Tans#, ***Organoid cell fate dynamics in space and time***, Science Advances, manuscript under review. **(Chapter 3)**

R.N.U. Kok*, **X. Zheng***, T. Clement, K. Spoelstra, J.S. van Zon#, S.J. Tans#, ***Loss of Paneth cell contact starts a differentiation timer in the intestinal crypt***, manuscript in preparation. **(Chapter 4)**

OTHER PUBLICATIONS

E. Marklund*, B. van Oosten*, G. Mao*, E. Amselem*, K. Kipper, A. Sabantsev, A. Emmerish, D. Globisch, **X. Zheng**, L.C. Lehmann, O.G. Berg, M. Johansson, J. Elf# and S.Deindl#, ***DNA***

surface exploration and operator bypassing during target search, Nature 583, 858–861 (2020).

F. Wu*, A. Japaridze*, **X. Zheng**, J. Wiktor, J.W.J. Kerssemakers and C. Dekker, ***Direct imaging of the circular chromosome in a live bacterium***, Nature Communications 10, 2194 (2019).

F. Wu, P. Swain, L. Kuijpers, **X. Zheng**, K. Felter, M. Guurink, J. Solari, S. Jun, T.S. Shimizu, D. Chaudhuri, B. Mulder and C. Dekker, ***Cell Boundary Confinement Sets the Size and Position of the E. coli Chromosome***, Current Biology, Volume 29, Issue 13 (2019).

T. Pauwelyn, R. Stahl, L. Mayo, **X. Zheng**, A. Lambrechts, S. Janssens, L. Lagae, V. Reumers and D. Braeken, ***Reflective lens-free imaging on high-density silicon microelectrode arrays for monitoring and evaluation of in vitro cardiac contractility***, Biomed. Opt. Express 9, 1827-1841 (2018).

* co-first authors
\# co-last authors

Acknowledgments

There is a poem, written by a Chinese poet *Lu You* from the Song Dynasty, that reads: "After endless mountains and rivers that leave doubt whether there is a path out, suddenly one encounters the shade of a willow, bright flowers and a lovely village." This poem describing his trip gives a good summary of my PhD journey, which is much more than what a thesis book and several journal articles can convey. It is a journey containing not only joy and satisfaction, but also confusion, frustration, loneliness, and doubts. It takes grittiness and great support to find the path out. I feel privileged to have so many great people to share this journey with.

First, I would like to thank my supervisors. **Sander** and **Jeroen**, I am grateful for everything that I have learned from you. I admire your courage in taking on new fields and your ability to navigate important research issues.

I also would like to thank the wonderful helps from our collaborators! **Hans**, **Benedetta**, **Delilah**, **Lin**, **Gui-wei**, **Daniel**, **Jacco**, **Lotte**, **Saskia**, **Maria** and **Nguyen**, it was a great pleasure to bring together our toolbox and march further in science as teams.

Our organoid team deserves my gratitude. **Guizela**, thanks for your great initial help, which has been a cornerstone for this thesis. **Yvonne**, thanks for introducing me to organoid culture, and your helps on both lab work and tracking have been instrumental in my PhD journey. **Rutger**, thanks for bringing the expertise in machine learning and software development. **Max**, thanks for the great contributions to the TypeTracker projects, the improvised brainstorming discussions, and our occasional reflections on the academic career paths. This thesis got a Dutch summary thanks to you. **Pascal**, thanks for your great helps during the revision and the sharing of graduation experiences. **Kasper**, thanks for your very useful discussions both on the projects and on career planning. **Tinka**, I am proud to have you as a student, and thanks for your great work on the Axin2 project. **Pieter Rein** and **Michael**, thanks for your feedback and discussions during our Organoid meeting.

The office! 1.37 feels like another home to me during these years. **Martijn**, thanks for bringing the plants to the office. **Anne-Bart**, thanks for your patience when I kept bothering you with my junior PhD worries, your unique poilitically incorrect humor, and the funny mandarin. **Florian**, we shared the office for almost my whole PhD. Thanks for being my daily coffee buddy, always offering great advice and keeping our office fun even during Covid. **Mark**, I appreciate our sharing of the pressure to finish up and look ahead. **Amber**, our lunch breaks together and discussion about Sweden were very joyful. **Mees**, it was a lot of fun to chat with you and witness your transition from a master student to a PhD student, both in Amolf!

Being in two different groups has been an interesting experience, with 2x team building events and unique knowledge of organoids, pulling proteins, and getting worms stressed. **Mario**, **Eline**, **Mohsin**, **Jason**, **Olga**, **Joleen**, and **Ercag**, thanks for introducing